Multi-dimensional disaggregation of land surface temperature using high-resolution red, near-infrared, shortwave-infrared and microwave-L bands

Olivier Merlin, Frédéric Jacob, Jean Pierre Wigneron, Jeffrey P. Walker, Ghani Chehbouni

Multidimensional Disaggregation of Land Surface Temperature Using High-Resolution Red, Near-Infrared, Shortwave-Infrared, and Microwave-L Bands

Olivier Merlin, Frédéric Jacob, Jean-Pierre Wigneron, Jeffrey Walker, and Ghani Chehbouni

***Abstract*—Land surface temperature data are rarely available at high temporal and spatial resolutions at the same locations. To fill this gap, the low spatial resolution data can be disaggregated at high temporal frequency using empirical relationships between remotely sensed temperature and fractional green (photosynthetically active) and senescent vegetation covers. In this paper, a new disaggregation methodology is developed by physically linking remotely sensed surface temperature to fractional green and senescent vegetation covers using a radiative transfer equation. Moreover, the methodology is implemented with two additional factors related to the energy budget of irrigated areas, being the fraction of open water and soil evaporative efficiency (ratio of actual to potential soil evaporation). The approach is tested over a 5 km by 32 km irrigated agricultural area in Australia using airborne Polarimetric L-band Multibeam Radiometer brightness temperature and spaceborne Advanced Scanning Thermal Emission and Reflection radiometer (ASTER) multispectral data. Fractional green vegetation cover, fractional senescent vegetation cover, fractional open water, and soil evaporative efficiency are derived from red, near-infrared, shortwave-infrared, and microwave-L band data. Low-resolution land surface temperature is simulated by aggregating ASTER land surface temperature to 1-km resolution, and the disaggregated temperature is verified against the high-resolution ASTER temperature data initially used in the aggregation process. The error in disaggregated temperature is successively reduced from 1.65 °C to 1.16 °C by including each of the four parameters. The correlation coefficient and slope between the disaggregated and ASTER temperatures are improved from 0.79 to 0.89 and from 0.63 to 0.88, respectively. Moreover, the radiative transfer equation allows quantification of the impact on disaggregation of the temperature at high resolution for each parameter: fractional green vegetation cover is responsible for 42% of the variability in disaggregated temperature, fractional senescent vegetation cover for 11%, fractional open water for 20%, and soil evaporative efficiency for 27%.**

***Index Terms*—Advanced Scanning Thermal Emission and Reflection radiometer (ASTER), brightness temperature, disaggregation, evaporative efficiency, land surface temperature, Moderate Resolution Imaging Spectroradiometer (MODIS), multispectral, open water, soil moisture, vegetation fraction.**

I. Introduction

REMOTELY sensed land surface temperature is a signature of the thermodynamic equilibrium state of the surface skin. Consequently, it provides the potential to monitor dynamic information on instantaneous energy and water fluxes at the land-surface–atmosphere interface. Nevertheless, the operational use of thermal remote sensing for hydrological and water resource management studies has been limited to regional scale applications (e.g., [1] and [2]) mainly because the spatial resolution (larger than 1 km) of current high temporal resolution thermal sensors is too coarse to represent the heterogeneity of man-made landscapes. For example, the Moderate Resolution Imaging Spectroradiometer (MODIS) has a revisit frequency of 1 or 2 times per day but a spatial resolution of only 1 km, while the Advanced Scanning Thermal Emission and Reflection radiometer (ASTER) has a spatial resolution of 90 m but a revisit time of only 16 days.

The use of remotely sensed land surface temperature over agricultural areas requires data at both high spatial and temporal resolutions [3]. While there is a lack of high spatial resolution thermal data from satellite with high frequency, there is the potential for land surface temperature derived from kilometric resolution sensors having high temporal resolution to be disaggregated using high spatial resolution ancillary data. The first disaggregation approach of remotely sensed temperature was developed by [4] using the fractional green vegetation cover derived from red and near-infrared reflectances. Given the high temperature difference between bare soil and a well-watered crop, this approach has proved to be effective over areas with relatively uniform soil and vegetation hydric status. Recently, [5] has extended the approach of [4] to conditions where vegetation hydric status is heterogeneous. This required developing a methodology to estimate the fraction of senescent vegetation cover from a time series of FORMOSAT-2 images.

Manuscript received December 2, 2010; revised June 28, 2011; accepted September 11, 2011. This work was supported in part by the French program Terre-Océan-Surfaces-Continentales-Atmosphère and in part by the Centre National de la Recherche Scientifique. The National Airborne Field Experiments have been made possible through infrastructure (LE0453434 and LE0560930) and research (DP0557543) funding from the Australian Research Council and the collaboration of a large number of scientists from throughout Australia, U.S., and Europe. Initial setup and maintenance of the study catchments were funded by a research Grant (DP0343778) from the Australian Research Council and by the CRC for Catchment Hydrology.

O. Merlin is with the Centre d'Etudes Spatiales de la Biosphère (CESBIO), 31401 Toulouse, France (e-mail: olivier.merlin@cesbio.cnes.fr).

F. Jacob (e-mail: frederic.jacob@supagro.inra.fr).

J.-P. Wigneron (e-mail: jpwigner@bordeaux.inra.fr).

J. Walker (e-mail: jeff.walker@monash.edu).

G. Chehbouni (e-mail: ghani.chehbouni@cesbio.cnes.fr).

Color versions of one or more of the figures in this paper are available online at http://ieeexplore.ieee.org.

Digital Object Identifier 10.1109/TGRS.2011.2169802

The accuracy in disaggregated temperature was improved by taking into account fractional senescent vegetation cover in addition to fractional green vegetation cover.

Fractional green and senescent vegetation covers, however, are not the only factors explaining the spatial variations of land surface temperature, especially over irrigated areas where crop fields may have different moisture status to the surrounds. In particular, the temperature over a flooded crop field may be drastically different from the temperature over a mature crop field. Therefore, the fraction of open water is an important variable to represent the spatial variations of land surface temperature. Over nonwatered land surfaces, the soil evaporative efficiency (ratio of actual to potential soil evaporation) is a signature of the capacity of the soil to evaporate its water content in the near surface and thus to counter an increase of its thermodynamic temperature. Consequently, soil evaporative efficiency is also an essential variable to describe the spatial variations of land surface temperature. Moreover, knowledge of soil evaporative efficiency is needed to decouple the effects of soil and vegetation hydric status on the surface energy budget and hence to better represent the resultant radiative surface temperature. As an example, the crop water stress index (CWSI) [6], [7] can be used to detect plant stress based on the difference between foliage and air temperature. Nevertheless, the application of the CWSI to partially vegetated areas is subjected to large uncertainties because the soil background may have a different temperature to the plants [7] depending on soil evaporative efficiency. Another example is provided by Moran *et al.* [8] who proposed the vegetation index/temperature (VIT) trapezoid to estimate a most probable range of plant stress over partially vegetated fields. It is a three-step procedure in which the following steps are performed: 1) the temperatures of the four vertices of the VIT trapezoid are estimated using an energy budget model; 2) the minimum and maximum probable vegetation temperatures are estimated from the measured composite land surface temperature, together with the maximum and minimum simulated soil temperatures; and 3) the minimum and maximum probable CWSIs are computed by normalizing the minimum and maximum probable vegetation temperatures from the vegetation temperature extremes simulated by the energy budget model. The point is that this approach does not allow estimating a single CWSI value because the retrieval problem is underdetermined. In particular, Moran *et al.* [8] noted that "with knowledge of a second point within the hourglass (perhaps soil temperature), it would be possible to infer [the canopy-air temperature] difference and pinpoint the CWSI value." In the latter case, knowledge of soil temperature is equivalent to knowledge of soil evaporative efficiency, which would remove the underdetermination of the VIT trapezoid.

The objective of this paper is to develop a new disaggregation methodology of kilometric land surface temperature using hectometric multivariable ancillary data. The approach is based on a radiative transfer equation that estimates differences in temperature data at hectometric resolution. Specifically, the use of a radiative transfer equation allows the following: 1) including variables other than those used by previous disaggregation approaches and 2) deducing the most pertinent variables. In addition to fractional green and senescent vegetation covers, the new methodology includes the variability at hectometric resolution of fractional open water and soil evaporative efficiency. With respect to other disaggregation algorithms in literature [4], [5], the proposed technique differs in the following four main aspects: 1) it relies on a physically based radiative transfer equation rather than empirical linear regressions; 2) it takes into account the fractional open water derived from shortwave-infrared band as required; 3) it takes into account the soil hydric status via microwave-derived soil evaporative efficiency; and 4) it allows the relative weight of each parameter used for disaggregating temperature to be quantified.

The new disaggregation technique is compared to the existing approaches using data collected during the National Airborne Field Experiment in 2006 (NAFE'06; [9]). The experimental site covers a 5 km by 32 km irrigated agricultural area, which included approximately 5% of flooded rice crops during NAFE'06. Disaggregation algorithms are first tested by aggregating ASTER temperature at 1-km resolution and by comparing the disaggregated temperature to the high-resolution ASTER temperature initially used in the aggregation process. The application to aggregated ASTER data allows evaluating approaches independently of differences between ASTER and MODIS products [5]. Disaggregation algorithms are then applied to MODIS data.

II. Experimental Data

The study area is a 5 km by 32 km area included in the Coleambally Irrigation Area (CIA) located in the flat western plains of the Murrumbidgee catchment in southeastern Australia (35° S, 146° E). The principal summer crops grown in the CIA are rice, maize, and soybeans, while winter crops include wheat, barley, oats, and canola. In November, rice crops are flooded under 30 cm height of irrigation water.

The NAFE'06 was conducted from October 31 to November 20, 2006, over a 40 km by 60 km area, with more detailed flights over the 5 km by 32 km focus area studied in this paper. While a full description of the NAFE'06 data set is given in [9], a brief overview of the most pertinent details is provided here. The data used in this paper are comprised of airborne L-band brightness temperature; ASTER red, near-infrared, and shortwave-infrared reflectances; ASTER land surface temperature data (resampled at 250-m resolution); MODIS land surface temperature data; and air temperature data collected by a meteorological station in the NAFE'06 area.

A. PLMR

The Polarimetric L-band Multibeam Radiometer (PLMR) is an airborne instrument that measures both H and V polarizations using a single receiver with polarization switching at view angles of $\pm 7°$, $\pm 21.5°$, and $\pm 38.5°$. The accuracy of the PLMR is estimated to be better than 2 K and 3 K in the H and V polarization, respectively [10].

During NAFE'06, the PLMR flew on November 14 to collect L-band brightness temperature at 250-m resolution over the 5 km by 32 km area in the CIA. PLMR was mounted in the across-track configuration so that each pixel was observed at a

given incidence angle (approximately 7°, 21.5°, or 38.5°). Data were processed for incidence angle and beam location on the ground by taking into account aircraft position, attitude, and ground topography.

As the sensitivity to soil moisture is higher for H-polarized brightness temperature than for V-polarized brightness temperature, only the H-polarized brightness temperature TB is used in this paper. Preprocessing of TB consists of the following: 1) resampling H-polarized PLMR data at 250-m resolution on a grid that matches in symmetry to the flight lines over the 5 km by 32 km area and 2) converting the resampled TB to an equivalent value at 21.5° incidence angle. The incidence angle 21.5° is chosen to minimize conversion errors. The angular conversion involves the brightness temperature collected by inner beams at approximately 7° incidence angle being multiplied by the ratio $\overline{TB_{\rm MB}}/\overline{TB_{\rm IB}}$, with $\overline{TB_{\rm MB}}$ and $\overline{TB_{\rm IB}}$ being the mean brightness temperatures collected by the middle and inner beams, respectively. Similarly, the brightness temperature collected by the outer beams at approximately 38.5° incidence angle is multiplied by the ratio $\overline{TB_{\rm MB}}/\overline{TB_{\rm OB}}$, with $\overline{TB_{\rm OB}}$ being the mean brightness temperature collected by the outer beams. Mean brightness temperatures $\overline{TB_{\rm IB}}$, $\overline{TB_{\rm MB}}$, and $\overline{TB_{\rm OB}}$ are computed as the average (for all flight lines) of the TB collected by the beams pointing at $\pm 7°$, $\pm 21.5°$, and $\pm 38.5°$, respectively. This technique was already used in [11] to generate TB images by assuming that the impact of soil moisture and biomass on the angular dependance of TB is negligible or small. In this paper, a slightly different approach is adopted to take into account the variations in aircraft attitude during data collection, which made the incidence angle θ oscillate around 7°, 21.5°, and 38.5°. The brightness temperature $TB(\theta)$ observed at the incidence angle θ is multiplied by the ratio $\overline{TB_{\rm MB}}/\overline{TB_{\rm interp}(\theta)}$, with $\overline{TB_{\rm interp}(\theta)}$ being the mean brightness temperature linearly interpolated at θ incidence angle from the mean data collected by the inner, middle, and outer beams.

B. ASTER

The ASTER instrument was launched in 1999 aboard Terra, a sun synchronous platform with 11:00 UTC descending Equator crossing and a 16-day revisit cycle. An ASTER scene covers an area of approximately 60 km by 60 km and consists of 14 nadir-looking bands and one oblique-looking band to create stereo-based digital elevation models. The three nadir-looking bands in the visible and near infrared have a 15-m resolution. The six bands in the shortwave-infrared have a 30-m resolution. Finally, there are five thermal infrared bands with a 90-m resolution.

The ASTER overpass of the NAFE'06 site was on November 16, 2006. Official ASTER products [12] were used here for surface reflectance (AST_07) and radiometric temperature (AST_08) with accuracies of 5% and 1.5 K, respectively [13]–[19]. They were downloaded from the Earth Observing System Data Gateway (EDG).

ASTER 15-m resolution red (B2) and near-infrared (B3) bands were extracted over the 5 km by 32 km area and resampled at 250-m resolution to match the spatial resolution and extent of PLMR observations. The ASTER 30-m resolution B5 band (1.60–1.70 μm) was extracted over the 5 km by 32 km study area and resampled at 50-m resolution. Fractional open water was estimated using B5 band [20] based on a threshold method. Consequently, B5 data were resampled at a resolution finer than that (250 m) of PLMR data to classify open water pixels at 50-m resolution and to obtain fractional open water at 250-m resolution from the binary classification. ASTER 90-m resolution radiometric temperature was extracted over the 5 km by 32 km area and aggregated at 250-m resolution to match the spatial resolution and extent of PLMR observations. Aggregation was achieved by linearly averaging high-resolution surface temperatures, i.e., without accounting for the nonlinear relationship between physical temperature and radiance. This choice was motivated by the results of [21], which compared the temperature aggregated using different scaling approaches and obtained very low differences (maximum difference of 0.2 °C).

C. MODIS

The MODIS/Terra data were collected concurrently with ASTER data. MODIS official products consisted of the 928-m resolution surface skin temperature (MOD11-L2) retrieved by the "generalized split window" algorithm [22]–[24] and registered in the sinusoidal projection. The MODIS Reprojection Tool was used to project MOD11-L2 data in UTM WGS 1984 55S with a sampling interval of 1 km.

In this paper, the disaggregation of 1-km MODIS temperature is evaluated using high-resolution ASTER data. To distinguish the errors associated with the disaggregation technique and the errors associated with the discrepancy between MODIS and ASTER temperature products, a comparison is made between ASTER and MODIS data at 1-km resolution over the 5 km by 32 km study area. The ASTER data are aggregated at the MODIS spatial resolution (1 km) by linearly averaging high-resolution temperatures. The root-mean-square difference (RMSD), bias, correlation coefficient, and slope of the linear regression between MODIS and aggregated ASTER data are 2.7 °C, −2.3 °C, 0.75, and 0.52, respectively. The discrepancy between MODIS and ASTER data, which is mainly explained here by a significant bias and a relatively low slope of the linear regression, is on the same order of magnitude as the mean difference (about 3 °C) reported in literature [5], [21], [25].

III. Disaggregation Algorithms

This paper aims to compare different approaches for disaggregating kilometric MODIS land surface temperature data. The study uses aggregated ASTER and real MODIS data and demonstrates the disaggregation at 250-m resolution. The resolution of 250 m is chosen to match with the lowest resolution at which ancillary data composed of red, near-infrared, shortwave-infrared, and microwave-L bands are available. In this case study, the target scale is determined by the resolution (250 m) of airborne microwave data.

As shown in the schematic diagram of Fig. 1, the disaggregation algorithms are noted as Dk, with k being the number of factors taken into account in the disaggregation. The new

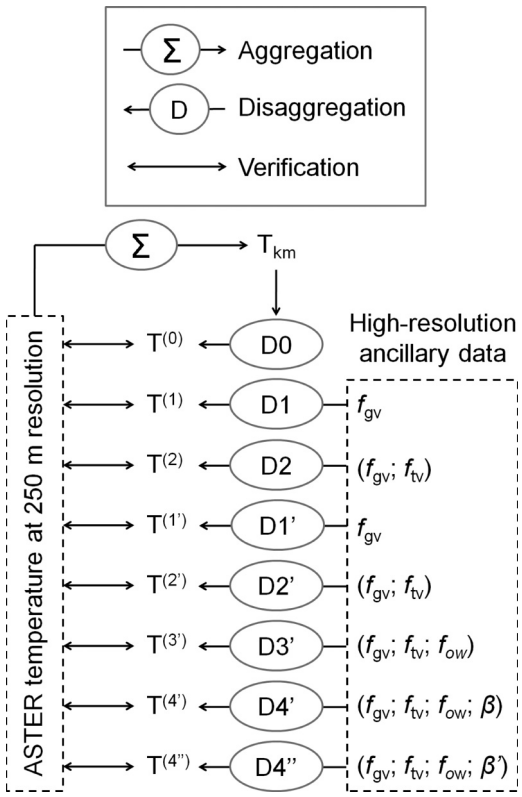

Fig. 1. Schematic diagram presenting the different disaggregation algorithms of kilometric temperature $T_{\rm km}$ and the verification strategy at high (250 m) resolution.

algorithms are noted as Dk$'$. D0 does not use any ancillary data, while D1 is based on a linear regression between land surface temperature and fractional green (photosynthetically active) vegetation cover. Fractional green vegetation cover $f_{\rm gv}$ is defined as the surface area of green vegetation per unit area of soil. D1 is the same as in [4]. D2 is based on D1 but takes into account both fractional green and total vegetation covers. Fractional vegetation cover $f_{\rm tv}$ is defined as the total surface area of (green plus senescent) vegetation per unit area of soil. D2 is the same as in [5]. The new algorithms D1$'$, D2$'$, D3$'$, and D4$'$ (and D4$''$) are all derived from a radiative transfer equation. The four algorithms differ with regard to the number of factors which are explicitly taken into account. D1$'$ includes the variability of $f_{\rm gv}$ and is thus a substitute for D1 based on radiative transfer. D2$'$ includes the variability of both $f_{\rm gv}$ and $f_{\rm tv}$ and is thus a substitute for D2 based on radiative transfer. The other algorithms D3$'$ and D4$'$ integrate additional variables. D3$'$ includes the variability of $f_{\rm gv}$, $f_{\rm tv}$, and fractional open water $f_{\rm ow}$. D4$'$ includes the variability of $f_{\rm gv}$, $f_{\rm tv}$, $f_{\rm ow}$, and soil evaporative efficiency (ratio of actual to potential soil evaporation) β. D4$''$ is the same as D4$'$ but with a different formulation for soil evaporative efficiency.

D0 sets the disaggregated temperature as

$$T^{(0)} = T_{\rm km} \tag{1}$$

with $T_{\rm km}$ being the land surface temperature observed at kilometric resolution.

Using D1, the disaggregated temperature is computed as

$$T^{(1)} = T_{\rm km} + \mathbf{a_1} \times (f_{\rm gv} - \langle f_{\rm gv}\rangle_{\rm km}) \tag{2}$$

with $f_{\rm gv}$ being the fractional green vegetation cover derived at high resolution, $\langle f_{\rm gv}\rangle_{\rm km}$ being the $f_{\rm gv}$ aggregated at kilometric resolution, and $\mathbf{a_1}$ being the slope of the linear regression between $T_{\rm km}$ and $\langle f_{\rm gv}\rangle_{\rm km}$. Note that the variables defined at kilometric resolution are noted with the subscript km.

Using D2, the disaggregated temperature is computed as

$$T^{(2)} = T_{\rm km} + \mathbf{a_1^{proj}} \times \left(f_{\rm gv}^{\rm proj} - \langle f_{\rm gv}\rangle_{\rm km}\right) \tag{3}$$

with $f_{\rm gv}^{\rm proj}$ being the projected $f_{\rm gv}$ and $\mathbf{a_1^{proj}}$ being the slope of the linear regression between $T_{\rm km}$ and the projected $f_{\rm gv}$ estimated at kilometric resolution $f_{\rm gv,km}^{\rm proj}$. Note that the variables defined at the image scale are written in bold. The notion of a "projected variable" was introduced in [26]. It is a robust tool that strenghtens the correlation between two variables by representing the dependence of these variables on other additional variables. In [5], the projection technique was applied to fractional green vegetation cover to artificially improve the spatial correlation between T and $f_{\rm gv}$ by taking into account the dependence of T on $f_{\rm tv}$. The projected fractional green vegetation cover is computed as

$$f_{\rm gv}^{\rm proj} = f_{\rm gv} - \frac{\mathbf{T_{fcsv}} - (\mathbf{T_{b,ds}} + \mathbf{T_{b,ws}})/2}{\mathbf{T_{fcsv}} - \mathbf{T_{fcgv}}} \times (f_{\rm tv} - \langle f_{\rm tv}\rangle_{\rm km}) \tag{4}$$

with $f_{\rm tv}$ being the fractional total vegetation cover derived at high resolution, $\langle f_{\rm tv}\rangle_{\rm km}$ being the $f_{\rm tv}$ aggregated at kilometric resolution, $\mathbf{T_{b,ws}}$ being the temperature of wet bare soil, $\mathbf{T_{b,ds}}$ being the temperature of dry bare soil, $\mathbf{T_{fcgv}}$ being the temperature of full-cover green vegetation, and $\mathbf{T_{fcsv}}$ being the temperature of full-cover senescent vegetation (notations are summarized in Table I). Following the interpretation of the "triangle method" [27], $\mathbf{T_{b,ws}}$, $\mathbf{T_{b,ds}}$, $\mathbf{T_{fcgv}}$, and $\mathbf{T_{fcsv}}$ correspond to the minimum and maximum soil and vegetation temperatures within the study area, respectively. It is reminded that $f_{\rm tv} = f_{\rm gv} + f_{\rm sv}$, with $f_{\rm gv}$ and $f_{\rm sv}$ being the fractional green and senescent vegetation covers, respectively.

In (4), the projected fractional green vegetation cover estimated at kilometric resolution is

$$f_{\rm gv,km}^{\rm proj} = \langle f_{\rm gv}\rangle_{\rm km} - \frac{\mathbf{T_{fcsv}} - (\mathbf{T_{b,ds}} + \mathbf{T_{b,ws}})/2}{\mathbf{T_{fcsv}} - \mathbf{T_{fcgv}}} \times (\langle f_{\rm tv}\rangle_{\rm km} - \mathbf{f_{tv}}) \tag{5}$$

with $\mathbf{f_{tv}}$ being the mean $f_{\rm tv}$ over the whole study area.

The new algorithms D$'$ use a radiative transfer equation to model the spatial variability of disaggregated temperature within each 1-km resolution pixel, using ancillary data available at high resolution such as $f_{\rm gv}$, $f_{\rm tv}$, $f_{\rm ow}$, and β. D1$'$ is a substitute for D1 based on radiative transfer. It expresses disaggregated temperature as

$$T^{(1')} = T_{\rm km} + \Delta T^{(1')} \tag{6}$$

TABLE I
INTERPRETATION OF THE VERTICES IN THE GENERALIZED "TRIANGLE APPROACH"

Vertex	Surface type	Near-surface soil hydric status	Abbreviation
A	Bare soil	Dry	b,ds
B	Bare soil	Wet	b,ws
C	Full-cover green vegetation	Wet or dry	fcgv
C′	Full-cover green vegetation	Wet	fcgv,ws
C″	Full-cover green vegetation	Dry	fcgv,ds
D	Full-cover senescent vegetation	Wet or dry	fcsv
D′	Full-cover senescent vegetation	Dry	fcsv,ds

with $\Delta T^{(1')}$ being the difference between the temperature simulated using high-resolution $f_{\rm gv}$ and that aggregated within the 1-km resolution pixel

$$\Delta T^{(1')} = T_{\rm mod}\ (f_{\rm gv}, \langle f_{\rm tv}\rangle_{\rm km}, \langle f_{\rm ow}\rangle_{\rm km}, \langle\beta\rangle_{\rm km}) - \langle T_{\rm mod}\ (f_{\rm gv}, \langle f_{\rm tv}\rangle_{\rm km}, \langle f_{\rm ow}\rangle_{\rm km}, \langle\beta\rangle_{\rm km})\rangle_{\rm km} \quad (7)$$

with $T_{\rm mod}$ being the land surface temperature simulated by a radiative transfer equation. In (7), fractional total vegetation cover, fractional open water, and soil evaporative efficiency are set to their values aggregated at kilometric resolution. Therefore, only the variability of $f_{\rm gv}$ is taken into account at high resolution.

D2′ is a substitute for D2 based on radiative transfer. It expresses the disaggregated temperature as in (6), with the simulated temperature difference $\Delta T^{(2')}$ written as

$$\Delta T^{(2')} = T_{\rm mod}\ (f_{\rm gv}, f_{\rm tv}, \langle f_{\rm ow}\rangle_{\rm km}, \langle\beta\rangle_{\rm km}) - \langle T_{\rm mod}\ (f_{\rm gv}, f_{\rm tv}, \langle f_{\rm ow}\rangle_{\rm km}, \langle\beta\rangle_{\rm km})\rangle_{\rm km}. \quad (8)$$

D3′ is derived from the same radiative transfer equation and includes the variability of $f_{\rm gv}$, $f_{\rm tv}$, and $f_{\rm ow}$ at high resolution. It determines the disaggregated temperature using (6) but with the simulated temperature difference $\Delta T^{(3')}$ written as

$$\Delta T^{(3')} = T_{\rm mod}\ (f_{\rm gv}, f_{\rm tv}, f_{\rm ow}, \langle\beta\rangle_{\rm km}) - \langle T_{\rm mod}\ (f_{\rm gv}, f_{\rm tv}, f_{\rm ow}, \langle\beta\rangle_{\rm km})\rangle_{\rm km}. \quad (9)$$

D4′ is derived from the same radiative transfer equation and includes the variability of $f_{\rm gv}$, $f_{\rm tv}$, $f_{\rm ow}$, and β at high resolution. It determines the disaggregated temperature using (6) but with the simulated temperature difference $\Delta T^{(4')}$ written as

$$\Delta T^{(4')} = T_{\rm mod}\,(f_{\rm gv}, f_{\rm tv}, f_{\rm ow}, \beta) - \langle T_{\rm mod}\,(f_{\rm gv}, f_{\rm tv}, f_{\rm ow}, \beta)\rangle_{\rm km}. \quad (10)$$

D4″ is an extension of (10) to replace β by another formulation of soil evaporative efficiency noted as β'.

The high- to low-resolution simulated temperature difference in (7)–(10) is computed using a linearized radiative transfer equation [5], [28], [29]. Modeled land surface temperature $T_{\rm mod}$ is written as

$$T_{\rm mod} = f_{\rm ow}T_{\rm ow} + (1 - f_{\rm ow})T_{\rm nw} \quad (11)$$

with $T_{\rm ow}$ being the surface temperature of a water body and $T_{\rm nw}$ being the skin temperature of a nonwatered land surface. Nonwatered land surface temperature is expressed as

$$T_{\rm nw} = f_{\rm gv}\mathbf{T_{fcgv}} + (f_{\rm tv} - f_{\rm gv})\mathbf{T_{fcsv}} + (1 - f_{\rm tv})T_{\rm bs} \quad (12)$$

with $\mathbf{T_{fcgv}}$ and $\mathbf{T_{fcsv}}$ being the temperature of full-cover green and senescent vegetations, respectively, and $T_{\rm bs}$ being the bare soil temperature. With the soil evaporative efficiency defined [30] as

$$\beta = \frac{\mathbf{T_{b,ds}} - T_{\rm bs}}{\mathbf{T_{b,ds}} - \mathbf{T_{b,ws}}} \quad (13)$$

the bare soil temperature can be expressed as

$$T_{\rm bs} = \beta\mathbf{T_{b,ws}} + (1 - \beta)\mathbf{T_{b,ds}}. \quad (14)$$

By assuming that water temperature is close to well-watered green vegetation [27], modeled land surface temperature becomes

$$T_{\rm mod} = f_{\rm ow}\mathbf{T_{fcgv}} + (1 - f_{\rm ow})T_{\rm nw} \quad (15)$$

with the nonwatered land surface temperature expressed as

$$T_{\rm nw} = f_{\rm gv}\mathbf{T_{fcgv}} + (f_{\rm tv} - f_{\rm gv})\mathbf{T_{fcsv}} + (1 - f_{\rm tv})\left[\beta\mathbf{T_{b,ws}} + (1 - \beta)\mathbf{T_{b,ds}}\right]. \quad (16)$$

The temperature extremes $\mathbf{T_{b,ds}}$, $\mathbf{T_{b,ws}}$, $\mathbf{T_{fcgv}}$, and $\mathbf{T_{fcsv}}$ are extrapolated (according to Section V) from low-resolution land surface temperatures using high-resolution ancillary data [5].

IV. DERIVATION OF BIOPHYSICAL VARIABLES

The four variables used by the disaggregation methodology are the following: fractional green vegetation cover $f_{\rm gv}$, fractional total (green plus senescent) vegetation cover $f_{\rm tv}$, fractional open water $f_{\rm ow}$, and soil evaporative efficiency β. All of these variables are estimated from ASTER red, near-infrared, and shortwave-infrared reflectance products and from the PLMR H-polarized brightness temperature converted at an incidence angle of 21.5°.

A. Fractional Green Vegetation Cover

Fractional green vegetation cover can be estimated from the Normalized Difference Vegetation Index (NDVI) as in [31]

$$f_{\rm gv} = \frac{\rm NDVI - \mathbf{NDVI_{bs}}}{\mathbf{NDVI_{fcgv}} - \mathbf{NDVI_{bs}}} \quad (17)$$

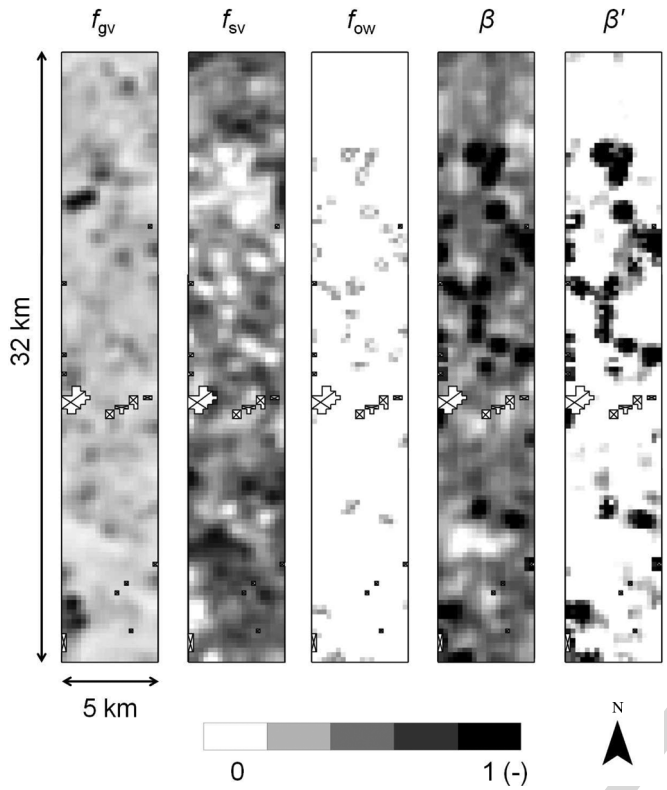

Fig. 2. Images of fractional green vegetation cover $f_{\rm gv}$, fractional senescent vegetation cover $f_{\rm sv} = f_{\rm tv} - f_{\rm gv}$, fractional open water $f_{\rm ow}$, soil evaporative efficiency β, and soil evaporative efficiency β'. Note that 2% of the 5 km by 32 km area is contaminated by clouds and cloud shadow. Contaminated 250-m resolution pixels are represented by crossed-out surfaces.

with $\mathbf{NDVI_{bs}}$ and $\mathbf{NDVI_{fcgv}}$ being the NDVI over bare soil and full-cover green vegetation, respectively. NDVI is computed as the difference between near-infrared and red bands divided by their sum. The spatial variation of fractional green vegetation cover over the study area is shown in Fig. 2.

B. Fractional Total (Green Plus Senescent) Vegetation Cover

Fractional total vegetation cover is estimated by correlating $f_{\rm tv}$ with surface albedo for green vegetation and by setting $f_{\rm tv}$ to the maximum $f_{\rm gv}$ for senescent vegetation. This methodology [5] is based on two assumptions, which are generally met in agricultural areas: 1) soil albedo is generally lower than green vegetation albedo, and 2) green vegetation albedo is lower than senescent vegetation albedo. Although a time series of red and near-infrared data would be required to estimate soil albedo and green vegetation albedo on a pixel-by-pixel basis [5], only one ASTER scene is available for this study period. Therefore, an alternate approach is adopted. Surface albedo is modeled as a linear mixing of vegetation and soil components (e.g., [32] and [33])

$$\alpha = (1 - f_{\rm tv})\alpha_{\mathbf{bs}} + f_{\rm gv}\alpha_{\mathbf{fcgv}} + (f_{\rm tv} - f_{\rm gv})\alpha_{\mathbf{fcsv}} \qquad (18)$$

with $\alpha_{\mathbf{bs}}$, $\alpha_{\mathbf{fcgv}}$, and $\alpha_{\mathbf{fcsv}}$ being the albedo for bare soil, full-cover green vegetation, and full-cover senescent vegetation, respectively, and with the end-members $\alpha_{\mathbf{bs}}$, $\alpha_{\mathbf{fcgv}}$, and $\alpha_{\mathbf{fcsv}}$ estimated in Section V.

By inverting (18), fractional vegetation cover is expressed as

$$f_{\rm tv} = \frac{\alpha - \alpha_{\mathbf{bs}} + f_{\rm gv}(\alpha_{\mathbf{fcsv}} - \alpha_{\mathbf{fcgv}})}{\alpha_{\mathbf{fcsv}} - \alpha_{\mathbf{bs}}} \qquad (19)$$

with α being the surface albedo estimated as a weighted sum of red and near-infrared reflectances using the coefficients given in [34] and validated in [35]–[38]. As stated previously, our case study does not allow calibrating $\alpha_{\mathbf{bs}}$, $\alpha_{\mathbf{fcgv}}$, and $\alpha_{\mathbf{fcsv}}$ on a pixel-by-pixel basis. Consequently, the value of $f_{\rm tv}$ computed from (19) may, on some occasions, be lower than $f_{\rm gv}$ or larger than 1. To avoid nonphysical values, $f_{\rm tv}$ is set to $f_{\rm gv}$ and 1 in the former and latter case, respectively.

The spatial variation of fractional senescent vegetation cover ($f_{\rm sv} = f_{\rm tv} - f_{\rm gv}$) over the study area is shown in Fig. 2. Note that NAFE'06 was undertaken at the beginning of the summer agricultural season so that all irrigated crops were green and healthy.

C. Fractional Open Water

The fraction of open water within each 250-m resolution pixel is estimated using 50-m resolution resampled ASTER B5 reflectance product. Various studies have indicated that the shortwave-infrared band centered at around 1 μm is highly sensitive to the presence of open water [20], [39], [40]. In this paper, a simple threshold method is applied to classify at 50-m resolution the 5 km by 32 km area in two classes: water and nonwatered surface. The threshold value is estimated as 0.170 from one flooded crop field in the south of the study area. The spatial variation of fractional open water over the study area is shown in Fig. 2. Open water represents 5% of the study area and is attributed to rice cropping.

D. Soil Evaporative Efficiency

Soil evaporative efficiency β is defined as the ratio of actual to potential soil evaporation. In this paper, β is estimated from PLMR brightness temperatures. Two different formulations are used to evaluate the coupling effects of near-surface soil moisture, $f_{\rm gv}$, and $f_{\rm sv}$ on microwave-derived soil evaporative efficiency.

By assuming that brightness temperature is mainly sensitive to surface soil moisture [41] and that soil evaporative efficiency is mainly driven by surface soil moisture [42], [43], soil evaporative efficiency can be estimated as

$$\beta = 1 - \frac{TB - \mathbf{TB_{b,ws}}}{\mathbf{TB_{fcsv,ds}} - \mathbf{TB_{b,ws}}} \qquad (20)$$

with $\mathbf{TB_{b,ws}}$ and $\mathbf{TB_{fcsv,ds}}$ being the minimum and maximum brightness temperatures observed over the study area, respectively. As brightness temperature generally decreases with surface soil moisture and increases with vegetation cover [44], $\mathbf{TB_{b,ws}}$ and $\mathbf{TB_{fcsv,ds}}$ are interpreted as the brightness temperatures over wet bare soil and full-cover senescent vegetation with dry soil, respectively. The spatial variation of β over the study area is shown in Fig. 2.

Since brightness temperature also depends on biomass (e.g., [45]), a second formulation of soil evaporative efficiency β' is

TABLE II
NDVI AND SURFACE ALBEDO END-MEMBERS

End-member	Value	Unit
$\mathbf{NDVI_{bs}}$	0.15	-
$\mathbf{NDVI_{fcgv}}$	0.65	-
$\alpha_{\mathbf{bs}}$	0.17	-
$\alpha_{\mathbf{fcgv}}$	0.22	-
$\alpha_{\mathbf{fcsv}}$	0.31	-

derived in order to decouple the effects of soil moisture, $f_{\rm gv}$, and $f_{\rm sv}$ on TB. As in [46], the assumption is that, for a given vegetated pixel, if vegetation is partially stressed (i.e., $f_{\rm sv} > 0$ or $f_{\rm tv} > f_{\rm gv}$), then near-surface soil moisture availability is zero (i.e., $\beta' = 0$). Alternatively, if that pixel does not contain senescent vegetation (i.e., $f_{\rm sv} = 0$ or $f_{\rm tv} = f_{\rm gv}$), then β' is computed as the ratio of the measured "wet soil" brightness temperature difference to the "dry soil"–"wet soil" brightness temperature difference. Formally, one writes

$$\beta' = 0 \quad \text{if} \quad TB > TB_{\mathbf{ds}} \tag{21}$$

$$\beta' = 1 - \frac{TB - TB_{\mathbf{ws}}}{TB_{\mathbf{ds}} - TB_{\mathbf{ws}}} \quad \text{if} \quad TB \leq TB_{\mathbf{ds}} \tag{22}$$

with $TB_{\mathbf{ds}}$ and $TB_{\mathbf{ws}}$ being the "dry soil" and "wet soil" brightness temperatures, respectively, both being estimated for $f_{\rm sv} = 0$. Since green vegetation is partially transparent to microwaves, the "dry soil" brightness temperature is computed as a weighted sum of the brightness temperature over dry bare soil (noted as $\mathbf{TB_{b,ds}}$) and the brightness temperature over full-cover green vegetation with dry soil (noted as $\mathbf{TB_{fcgv,ds}}$)

$$TB_{\mathbf{ds}} = f_{\rm gv}\mathbf{TB_{fcgv,ds}} + (1 - f_{\rm gv})\mathbf{TB_{b,ds}}. \tag{23}$$

Similarly, the "wet soil" brightness temperature is computed as a weighted sum of the brightness temperature over wet bare soil (noted as $\mathbf{TB_{b,ws}}$) and the brightness temperature over full-cover green vegetation with wet soil (noted as $\mathbf{TB_{fcgv,ws}}$)

$$TB_{\mathbf{ws}} = f_{\rm gv}\mathbf{TB_{fcgv,ws}} + (1 - f_{\rm gv})\mathbf{TB_{b,ws}}. \tag{24}$$

The spatial variation of β' over the study area is shown in Fig. 2.

V. ESTIMATING END-MEMBERS

A key step in the disaggregation procedure is estimating the 14 end-members from ASTER and PLMR data. They are composed of the following: $\mathbf{NDVI_{bs}}$, $\mathbf{NDVI_{fcgv}}$, $\alpha_{\mathbf{bs}}$, $\alpha_{\mathbf{fcgv}}$, $\alpha_{\mathbf{fcsv}}$, $\mathbf{T_{b,ws}}$, $\mathbf{T_{b,ds}}$, $\mathbf{T_{fcgv}}$, $\mathbf{T_{fcsv}}$, $\mathbf{TB_{b,ws}}$, $\mathbf{TB_{b,ds}}$, $\mathbf{TB_{fcgv,ws}}$, $\mathbf{TB_{fcgv,ds}}$, and $\mathbf{TB_{fcsv,ds}}$. For the convenience of the reader, the unit is degree Celsius for radiometric temperature and kelvin for brightness temperature.

A. NDVI

NDVI end-members are estimated as the minimum and maximum values of NDVI observed over the 5 km by 32 km area for bare soil and full-cover green vegetation, respectively. Values for $\mathbf{NDVI_{bs}}$ and $\mathbf{NDVI_{fcgv}}$ are reported in Table II.

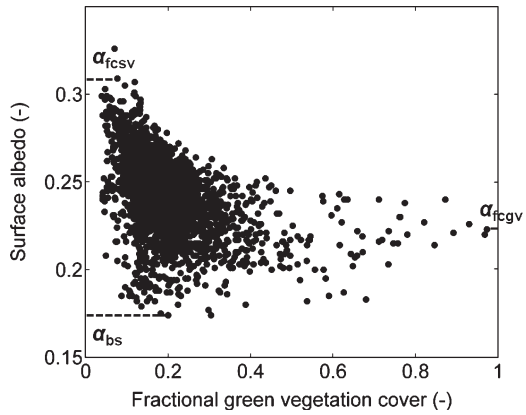

Fig. 3. ASTER surface albedo α plotted against ASTER fractional green vegetation cover $f_{\rm gv}$. Three particular values of α are identified: the soil albedo $\alpha_{\mathbf{bs}}$ estimated as the minimum surface albedo, the green vegetation albedo $\alpha_{\mathbf{fcgv}}$ estimated as the albedo corresponding to the largest $f_{\mathbf{gv}}$, and the senescent vegetation albedo $\alpha_{\mathbf{fcsv}}$ estimated as the maximum surface albedo.

In this paper, the study domain included extreme conditions in terms of vegetation cover so that NDVI end-members could be estimated from the red and near-infrared reflectances acquired over the area on a single date. In the case where extreme conditions are not encountered in the application domain, a different approach should be adopted, such as the use of a time series of NDVI data (instead of a single snapshot image) that would capture the phenological stages of agricultural crops. Also, the determination of reflectance end-members could be further constrained by the use of ancillary spectral data sets [47].

B. Albedo

Fig. 3 shows the space defined by surface albedo α and fractional green vegetation cover $f_{\rm gv}$. Pixels including open water are removed from the scatterplot. The soil albedo $\alpha_{\mathbf{bs}}$ is defined as the minimum ASTER surface albedo observed within the study area by assuming that the dependence of $\alpha_{\mathbf{bs}}$ on soil moisture is small compared to the dependence of α on vegetation cover. The green vegetation albedo $\alpha_{\mathbf{fcgv}}$ is estimated as the surface albedo corresponding to maximum fractional green vegetation cover. The senescent vegetation albedo $\alpha_{\mathbf{fcsv}}$ is estimated as the maximum surface albedo observed within the study area. Values for $\alpha_{\mathbf{bs}}$, $\alpha_{\mathbf{fcgv}}$, and $\alpha_{\mathbf{fcsv}}$ are reported in Table II.

C. Land Surface Temperature

As the range of surface conditions varies with spatial resolution, two different procedures are developed to estimate temperature end-members.

1) When estimating temperature end-members from 250-m resolution data, one pixel is identified as fully covered green vegetation, one pixel as fully covered senescent vegetation, one pixel as bare dry soil, and one pixel as bare wet soil. In this case, it is assumed that all extreme conditions are included at high resolution within the study domain.

TABLE III
LAND SURFACE TEMPERATURE AND L-BAND BRIGHTNESS TEMPERATURE END-MEMBERS THAT ARE ESTIMATED FROM HIGH-RESOLUTION ASTER TEMPERATURE DATA, EXTRAPOLATED FROM AGGREGATED ASTER TEMPERATURE DATA, AND EXTRAPOLATED FROM MODIS TEMPERATURE DATA. FOR THE CONVENIENCE OF THE READER, THE UNIT IS DEGREE CELSIUSFOR RADIOMETRIC TEMPERATURE AND KELVIN FOR BRIGHTNESS TEMPERATURE

End-member	High-resolution T	Aggregated ASTER T_{km}	MODIS T_{km}	Unit
$\mathbf{T_{b,ds}}$	38	40.2	38.9	°C
$\mathbf{T_{b,ws}}$	25	27.6	26.2	°C
$\mathbf{T_{fcgv}}$	21	21.0	21.0	°C
$\mathbf{T_{fcsv}}$	34	32.0	28.7	°C
$\mathbf{TB_{b,ds}}$	240	246	241	K
$\mathbf{TB_{b,ws}}$	190	193	193	K
$\mathbf{TB_{fcgv,ws}}$	205	205	205	K
$\mathbf{TB_{fcgv,ds}}$	240	240	240	K
$\mathbf{TB_{fcsv,ds}}$	280	280	280	K

2) When estimating temperature end-members from 1-km resolution data (as in the operational scenario), none of the pixels are identified as representative of any extreme condition. Temperature end-members are extrapolated from 1-km temperature data using ancillary data composed of air temperature, soil albedo, green vegetation albedo, and senescent vegetation albedo as described in the following.

End-members $\mathbf{T_{b,ws}}$, $\mathbf{T_{b,ds}}$, $\mathbf{T_{fcgv}}$, and $\mathbf{T_{fcsv}}$ are determined by analyzing the consistency of the diagrams in Fig. 4. Fig. 4(a) shows the space defined by ASTER land surface temperature and ASTER fractional green vegetation cover. The three edges of the triangle $T - f_{\mathrm{gv}}$ are interpreted [27] as "bare soil" between $\mathbf{A}$ and $\mathbf{B}$, "wet surface" between $\mathbf{B}$ and $\mathbf{C}$, and "dry soil" between $\mathbf{C}$ and $\mathbf{A}$. Fig. 4(b) shows the space defined by ASTER land surface temperature and ASTER surface albedo. An interpretation of the polygon $T - \alpha$ is provided in [5], which is consistent with the triangle method. The four edges are interpreted as "bare soil" between $\mathbf{A}$ and $\mathbf{B}$, "wet surface" between $\mathbf{B}$ and $\mathbf{C}$, "full cover" between $\mathbf{C}$ and $\mathbf{D}$, and "dry surface" between $\mathbf{D}$ and $\mathbf{A}$. The notation system for polygon vertices $\mathbf{A}$, $\mathbf{B}$, $\mathbf{C}$, and $\mathbf{D}$ is summarized in Table I, and the corresponding temperature values $\mathbf{T_{b,ds}}$, $\mathbf{T_{b,ws}}$, $\mathbf{T_{fcgv}}$, and $\mathbf{T_{fcsv}}$ are reported in Table III.

In this paper, high-resolution temperature T is assumed to be unavailable. Consequently, the extreme temperatures $\mathbf{T_{b,ds}}$, $\mathbf{T_{b,ws}}$, $\mathbf{T_{fcgv}}$, and $\mathbf{T_{fcsv}}$ are extrapoled from the spaces $T_{\mathrm{km}} - \langle f_{\mathrm{gv}} \rangle_{\mathrm{km}}$ and $T_{\mathrm{km}} - \langle \alpha \rangle_{\mathrm{km}}$ defined at kilometric resolution (see Fig. 4(c) and (d) for aggregated ASTER temperature and Fig. 4(e) and (f) for MODIS temperature). An approach similar to [5] is used as follows.

1) Vertex $\mathbf{C}$ corresponds to full-cover green vegetation and is located at $(1, \mathbf{T_{fcgv}})$ in Fig. 4(c) (Fig. 4(e) for MODIS temperature) and at $(\alpha_{\mathbf{fcgv}}, \mathbf{T_{fcgv}})$ in Fig. 4(d) [Fig. 4(f)]. In this paper, $\mathbf{T_{fcgv}}$ is set to the air temperature $\mathbf{T_a}$ measured at the time of ASTER overpass. Vertex $\mathbf{C}$ is thus placed at $(1, \mathbf{T_a})$ in Fig. 4(c) [Fig. 4(e)] and at $(\alpha_{\mathbf{fcgv}}, \mathbf{T_a})$ in Fig. 4(d) [Fig. 4(f)].

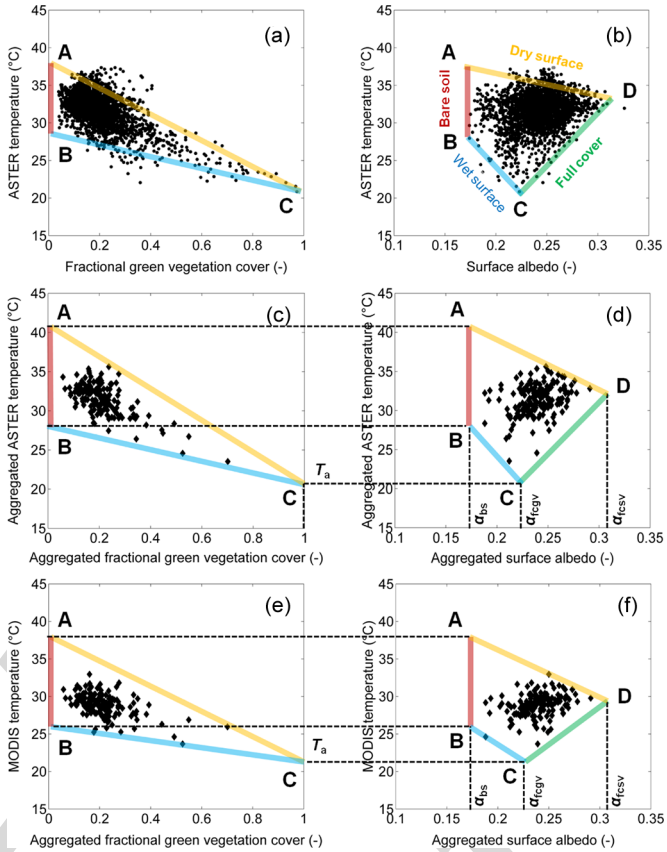

Fig. 4. (a) Scatterplot of ASTER temperature versus fractional green vegetation cover and (b) versus surface albedo, (c) scatterplot of aggregated ASTER temperature versus aggregated fractional green vegetation cover and (d) versus aggregated surface albedo, and (e) scatterplot of MODIS temperature versus aggregated fractional green vegetation cover and (f) versus aggregated surface albedo. The vertices $\mathbf{A}$, $\mathbf{B}$, $\mathbf{C}$, and $\mathbf{D}$ obtained using high-resolution data in (a) and (b) are extrapolated using low-resolution data in (c), (d), (e), and (f) from ancillary data composed of air temperature $\mathbf{T_a}$, soil albedo $\alpha_{\mathbf{bs}}$, green vegetation albedo $\alpha_{\mathbf{fcgv}}$, and senescent vegetation albedo $\alpha_{\mathbf{fcsv}}$.

2) Vertex $\mathbf{B}$ corresponds to wet bare soil and is located at $(0, \mathbf{T_{b,ws}})$ in Fig. 4(c) [Fig. 4(e)] and at $(\alpha_{\mathbf{bs}}, \mathbf{T_{b,ws}})$ in Fig. 4(d) [Fig. 4(f)]. It is placed in Fig. 4(c) [Fig. 4(e)] at the intersection between $(\mathbf{BC})$ and the vertical line $\langle f_{\mathrm{gv}} \rangle_{\mathrm{km}} = 0$. The slope of $(\mathbf{BC})$ is computed as the slope of the linear regression of the data points corresponding to the "wet surface" edge of the triangle $T_{\mathrm{km}} - \langle f_{\mathrm{gv}} \rangle_{\mathrm{km}}$. The off-set of $(\mathbf{BC})$ is determined from $\mathbf{C}$.
3) Vertex $\mathbf{A}$ corresponds to dry bare soil and is located at $(0, \mathbf{T_{b,ds}})$ in Fig. 4(c) [Fig. 4(e)] and at $(\alpha_{\mathbf{bs}}, \mathbf{T_{b,ds}})$ in Fig. 4(d) [Fig. 4(f)]. It is placed in Fig. 4(c) [Fig. 4(e)] at the intersection between $(\mathbf{AC})$ and the vertical line $\langle f_{\mathrm{gv}} \rangle_{\mathrm{km}} = 0$. The slope of $(\mathbf{AC})$ is computed as the slope of the linear regression of the data points corresponding to the "dry soil" edge of the triangle $T_{\mathrm{km}} - \langle f_{\mathrm{gv}} \rangle_{\mathrm{km}}$. The off-set of $(\mathbf{AC})$ is determined from $\mathbf{C}$.
4) Vertex $\mathbf{D}$ corresponds to full-cover senescent vegetation and is located at $(\alpha_{\mathbf{fcsv}}, \mathbf{T_{fcsv}})$ in Fig. 4(d) [Fig. 4(f)]. It is placed in Fig. 4(d) [Fig. 4(f)] at the intersection between $(\mathbf{AD})$ and the vertical line $\langle \alpha \rangle_{\mathrm{km}} = \alpha_{\mathbf{fcsv}}$. The line $(\mathbf{AD})$ is considered as being parallel to $(\mathbf{BC})$[5]. Consequently, the slope of $(\mathbf{AD})$ is determined from

the slope of $(\mathbf{BC})$. The off-set of $(\mathbf{AD})$ is determined from $\mathbf{A}$. Note that the lines $(\mathbf{AD})$ and $(\mathbf{BC})$ might not be strictly parallel. This may be due to a lack of representativeness of the surface conditions captured at 250-m resolution within the study area. In that case, one or several data points may be located above $(\mathbf{AD})$. To circumvent this artifact, the slope of $(\mathbf{AD})$ in Fig. 4(d) [Fig. 4(f)] is increased so that all data points will be located below the "dry surface" edge.

Table III lists the four temperature end-members: 1) estimated from Fig. 4(a) and (b) using high-resolution ASTER data; 2) extrapolated from Fig. 4(c) and (d) using aggregated ASTER temperature data; and 3) extrapolated from Fig. 4(e) and (f) using MODIS temperature data. The values extrapolated from aggregated ASTER and MODIS temperatures are rather close to those estimated from high-resolution ASTER temperature data, with the maximum difference in extrapolated temperatures being 2.6 °C, except for $\mathbf{T_{fcsv}}$ using MODIS data. In the latter case, the significant underestimation (5.3 °C) of $\mathbf{T_{fcsv}}$ can be explained by the following: 1) the negative mean difference $(-2.3\ ^\circ\mathrm{C})$ between MODIS and ASTER data and/or 2) the smaller range of (spatial dynamics) of 1-km resolution MODIS data in relation to 1-km aggregated ASTER data [please compare Fig. 4(c) with Fig. 4(e), and Fig. 4(d) with Fig. 4(f)].

D. Brightness Temperature

To estimate soil evaporative efficiency β in (20) and β' in (22), five brightness temperature values corresponding to extreme surface conditions are required: $\mathbf{TB_{b,ds}}$, $\mathbf{TB_{b,ws}}$, $\mathbf{TB_{fcgv,ws}}$, $\mathbf{TB_{fcgv,ds}}$, and $\mathbf{TB_{fcsv,ds}}$. In this paper, those five values are estimated from a generalized version [5], [9] of the classical "triangle method" [27].

Fig. 5(a) shows the space defined by PLMR brightness temperature and ASTER land surface temperature. In the following, an original interpretation of the five vertices visible in Fig. 5(a) is provided, which is consistent with both the classical "triangle method" and the state-of-the-art L-band radiative transfer models. Vertices are presented successively in the counterclockwise direction, and the correspondence with vegetation and soil conditions is summarized in Table I.

1) Vertex at minimum brightness temperature: L-band radiative transfer models predict an increase of brightness temperature with biomass and a decrease of brightness temperature with surface soil moisture (e.g., [48] and [49]). Therefore, the point at minimum brightness temperature corresponds to wet bare soil. This vertex is noted as $\mathbf{B}$ in Fig. 5(a), which is consistent with Fig. 4.
2) Vertex at maximum land surface temperature: the triangle method predicts a decrease of land surface temperature with both vegetation cover and surface soil moisture. Therefore, the point at maximum land surface temperature corresponds to dry bare soil. This vertex is noted as $\mathbf{A}$ in Fig. 5(a), which is consistent with Fig. 4.
3) Vertex at maximum brightness temperature: being consistent with an increase of vegetation emission with biomass and a decrease of soil emission with surface soil moisture, the point at maximum brightness temperature corresponds to full-cover vegetation with dry soil. It could correspond to full-cover green vegetation. However, the associated land surface temperature in Fig. 5(a) is much larger than that over full-cover green vegetation (21 °C) and rather close to the temperature over full-cover senescent vegetation (34 °C). Therefore, the point at maximum brightness temperature corresponds to full-cover senescent vegetation with dry soil. This vertex is noted as $\mathbf{D}'$ in Fig. 5(a), which is consistent with Fig. 4. A prime mark indicates that $\mathbf{D}'$ corresponds to a dry soil, whereas $\mathbf{D}$ does not specify soil hydric status. Note that $\mathbf{D}'$ does not necessarily correspond to dry senescent vegetation since wet senescent vegetation can lead to large values of brightness temperature [50]. In our case study, however, no rainfall occurred during the four days preceding the ASTER overpass, which means that senescent vegetation was completely dry. In terms of radiative transfer modeling, the effect of dry biomass on brightness temperature can be represented by large values of roughness parameter [51].
4) Vertices at minimum land surface temperature: two more vertices are apparent in the counterclockwise direction. Being consistent with a decrease of land surface temperature with green vegetation, both points correspond to full-cover green vegetation. As vegetation is partially transparent to the L-band emission from the soil, each point corresponds to a different soil hydric status. The vertex with a larger TB [noted as $\mathbf{C}''$ in Fig. 5(a)] corresponds to full-cover green vegetation with dry soil, and the point with a lower TB [noted as $\mathbf{C}'$ in Fig. 5(a)] corresponds to full-cover green vegetation with wet soil.

As high-resolution temperature is assumed to be unavailable in this paper, brightness temperature end-members are not estimated from the polygon $TB - T$ in Fig. 5(a) but from the polygon $TB - f_{\mathrm{gv}}$ shown in Fig. 5(b). The following is an interpretation of the polygon in Fig. 5(b), based on the consistency with the polygon in Fig. 5(a). In particular, the five vertices in Fig. 5(a) can be located in Fig. 5(b) as follows.

1) Vertex $\mathbf{B}$ corresponds to wet bare soil. It is located at the minimum value of brightness temperature such that $f_{\mathrm{gv}} = 0$.
2) Vertex $\mathbf{A}$ corresponds to bare dry soil. It is not apparent in Fig. 5(b) because fractional green vegetation is not sufficient information to distinguish between bare soil and senescent vegetation.
3) Vertex $\mathbf{D}'$ corresponds to full-cover senescent vegetation with dry soil. It is located at the maximum value of brightness temperature.
4) Vertex $\mathbf{C}''$ corresponds to full-cover green vegetation with dry soil. It is located at the maximum value of brightness temperature such that $f_{\mathrm{gv}} = 1$.
5) Vertex $\mathbf{C}'$ corresponds to full-cover green vegetation with wet soil. It is located at the minimum value of brightness temperature such that $f_{\mathrm{gv}} = 1$.

Based on the aforementioned interpretation of the polygon $TB - f_{\mathrm{gv}}$ in Fig. 5(b), the methodology used for estimating

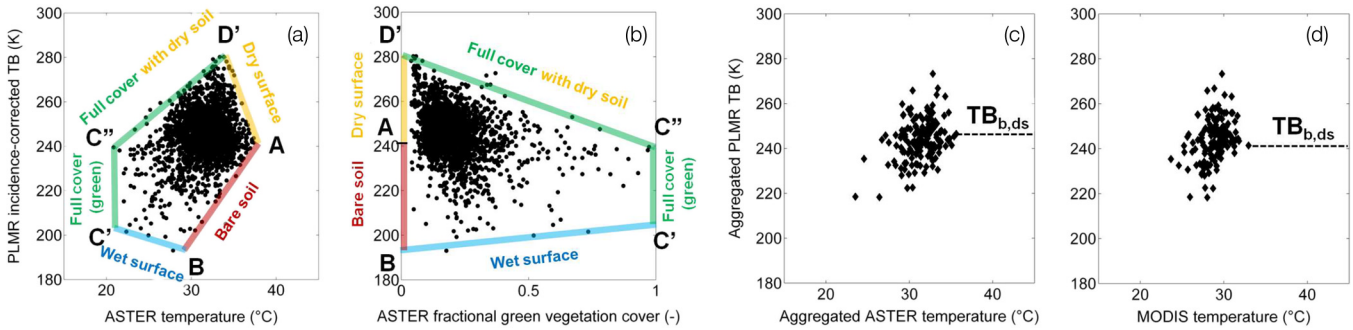

Fig. 5. (a) Scatterplot of PLMR incidence-corrected brightness temperature TB versus ASTER land surface temperature and (b) versus ASTER fractional green vegetation cover, and (c) scatterplot of aggregated TB versus aggregated ASTER temperature and (d) versus MODIS temperature. Extreme brightness temperatures $\mathbf{TB_{b,ws}}$, $\mathbf{TB_{fcgv,ws}}$, $\mathbf{TB_{fcgv,ds}}$, and $\mathbf{TB_{fcsv,ds}}$ are estimated by interpreting the bare soil, dry surface, full-cover vegetation, and wet surface edges of the polygon in (b). The estimation of $\mathbf{TB_{b,ds}}$ using low-resolution temperature data is illustrated with aggregated ASTER temperature in (c) and MODIS temperature in (d).

$\mathbf{TB_{b,ds}}$, $\mathbf{TB_{b,ws}}$, $\mathbf{TB_{fcgv,ws}}$, $\mathbf{TB_{fcgv,ds}}$, and $\mathbf{TB_{fcsv,ds}}$ is detailed in the following.

1) The brightness temperature over full-cover dry surface ($\mathbf{TB_{fcsv,ds}}$) and over wet bare soil ($\mathbf{TB_{b,ws}}$) are set to the maximum and minimum brightness temperatures observed within the study area, respectively.
2) The brightness temperatures over full-cover green vegetation with wet soil ($\mathbf{TB_{fcgv,ws}}$) and over full-cover green vegetation with dry soil ($\mathbf{TB_{fcgv,ds}}$) are estimated as the brightness temperature extrapolated at $f_{\rm gv} = 1$ in Fig. 5(b) along the "wet soil" and the "full-cover dry soil" edge, respectively. The slope of the lines ($\mathbf{BC}'$) and ($\mathbf{D}'\mathbf{C}''$) are determined so that all of the points with $f_{\rm gv} > 0.5$ be above and below the "wet soil" and "full-cover dry soil" edges, respectively.
3) Vertex $\mathbf{A}$ cannot be identified in the space $TB - f_{\rm gv}$. Consequently, $\mathbf{TB_{b,ds}}$ is set to the brightness temperature corresponding to the maximum $T_{\rm km}$ (see Fig. 5(c) for aggregated ASTER temperature and Fig. 5(d) for MODIS temperature data).

Table III lists the five brightness temperature end-members: 1) estimated from Fig. 5(a) using high-resolution ASTER data; 2) estimated from Fig. 5(b) and (c) using high-resolution fractional green vegetation cover and aggregated ASTER temperature data; and 3) estimated from Fig. 5(b) and (d) using high-resolution fractional green vegetation cover and MODIS temperature data. Values estimated from low-resolution temperature are remarkably close to those estimated from high-resolution ASTER temperature data (Table III), except for $\mathbf{TB_{b,ds}}$ with a difference of 6 K. This difference is apparently due to the lack of representativeness of kilometric aggregated brightness temperature and the method for estimating $\mathbf{TB_{b,ds}}$ at kilometric scale. Note, however, that a 6-K difference is still relatively low compared to the range (190 K–280 K) covered by brightness temperature values.

VI. Application

The disaggregation algorithms presented here are applied to the NAFE'06 data set. ASTER land surface temperature is aggregated at 1-km resolution, and kilometric temperature is used as input to D0, D1, D1′, D2, D2′, D3′, D4′, and D4″. As shown in Fig. 1, the verification strategy consists in comparing disaggregation results at 250-m resolution with ASTER land surface temperature. An application to MODIS data is also presented.

A. Application to Aggregated ASTER Data

1) End-Members Derived From High-Resolution Data: The approach is first implemented using the end-members estimated from high-resolution ASTER temperature data. This allows testing the robustness of the model in (15) and (16) independently of the methodology used for extrapolating the nine end-members $\mathbf{T_{b,ds}}$, $\mathbf{T_{b,ws}}$, $\mathbf{T_{fcgv}}$, $\mathbf{T_{fcsv}}$, $\mathbf{TB_{b,ds}}$, $\mathbf{TB_{b,ws}}$, $\mathbf{TB_{fcgv,ws}}$, $\mathbf{TB_{fcgv,ds}}$, and $\mathbf{TB_{fcsv,ds}}$.

Fig. 6 shows the output images of the eight disaggregation algorithms, which are to be compared with the reference image derived from ASTER land surface temperature. One observes that the disaggregated temperature is successively improved by including additional factors in the disaggregation, which indicates that the methodology is able to take into account several independent factors. Although the boxy artifact at 1-km resolution is successively reduced from $T^{(0)}$ to $T^{(4'')}$, it is still apparent for $T^{(4'')}$. This effect may be due to the following: 1) other factors that are not taken into account in the procedure, such as green vegetation water stress, wind speed, surface emissivity, surface albedo, etc.; 2) errors in estimated $f_{\rm gv}$, $f_{\rm sv}$, $f_{\rm ow}$, and β; and/or 3) resampling errors at 250-m resolution.

Table IV lists the RMSD, correlation coefficient, and slope between the disaggregated and ASTER temperatures for each of the eight disaggregation algorithms. The error is successively decreased from 1.65 °C to 1.16 °C, while the correlation coefficient and slope are successively increased from 0.79 and 0.63 to 0.89 and 0.88, respectively. When comparing D1, D2, D1′, and D2′, no significant differences are observed between all four algorithms in terms of root-mean-square error, correlation coefficient, and slope. Note that, in this paper, $f_{\rm tv}$ was estimated in a different way than in [5] because only one visible and near-infrared image was available and a FORMOSAT-like time series would be required to derive $f_{\rm tv}$ more accurately on a pixel-by-pixel basis. Nevertheless, this comparison suggests that D1′ seems to be equivalent to D1 and D2′ equivalent to D2, which justifies the use of the $T_{\rm mod}$ model.

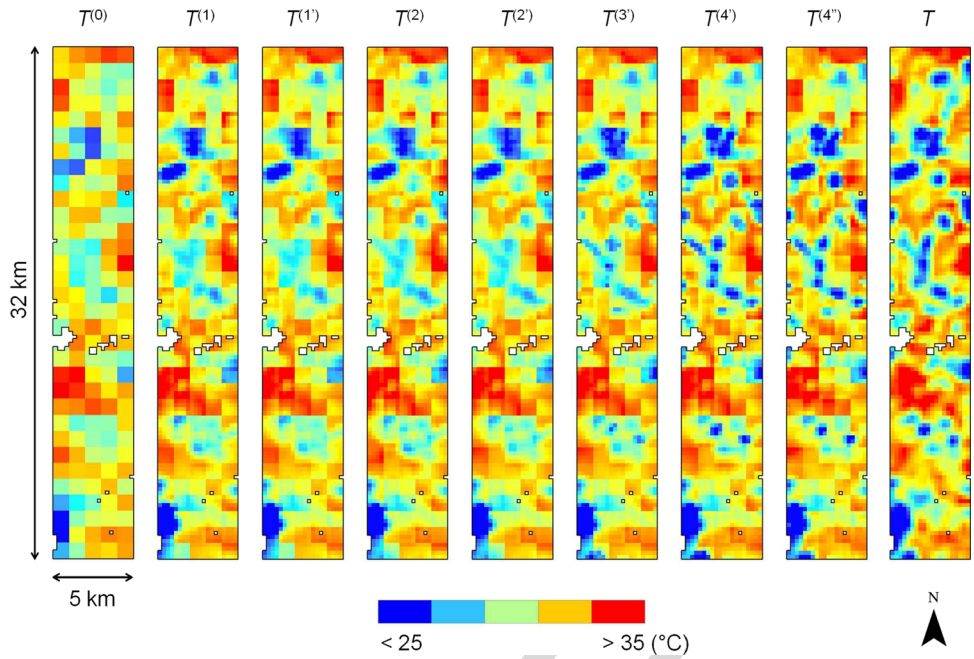

Fig. 6. Maps of the temperature disaggregated by the eight algorithms as compared with the map (right) of high-resolution ASTER temperature.

TABLE IV
RMSD, CORRELATION COEFFICIENT (R), AND SLOPE BETWEEN THE DISAGGREGATED AND ASTER TEMPERATURES. THE RESULTS CORRESPOND TO THE END-MEMBERS ESTIMATED USING HIGH-RESOLUTION ASTER TEMPERATURE DATA (TO THE END-MEMBERS EXTRAPOLATED USING AGGREGATED ASTER TEMPERATURE DATA)

Algorithm	RMSD °C	R -	Slope -
D0	1.65	0.79	0.63
D1	1.39	0.86	0.76
D2	1.35 (1.35)	0.87 (0.87)	0.76 (0.76)
D1′	1.38 (1.39)	0.86 (0.86)	0.74 (0.72)
D2′	1.30 (1.40)	0.88 (0.86)	0.75 (0.73)
D3′	1.22 (1.27)	0.89 (0.88)	0.78 (0.76)
D4′	1.15 (1.15)	0.91 (0.91)	0.86 (0.84)
D4″	1.16 (1.24)	0.89 (0.80)	0.88 (0.86)

The main advantage of the new approach is to take into account a number of additional factors, including fractional open water and soil evaporative efficiency. When comparing the results obtained for D3′, D4′, and D4″ in Table IV, it is observed that the disaggregated temperature is significantly improved against the classical approaches D1 and D2. Moreover, the statistical results are successively improved by including f_{ow}, β, and β'. Fig. 7 shows the improvement, especially in the slope between the disaggregated and ASTER temperatures. The good results obtained for D4″ indicate that the performance of disaggregation algorithms is intimately related to the following: 1) the capability of separating the independent factors that impact on surface temperature and 2) the ability to integrate them consistently into the procedure.

2) End-Members Derived From Aggregated ASTER Data: As disaggregation procedures D1′, D2′, D3′, D4′, and D4″ are subjected to uncertainties in land surface temperature and brightness temperature end-members, the five algorithms are next tested using the end-members estimated from kilometric temperature data, as presented in Section V. Aggregated ASTER (instead of MODIS) data are used to evaluate the

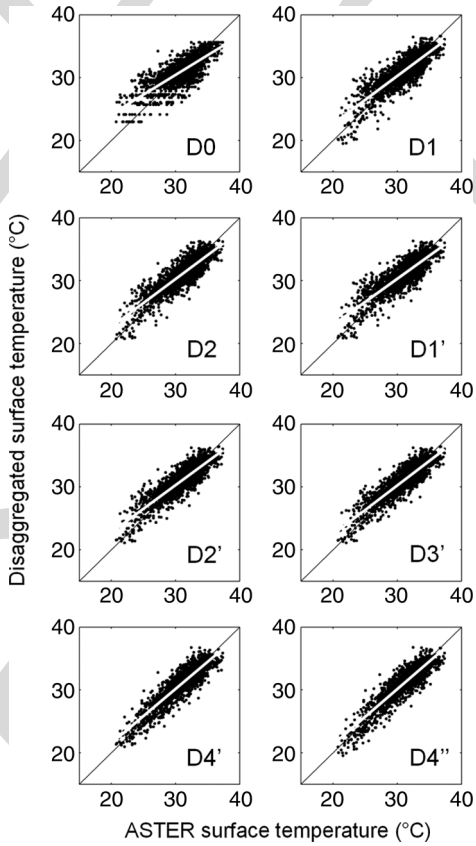

Fig. 7. Aggregated ASTER temperature (1 km) is disaggregated by each of the eight algorithms and is plotted against high-resolution ASTER temperature.

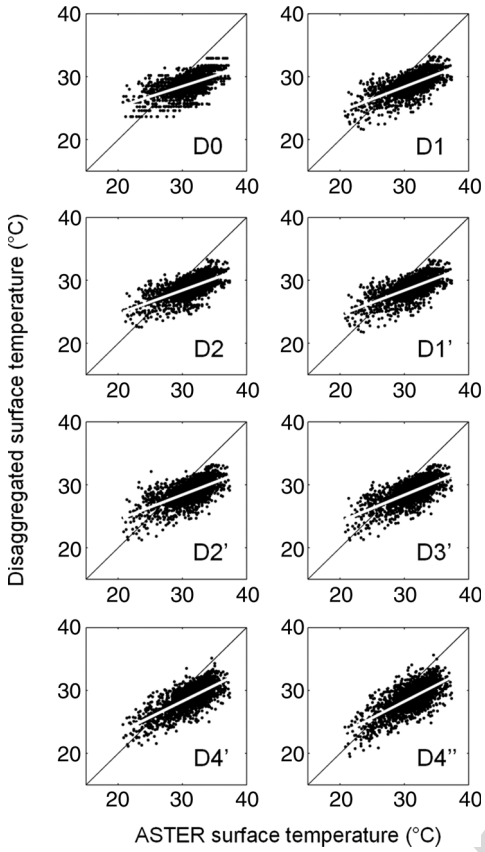

Fig. 8. MODIS temperature (1 km) is disaggregated by each of the eight algorithms and is plotted against high-resolution ASTER temperature.

impact of end-members regardless of the discrepancy between MODIS and ASTER temperatures.

Table IV lists the RMSD, correlation coefficient, and slope between the disaggregated and ASTER temperatures for each of the five algorithms. Results are compared with those obtained using the end-members estimated from high-resolution ASTER temperature. In general, the error is slightly larger, and the correlation coefficient and slope are slightly lower using extrapolated end-members. Nevertheless, the disaggregated temperature is still much improved by applying D4″ instead of D1′, with the correlation coefficient and slope increasing from 0.74 to 0.88 and from 0.72 to 0.86, respectively. Consequently, the extrapolation of end-members from kilometric data is not found to be a limiting factor in the methodology.

B. Application to MODIS Data

Disaggregation algorithms D0, D1, D1′, D2, D2′, D3′, D4′, and D4″ are then applied to MODIS data. In this case, end-members are derived from MODIS data. Fig. 8 shows the scatterplot of disaggregated MODIS versus ASTER temperature for each algorithm separately. One observes that the new methodology improves the correlation and slope of the linear regression between the disaggregated and ASTER temperatures. However, a systematic negative bias is apparent in the disaggregated temperature. Table V lists the RMSD, correlation coefficient, and slope between the disaggregated and ASTER temperatures for each of the eight algorithms. The error slightly decreases

TABLE V
RMSD, CORRELATION COEFFICIENT (R), AND SLOPE BETWEEN THE DISAGGREGATED AND ASTER TEMPERATURES. THE RESULTS CORRESPOND TO THE END-MEMBERS EXTRAPOLATED USING MODIS TEMPERATURE DATA

Algorithm	RMSD °C	R -	Slope -
D0	3.19	0.60	0.33
D1	3.08	0.67	0.39
D2	3.11	0.66	0.37
D1′	3.09	0.67	0.39
D2′	3.12	0.65	0.39
D3′	3.06	0.69	0.42
D4′	2.98	0.73	0.50
D4″	3.03	0.70	0.52

from 3.2 °C to 3.0 °C, while the correlation coefficient and slope increase from 0.6 and 0.3 to 0.7 and 0.5, respectively. The results obtained for D3′ and D4′ in Table V indicate that the disaggregated temperature is improved against the classical approaches D1 and D2. As for the application to aggregated ASTER data, the statistical results are successively improved by including f_{ow}, β, and β'. However, the improvement with MODIS data is not as visible as with aggregated ASTER data because the difference between MODIS and ASTER data (please refer to Section II-C) has the same order of magnitude as the subpixel variability at 250-m resolution (see RMSD for D0 in Table V). In particular, the mean bias and the relatively low slope of the linear regression between the disaggregated and ASTER data are associated with the discrepancy at 1-km resolution between the MODIS and ASTER temperature data.

VII. SENSITIVITY ANALYSIS

To further assess the stability of the new D′ algorithms based on radiative transfer, two sensitivity analyses are conducted by the following: 1) adding a Gaussian noise on kilometric temperatures and high-resolution brightness temperatures and 2) estimating the contribution of each factor on the variability of modeled land surface temperature.

A. Uncertainty in End-Members

To test the stability of the method for estimating the nine end-members ($\mathbf{T_{b,ds}}$, $\mathbf{T_{b,ws}}$, $\mathbf{T_{fcgv}}$, $\mathbf{T_{fcsv}}$, $\mathbf{TB_{b,ds}}$, $\mathbf{TB_{b,ws}}$, $\mathbf{TB_{fcgv,ws}}$, $\mathbf{TB_{fcgv,ds}}$, and $\mathbf{TB_{fcsv,ds}}$) from low-resolution temperature data, a Gaussian noise with a standard deviation of 1 °C is added to the kilometric (aggregated ASTER) land surface temperature data set, and a Gaussian noise with a standard deviation of 2 K is added to the high-resolution brightness temperature data set. An ensemble of 100 data sets is generated and used as input to the disaggregation algorithms.

Table VI reports the average and standard deviation of extrapolated end-members computed within the ensemble of 100 artificially perturbed data sets. Results indicate that the method for extrapolating end-members is stable for all end-members.

TABLE VI
MEAN AND STANDARD DEVIATION OF LAND SURFACE TEMPERATURE AND L-BAND BRIGHTNESS TEMPERATURE END-MEMBERS EXTRAPOLATED USING KILOMETRIC TEMPERATURE DATA. FOR THE CONVENIENCE OF THE READER, THE UNIT IS DEGREE CELSIUS FOR RADIOMETRIC TEMPERATURE AND KELVIN FOR BRIGHTNESS TEMPERATURE

End-member	Mean	St. dev.	Unit
$\mathbf{T_{b,ds}}$	40.8	0.8	°C
$\mathbf{T_{b,ws}}$	25.7	1.5	°C
$\mathbf{T_{fcgv}}$	21.0	0	°C
$\mathbf{T_{fcsv}}$	33.1	1.3	°C
$\mathbf{TB_{b,ds}}$	246	3.2	K
$\mathbf{TB_{b,ws}}$	193	1.4	K
$\mathbf{TB_{fcgv,ws}}$	204	2.3	K
$\mathbf{TB_{fcgv,ds}}$	240	1.5	K
$\mathbf{TB_{fcsv,ds}}$	281	1.0	K

TABLE VII
RMSD, CORRELATION COEFFICIENT (R), AND SLOPE BETWEEN THE DISAGGREGATED AND ASTER TEMPERATURES FOR THE DATA INCLUDING ALL THE 100 ARTIFICIALLY NOISED DATA SETS

Algorithm	RMSD °C	R -	Slope -
D0	1.81	0.75	0.63
D1	1.58	0.82	0.76
D2	1.54	0.83	0.76
D1′	1.57	0.82	0.73
D2′	1.54	0.83	0.74
D3′	1.44	0.85	0.78
D4′	1.39	0.87	0.87
D4″	1.48	0.86	0.89

Table VII lists the RMSD, correlation coefficient, and slope between the disaggregated and ASTER temperatures for all 100 data sets. Although the results are generally degraded by using noisy input data sets, D4″ is still superior to all other algorithms (see Fig. 9). Therefore, the integration of fractional open water and soil evaporative efficiency into the disaggregation is able to improve the representation of land surface temperature variability despite the uncertainties in $f_{\rm ow}$ and β', and the uncertainties in extrapolated end-members.

B. Weighting Variability Factors

Results with the NAFE'06 data set have indicated that the new D′ algorithms based on radiative transfer significantly improve (in relation to D1 and D2 methods) the representation of disaggregated temperature by directly integrating the various input parameters of the radiative transfer equation. Another advantage of the proposed methodology is to quantify the weight of these input parameters. Here, the relative weights of $f_{\rm gv}$, $f_{\rm sv}$, $f_{\rm ow}$, and β' are compared, and the relative improvement in disaggregated temperature when including these factors in the disaggregation is assessed. The weight of $f_{\rm gv}$ on the variability

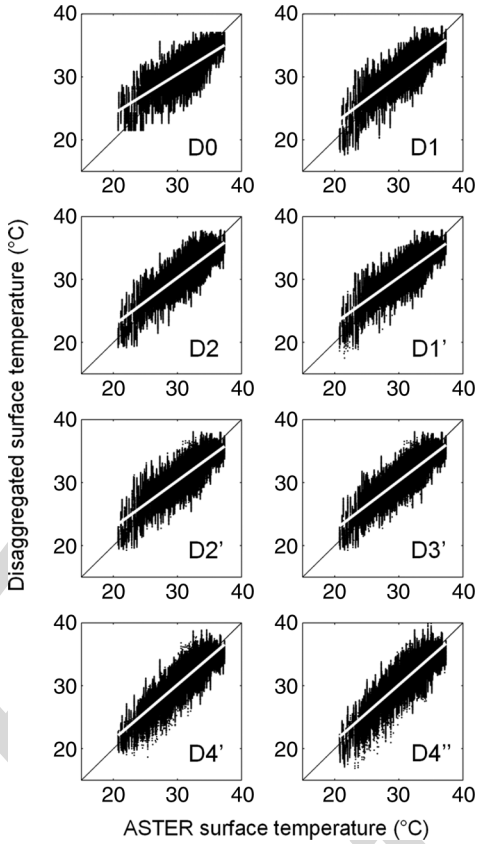

Fig. 9. As for Fig. 7 but using all the 100 artificially noised input data sets.

in land surface temperature is derived by computing the first partial derivative of $T_{\rm mod}$ from (15) and (16)

$$\frac{\partial T_{\rm mod}}{\partial f_{\rm gv}} = -(1-f_{\rm ow})(\mathbf{T_{fcsv}} - \mathbf{T_{fcgv}}). \quad (25)$$

Similarly, the first partial derivative of $T_{\rm mod}$ is computed with respect to $f_{\rm sv}$

$$\frac{\partial T_{\rm mod}}{\partial f_{\rm sv}} = -(1-f_{\rm ow})\left[\beta'\mathbf{T_{b,ws}} + (1-\beta')\mathbf{T_{b,ds}} - \mathbf{T_{fcsv}}\right] \quad (26)$$

with respect to $f_{\rm ow}$

$$\frac{\partial T_{\rm mod}}{\partial f_{\rm ow}} = -\left[f_{\rm gv}\mathbf{T_{fcgv}} + (f_{\rm tv}-f_{\rm gv})\mathbf{T_{fcsv}} + (1-f_{\rm tv})\left(\beta'\mathbf{T_{b,ws}} + (1-\beta')\mathbf{T_{b,ds}}\right) - \mathbf{T_{fcgv}}\right] \quad (27)$$

and with respect to β'

$$\frac{\partial T_{\rm mod}}{\partial \beta'} = -(1-f_{\rm ow})(1-f_{\rm tv})(\mathbf{T_{b,ds}} - \mathbf{T_{b,ws}}). \quad (28)$$

Table VIII lists the standard deviation of each parameter within the study area, the average of partial derivatives, and the relative weight of each parameter on the variability of modeled land surface temperature. The relative weights of $f_{\rm gv}$, $f_{\rm sv}$, $f_{\rm ow}$, and β' are estimated as the mean partial derivative times the standard deviation. Results indicate that all parameters have a negative impact on T. More interestingly, $f_{\rm gv}$ appears to be the most significant variability factor, with a relative weight of 42%, which is consistent with NDVI-based approaches [4].

TABLE VIII
STANDARD DEVIATION, MEAN PARTIAL DERIVATIVE, AND IMPACT ON HIGH-RESOLUTION MODELED TEMPERATURE OF EACH OF THE FOUR PARAMETERS: FRACTIONAL GREEN VEGETATION COVER, FRACTIONAL SENESCENT VEGETATION COVER, FRACTIONAL OPEN WATER, AND SOIL EVAPORATIVE EFFICIENCY

Factor	Standard deviation	Mean partial derivative	Impact on T_{mod} (percentage of total)
-	-	°C	°C (%)
f_{gv}	0.11	−13	0.97 (42)
f_{sv}	0.19	−2.0	0.26 (11)
f_{ow}	0.06	−11	0.45 (20)
β'	0.19	−4.8	0.17 (27)

The second and third most significant variability factors are soil evaporative efficiency and fractional open water, with relative weights of 27% and 20%, respectively. Finally, fractional senescent vegetation cover represents only 11% of the variability in land surface temperature. The low impact of f_{sv} can be associated with the low mean partial derivative. In particular, $\partial T_{\mathrm{mod}}/\partial f_{\mathrm{sv}}$ is low because the temperature difference between dry bare soil ($\mathbf{T_{b,ds}}$) and full-cover senescent vegetation ($\mathbf{T_{fcsv}}$) is also low in our case study.

The relative weights in Table VIII are now related with the disaggregation results in Table III. Consequently, the poor improvement of D2 against D1 (and D2′ against D1′) can be attributed to the relatively low weight of f_{sv} in the variability of land surface temperature. Conversely, the significant improvements of D4″ against D3′, D3′ against D2′, and D1 (and D1′) against D0 are attributed to the large weights of β', f_{ow}, and f_{gv}, respectively.

In summary, the variability of land surface temperature is reasonably represented by model T_{mod}. Moreover, the approach allows the relative weight of each variability factor to be taken into account in the disaggregation procedure.

VIII. SUMMARY AND CONCLUSION

A new disaggregation methodology for land surface temperature has been developed to integrate the main surface parameters involved in the surface energy budget. It is based on a linearized radiative transfer equation, which distinguishes between soil, vegetation, and water temperature, and uses soil evaporative efficiency and fractional senescent vegetation cover to parameterize/estimate soil and vegetation hydric status, respectively. The approach is implemented using four parameters: the fraction of green vegetation cover derived from red and near-infrared bands, the fraction of senescent vegetation cover derived from red and near-infrared bands, the fraction of open water derived from shortwave-infrared band, and the soil evaporative efficiency derived from microwave-L band. It is tested over a 5 km by 32 km area of irrigated land in Australia, including flooded rice crops, using ASTER and L-band airborne data. Low-resolution land surface temperature is simulated by aggregating ASTER land surface temperature at 1-km resolution, and the disaggregated temperature is compared to high-resolution ASTER temperature. The results indicate that the methodology is able to separate efficiently the independent factors that impact surface temperature and to integrate them consistently into the disaggregation procedure. The error in disaggregated temperature is successively reduced from 1.65 °C to 1.16 °C by including each of the four parameters. The correlation coefficient and slope between the disaggregated and ASTER temperatures are improved from 0.79 to 0.89 and from 0.63 to 0.88, respectively. Moreover, the radiative transfer equation allows quantifying the impact at high resolution of each parameter on land surface temperature. In this case study, fractional green vegetation cover is responsible for 42% of the variability in disaggregated land surface temperature, fractional senescent vegetation cover for 11%, fractional open water for 20%, and soil evaporative efficiency for 27%.

Note that the approach presented in this paper did not take into account the water stress of green vegetation because none of the considered parameters (fractional green vegetation cover, fractional senescent vegetation cover, fractional open water, and soil evaporative efficiency) could describe the hydric status of photosynthetically active (green) vegetation. The analysis was conducted solely in a highly irrigated environment in which vegetation water stress was small. However, in most cases, the vegetation water stress might not be negligible for natural areas. In the presence of water-stressed green vegetation, the scatterplot (temperature versus green vegetation cover) would be transformed into a trapezoidal shape with four vertices rather than a triangle. In such conditions, the disaggregation problem would be partly undetermined since the partitioning between unstressed and stressed green vegetations would not be represented. Consequently, the approaches shown here are not expected to be representative of other less extreme environments than the present irrigated area. Nevertheless, one should keep in mind that improving the spatial resolution of land surface temperature data via disaggregation is only relevant in the conditions where the spatial variability of temperature is large.

Although the approach was successfully applied to airborne and satellite data collected during NAFE'06, further research is needed to test the disaggregation approach on a routine basis. One may anticipate that fractional green and senescent vegetation covers could be derived accurately using FORMOSAT-like data. The FORMOSAT-2 instrument [52] provides shortwave data at high spatial resolution (8 m) and high temporal frequency (potentially one image per day), which allow a fine analysis of the seasonality of canopies during the crop cycle [5], [53], [54]. Fractional open water could be derived from Landsat-5 data (e.g., [20]). Although the repeat cycle of Landsat (16 days) is longer than the temporal resolution needed for land surface temperature, the seasonal variations of water bodies

such as irrigation canals and flooded fields are expected to be low. Soil evaporative efficiency could be derived at high resolution from active microwave sensors, such as the Phased Array L-band SAR (PALSAR) [55]. Soil evaporative efficiency formulas express evaporation as a function of normalized surface soil moisture. Therefore, soil evaporative efficiency is equivalent to a soil moisture index, which could be replaced in (20) by the radar-derived soil wetness index computed as the observed to minimal backscattering coefficient difference divided by the maximal to minimal backscattering coefficient difference [56], [57]. Note, however, that the temporal coverage of the PALSAR fine beam dual polarization mode is relatively low, with a revisit cycle of 46 days. Consequently, accurate disaggregation of land surface temperature would still rely on the availability of high-resolution radar data.

ACKNOWLEDGMENT

The authors would like to thank the NAFE'06 participants for their participation in collecting this extensive data set.

REFERENCES

[1] S. Stisen, I. Sandholt, A. Nørgaard, R. Fensholt, and K. H. Jensen, "Combining the triangle method with thermal inertia to estimate regional evapotranspiration—Applied to MSG-SEVERI data in the Senegal River basin," *Remote Sens. Environ.*, vol. 112, no. 3, pp. 1242–1255, Mar. 2008.

[2] R. Tang, Z.-L. Li, and B. Tang, "An application of the Ts-VI method with enhanced edges determination for evapotranspiration estimation from MODIS data in arid and semi-arid regions: Implementation and validation," *Remote Sens. Environ.*, vol. 114, no. 3, pp. 540–551, Mar. 2010. doi:DOI:10.1016/j.rse.2009.10.012.

[3] B. Seguin, F. Becker, T. Phulpin, X. F. Gu, G. Guyot, Y. Kerr, C. King, J. P. Lagouarde, C. Ottlé, M. P. Stoll, A. Tabbagh, and A. Vidal, "IRSUTE: A minisatellite project for land surface heat flux estimation from field to regional scale," *Remote Sens. Environ.*, vol. 68, no. 3, pp. 357–369, Jun. 1999.

[4] N. Agam, W. P. Kustas, M. C. Anderson, F. Li, and C. M. U. Neale, "A vegetation index based technique for spatial sharpening of thermal imagery," *Remote Sens. Environ.*, vol. 107, no. 4, pp. 545–558, Apr. 2007.

[5] O. Merlin, B. Duchemin, O. Hagolle, F. Jacob, B. Coudert, G. Chehbouni, G. Dedieu, J. Garatuza, and Y. Kerr, "Disaggregation of MODIS surface temperature over an agricultural area using a time series of FORMOSAT-2 images," *Remote Sens. Environ.*, vol. 114, no. 11, pp. 2500–2512, Nov. 2010. doi:DOI:10.1016/j.rse.2010.05.025.

[6] S. B. Idso, R. D. Jackson, P. J. Pinter, R. J. Reginato, and J. L. Hatfield, "Normalizing the stress–degree–day parameter for environmental variability," *Agric. Meteorol.*, vol. 24, no. 1, pp. 45–55, 1981.

[7] R. D. Jackson, S. B. Idso, R. J. Reginato, and P. J. Pinter, "Canopy temperature as a crop water stress indicator," *Water Resour. Res.*, vol. 17, no. 4, pp. 1133–1138, 1981.

[8] M. S. Moran, T. R. Clarke, Y. Inoue, and A. Vidal, "Estimating crop water deficit using the relation between surface-air temperature and spectral vegetation index," *Remote Sens. Environ.*, vol. 49, no. 3, pp. 246–263, Sep. 1994.

[9] O. Merlin, J. P. Walker, J. D. Kalma, E. J. Kim, J. Hacker, R. Panciera, R. Young, G. Summerell, J. Hornbuckle, M. Hafeez, and T. J. Jackson, "The NAFE'06 data set: Towards soil moisture retrieval at intermediate resolution," *Adv. Water Resour.*, vol. 31, no. 11, pp. 1444–1455, Nov. 2008. doi:DOI:10.1016/j.advwatres.2008.01.018.

[10] R. Panciera, J. P. Walker, J. D. Kalma, E. J. Kim, J. Hacker, O. Merlin, M. Berger, and N. Skou, "The NAFE'05/CoSMOS data set: Toward SMOS calibration, downscaling and assimilation," *IEEE Trans. Geosci. Remote Sens.*, vol. 46, no. 3, pp. 736–745, Mar. 2008. doi:DOI:10.1109/TGRS.2007.915403.

[11] T. Schmugge, T. J. Jackson, W. P. Kustas, R. Roberts, R. Parry, D. C. Goodrich, S. A. Amer, and M. A. Weltz, "Push broom microwave radiometer observations of surface soil moisture in Monsoon '90," *Water Resour. Res.*, vol. 30, no. 5, pp. 1321–1328, 1994.

[12] M. Abrams, "The Advanced Spaceborne Thermal Emission and Reflection radiometer (ASTER): Data products for the high spatial resolution imager on NASA's Terra platform," *Int. J. Remote Sens.*, vol. 21, pp. 847–859, 2000.

[13] K. Thome, K. Arai, S. Hook, H. Kieer, H. Lang, T. Matsunaga, A. Ono, F. Palluconi, H. Sakuma, P. Slater, T. Takashima, H. Tonooka, S. Tsuchida, R. M. Welch, and E. Zalewski, "ASTER preflight and inflight calibration and the validation of level 2 products," *IEEE Trans. Geosci. Remote Sens.*, vol. 36, no. 4, pp. 1161–1172, Jul. 1998.

[14] F. Jacob, F. Petitcolin, T. Schmugge, E. Vermote, A. French, and K. Ogawa, "Comparison of land surface emissivity and radiometric temperature derived from MODIS and ASTER sensors," *Remote Sens. Environ.*, vol. 90, no. 2, pp. 137–152, Mar. 2004.

[15] J. A. Sobrino, J. C. Jiménez-Muñoz, L. Balick, A. R. Gillespie, D. A. Sabol, and W. T. Gustafson, "Accuracy of ASTER level-2 thermal-infrared standard products of an agricultural area in Spain," *Remote Sens. Environ.*, vol. 106, no. 2, pp. 146–153, Jan. 2007. doi:DOI:10.1016/j.rse.2006.08.010.

[16] C. Coll, V. Caselles, E. Valor, R. Niclòs, J. M. Sánchez, J. M. Galve, and M. Mira, "Temperature and emissivity separation from ASTER data for low spectral contrast surfaces," *Remote Sens. Environ.*, vol. 110, no. 2, pp. 162–175, Sep. 2007. doi:DOI:10.1016/j.rse.2007.02.008.

[17] A. French, T. Schmugge, J. Ritchie, A. Hsu, F. Jacob, and K. Ogawa, "Detecting land cover change at the Jornada Experimental Range, New Mexico with ASTER emissivities," *Remote Sens. Environ.*, vol. 112, no. 4, pp. 1730–1748, Apr. 2008. doi:DOI:10.1016/j.rse.2007.08.020.

[18] F. Jacob, T. Schmugge, A. Olioso, D. Courault, A. French, K. Ogawa, F. Petitcolin, G. Chehbouni, A. Pinheiro, and J. Privette, *Modeling and Inversion in Thermal Infrared Remote Sensing Over Vegetated Land Surfaces. Advances in Land Remote Sensing*, vol. 10, S. Liang, Ed. New York: Springer-Verlag, 2008.

[19] D. E. Sabol, A. R. Gillespie, E. Abbott, and G. Yamada, "Field validation of the ASTER temperature–emissivity separation algorithm," *Remote Sens. Environ.*, vol. 113, no. 11, pp. 2328–2344, Nov. 2009. doi:DOI:10.1016/j.rse.2009.06.008.

[20] T. G. Van Niel, T. R. McVicar, H. Fang, and S. Liang, "Calculating environmental moisture for per-field discrimination of rice crops," *Int. J. Remote Sens.*, vol. 24, no. 4, pp. 885–890, 2003.

[21] Y. Liu, T. Hiyama, and Y. Yamaguchi, "Scaling of land surface temperature using satellite data: A case examination on ASTER and MODIS products over a heterogeneous terrain area," *Remote Sens. Environ.*, vol. 105, no. 2, pp. 115–128, Nov. 2006.

[22] Z. Wan and J. Dozier, "A generalized split-window algorithm for retrieving land-surface temperature from space," *IEEE Trans. Geosci. Remote Sens.*, vol. 34, no. 4, pp. 892–905, Jul. 1996.

[23] G. C. Hulley and S. J. Hook, "Generating consistent land surface temperature and emissivity products between ASTER and MODIS data for Earth science research," *IEEE Trans. Geosci. Remote Sens.*, vol. 49, no. 9, pp. 1304–1315, Apr. 2011. doi:DOI:10.1109/TGRS.2010.2063034.

[24] M. Atitar and J. A. Sobrino, "A split-window algorithm for estimating LST from Meteosat 9 data: Test and comparison with *in situ* data and MODIS LSTs," *IEEE Geosci. Remote Sens. Lett.*, vol. 6, no. 1, pp. 122–126, Jan. 2009. doi:DOI:10.1109/LGRS.2008.2006410.

[25] Y. Liu, Y. Yamaguchi, and C. Ke, "Reducing the discrepancy between ASTER and MODIS land surface temperature products," *Sensors*, vol. 7, pp. 3043–3057, 2007.

[26] O. Merlin, G. Chehbouni, Y. Kerr, E. G. Njoku, and D. Entekhabi, "A combined modeling and multi-spectral/multi-resolution remote sensing approach for disaggregation of surface soil moisture: Application to SMOS configuration," *IEEE Trans. Geosci. Remote Sens.*, vol. 43, no. 9, pp. 2036–2050, Sep. 2005.

[27] T. Carlson, "An overview of the 'triangle method' for estimating surface evapotranspiration and soil moisture from satellite imagery," *Sensors*, vol. 7, pp. 1612–1629, 2007.

[28] M. C. Anderson, J. M. Norman, G. R. Diak, W. P. Kustas, and J. R. Mecikalski, "A two-source time-integrated model for estimating surface fluxes using thermal infrared remote sensing," *Remote Sens. Environ.*, vol. 60, no. 2, pp. 195–216, May 1997.

[29] O. Merlin and G. Chehbouni, "Different approaches in estimating heat flux using dual angle observations of radiative surface temperature," *Int. J. Remote Sens.*, vol. 25, no. 1, pp. 275–289, 2004.

[30] K. Nishida, R. R. Nemani, J. M. Glassy, and S. W. Running, "Development of an evapotranspiration index from Aqua/MODIS for monitoring surface moisture status," *IEEE Trans. Geosci. Remote Sens.*, vol. 41, no. 2, pp. 493–501, Feb. 2003.

[31] G. Gutman and A. Ignatov, "The derivation of the green vegetation fraction from NOAA/AVHRR data for use in numerical weather

prediction models," *Int. J. Remote Sens.*, vol. 19, no. 8, pp. 1533–1543, 1998.
[32] J. Noilhan and S. Planton, "A simple parameterization of land surface processes for meteorological models," *Monthly Weather Rev.*, vol. 117, no. 3, pp. 536–549, 1989.
[33] D. A. Roberts, M. O. Smith, and J. B. Adams, "Green vegetation, nonphotosynthetic vegetation, and soils in AVIRIS data," *Remote Sens. Environ.*, vol. 44, no. 2/3, pp. 255–269, May 1993.
[34] M. Weiss, F. Baret, M. Leroy, A. Begué, O. Hautecoeur, and R. Santer, "Hemispherical reflectance and albedo estimates from the accumulation of across track sun synchronous satellite data," *J. Geophys. Res.*, vol. 104, no. D18, pp. 221–232, 1999.
[35] F. Jacob, A. Olioso, M. Weiss, F. Baret, and O. Hautecoeur, "Mapping short-wave albedo of agricultural surfaces using airborne PolDER data," *Remote Sens. Environ.*, vol. 80, no. 1, pp. 36–46, Apr. 2002.
[36] F. Jacob, M. Weiss, A. Olioso, and A. French, "Assessing the narrowband to broadband conversion to estimate visible, near infrared and shortwave apparent albedo from airborne PolDER data," *Agronomie*, vol. 22, no. 6, pp. 537–546, Sep./Oct. 2002.
[37] F. Jacob and A. Olioso, "Derivation of diurnal courses of albedo and reflected solar irradiance from airborne PolDER data acquired near solar noon," *J. Geophys. Res.*, vol. 110, no. D10, p. D10 104, May 2005.
[38] A. Bsaibes, D. Courault, F. Baret, M. Weiss, A. Olioso, F. Jacob, O. Hagolle, O. Marloie, N. Bertrand, V. Desfond, and F. Kzemipour, "Albedo and LAI estimates from FORMOSAT-2 data for crop monitoring," *Remote Sens. Environ.*, vol. 113, no. 4, pp. 716–729, Apr. 2009. doi:DOI:10.1016/j.rse.2008.11.014.
[39] P. M. Barbosa, M. A. Casterad, and J. Herrero, "Performance of several Landsat 5 Thematic Mapper (TM) image classification methods for crop extent estimates in an irrigation district," *Int. J. Remote Sens.*, vol. 17, no. 18, pp. 3665–3674, Dec. 1996.
[40] H. Xu, "Modification of normalized difference water index (NDWI) to enhance open water features in remotely sensed imagery," *Int. J. Remote Sens.*, vol. 27, no. 14, pp. 3025–3033, Jul. 2006.
[41] W. P. Kustas, T. J. Schmugge, K. S. Humes, T. J. Jackson, R. Parry, M. A. Weltz, and M. S. Moran, "Relationships between evaporative fraction and remotely sensed vegetation index and microwave brightness temperature for semiarid rangelands," *J. Appl. Meteor.*, vol. 32, no. 12, pp. 1781–1790, Dec. 1993.
[42] J. W. Deardorff, "Efficient prediction of ground temperature and moisture with inclusion of a layer of vegetation," *J. Geophys. Res.*, vol. 83, no. C4, pp. 1889–1903, Apr. 1978.
[43] P. J. Camillo and R. J. Gurney, "A resistance parameter for bare soil evaporation models," *Soil Sci.*, vol. 141, no. 2, pp. 95–105, Feb. 1986.
[44] F. T. Ulaby, R. K. Moore, and A. K. Fung, *Microwave Remote Sensing: Active and Passive*, vol. 2. Norwood, MA: Artech House, 1982.
[45] T. J. Schmugge, "Applications of passive microwave observations of surface soil moisture," *J. Hydrol.*, vol. 212/213, pp. 188–197, Dec. 1998.
[46] M. C. Anderson, J. M. Norman, W. P. Kustas, R. Houborg, P. J. Starks, and N. Agam, "A thermal-based remote sensing technique for routine mapping of land-surface carbon, water and energy fluxes from field to regional scales," *Remote Sens. Environ.*, vol. 112, no. 12, pp. 4227–4241, Dec. 2008. doi:DOI:10.1016/j.rse.2008.07.009.
[47] L. M. Montandon and E. E. Small, "The impact of soil reflectance on the quantification of the green vegetation fraction from NDVI," *Remote Sens. Environ.*, vol. 112, no. 4, pp. 1835–1845, Apr. 2008. doi:DOI:10.1016/j.rse.2007.09.007.
[48] E. G. Njoku and D. Entekhabi, "Passive microwave remote sensing of soil moisture," *J. Hydrol.*, vol. 184, no. 1/2, pp. 101–129, Oct. 1996.
[49] J.-P. Wigneron, Y. Kerr, P. Waldteufel, K. Saleh, M.-J. Escorihuela, P. Richaume, P. Ferrazzoli, P. de Rosnay, R. Gurneye, J.-C. Calvet, J. P. Grant, M. Guglielmettih, B. Hornbuckle, C. Matzler, T. Pellarin, and M. Schwank, "L-band Microwave Emission of the Biosphere (L-MEB) model: Description and calibration against experimental data sets over crop fields," *Remote Sens. Environ.*, vol. 107, no. 4, pp. 639–655, Apr. 2007. doi:DOI:10.1016/j.rse.2008.10.014.
[50] K. Saleh, J.-P. Wigneron, P. de Rosnay, J.-C. Calvet, M. J. Escorihuela, Y. Kerr, and P. Waldteufel, "Impact of rain interception by vegetation and mulch on the L-band emission of natural grass," *Remote Sens. Environ.*, vol. 101, no. 1, pp. 127–139, Mar. 2006.
[51] K. Saleh, J.-P. Wigneron, P. Waldteufel, P. deRosnay, M. Schwank, J.-C. Calvet, and Y. H. Kerr, "Estimates of surface soil moisture under grass covers using L-band radiometry," *Remote Sens. Environ.*, vol. 109, no. 1, pp. 42–53, Jul. 2007.
[52] J.-S. Chern, J. Ling, and S.-L. Weng, "Taiwan's second remote sensing satellite," *Acta Astronaut.*, vol. 63, no. 11/12, pp. 1305–1311, Dec. 2008. doi:DOI:10.1016/j.actaastro.2008.05.022.
[53] B. Duchemin, O. Hagolle, B. Mougenot, I. Benhadj, R. Hadria, V. Simonneaux, J. Ezzahar, J. Hoedjes, S. Khabba, M. H. Kharrou, G. Boulet, G. Dedieu, S. Er-Raki, R. Escadafal, A. Olioso, and A. G. Chehbouni, "Agrometeorological study of semi-arid areas: An experiment for analysing the potential of time series of FORMOSAT-2 images (Tensift-Marrakech plain)," *Int. J. Remote Sens.*, vol. 29, no. 17, pp. 5291–5299, 2008. doi:DOI:10.1080/01431160802036482.
[54] R. Hadria, B. Duchemin, L. Jarlan, G. Dedieu, F. Baup, S. Khabba, A. Olioso, and T. Le Toan, "Potentiality of optical and radar satellite data at high spatio-temporal resolutions for the monitoring of irrigated wheat crops in Morocco," *Int. J. Appl. Earth Obs. Geoinf.*, vol. 12, pp. S32–S37, Feb. 2010. doi:DOI:10.1016/j.jag.2009.09.003.
[55] A. Rosenqvist, M. Shimada, N. Ito, and M. Watanabe, "ALOS PALSAR: A pathfinder mission for global-scale monitoring of the environment," *IEEE Trans. Geosci. Remote Sens.*, vol. 45, no. 11, pp. 3307–3316, Nov. 2007.
[56] W. Wagner, G. Lemoine, M. Borgeaud, and H. Rott, "A study of vegetation cover effects on ERS scatterometer data," *IEEE Trans. Geosci. Remote Sens.*, vol. 37, no. 2, pp. 938–948, Mar. 1999.
[57] R. Fieuzal, B. Duchemin, L. Jarlan, M. Zribi, F. Baup, O. Merlin, O. Hagolle, and J. Garatuza-Payan, "Combined use of optical and radar satellite data for the monitoring of irrigation and soil moisture of wheat crops," *Hydrol. Earth Syst. Sci.*, vol. 15, no. 4, pp. 1117–1129, 2011. doi:DOI:10.5194/hess-15-117-2011.

Olivier Merlin, photograph and biography not available at the time of publication. **AQ4**

Frédéric Jacob, photograph and biography not available at the time of publication.

Jean-Pierre Wigneron, photograph and biography not available at the time of publication.

Jeffrey Walker, photograph and biography not available at the time of publication.

Ghani Chehbouni, photograph and biography not available at the time of publication.

AUTHOR QUERIES

AUTHOR PLEASE ANSWER ALL QUERIES

Please be aware that the authors are required to pay overlength page charges ($200 per page) if the paper is longer than 6 pages. If you cannot pay any or all of these charges please let us know.

AQ1 = Please provide the current affiliation (name and specific address of the company) of authors "Frederic Jacob," "Jean-Pierre Wigneron," "Jeffrey Walker," and "Ghani Chehbouni."
AQ2 = The sentence that starts with "It is a three-step procedure..." was modified to properly introduce the list. Please check if the thought is preserved, and correct if necessary.
AQ3 = The caption for Table III was modified. Please check if the thought is preserved, and correct if necessary.
AQ4 = Please provide photo and biography of all authors.

END OF ALL QUERIES

Multidimensional Disaggregation of Land Surface Temperature Using High-Resolution Red, Near-Infrared, Shortwave-Infrared, and Microwave-L Bands

Olivier Merlin, Frédéric Jacob, Jean-Pierre Wigneron, Jeffrey Walker, and Ghani Chehbouni

***Abstract*—Land surface temperature data are rarely available at high temporal and spatial resolutions at the same locations. To fill this gap, the low spatial resolution data can be disaggregated at high temporal frequency using empirical relationships between remotely sensed temperature and fractional green (photosynthetically active) and senescent vegetation covers. In this paper, a new disaggregation methodology is developed by physically linking remotely sensed surface temperature to fractional green and senescent vegetation covers using a radiative transfer equation. Moreover, the methodology is implemented with two additional factors related to the energy budget of irrigated areas, being the fraction of open water and soil evaporative efficiency (ratio of actual to potential soil evaporation). The approach is tested over a 5 km by 32 km irrigated agricultural area in Australia using airborne Polarimetric L-band Multibeam Radiometer brightness temperature and spaceborne Advanced Scanning Thermal Emission and Reflection radiometer (ASTER) multispectral data. Fractional green vegetation cover, fractional senescent vegetation cover, fractional open water, and soil evaporative efficiency are derived from red, near-infrared, shortwave-infrared, and microwave-L band data. Low-resolution land surface temperature is simulated by aggregating ASTER land surface temperature to 1-km resolution, and the disaggregated temperature is verified against the high-resolution ASTER temperature data initially used in the aggregation process. The error in disaggregated temperature is successively reduced from 1.65 °C to 1.16 °C by including each of the four parameters. The correlation coefficient and slope between the disaggregated and ASTER temperatures are improved from 0.79 to 0.89 and from 0.63 to 0.88, respectively. Moreover, the radiative transfer equation allows quantification of the impact on disaggregation of the temperature at high resolution for each parameter: fractional green vegetation cover is responsible for 42% of the variability in disaggregated temperature, fractional senescent vegetation cover for 11%, fractional open water for 20%, and soil evaporative efficiency for 27%.**

***Index Terms*—Advanced Scanning Thermal Emission and Reflection radiometer (ASTER), brightness temperature, disaggregation, evaporative efficiency, land surface temperature, Moderate Resolution Imaging Spectroradiometer (MODIS), multispectral, open water, soil moisture, vegetation fraction.**

I. Introduction

REMOTELY sensed land surface temperature is a signature of the thermodynamic equilibrium state of the surface skin. Consequently, it provides the potential to monitor dynamic information on instantaneous energy and water fluxes at the land-surface–atmosphere interface. Nevertheless, the operational use of thermal remote sensing for hydrological and water resource management studies has been limited to regional scale applications (e.g., [1] and [2]) mainly because the spatial resolution (larger than 1 km) of current high temporal resolution thermal sensors is too coarse to represent the heterogeneity of man-made landscapes. For example, the Moderate Resolution Imaging Spectroradiometer (MODIS) has a revisit frequency of 1 or 2 times per day but a spatial resolution of only 1 km, while the Advanced Scanning Thermal Emission and Reflection radiometer (ASTER) has a spatial resolution of 90 m but a revisit time of only 16 days.

The use of remotely sensed land surface temperature over agricultural areas requires data at both high spatial and temporal resolutions [3]. While there is a lack of high spatial resolution thermal data from satellite with high frequency, there is the potential for land surface temperature derived from kilometric resolution sensors having high temporal resolution to be disaggregated using high spatial resolution ancillary data. The first disaggregation approach of remotely sensed temperature was developed by [4] using the fractional green vegetation cover derived from red and near-infrared reflectances. Given the high temperature difference between bare soil and a well-watered crop, this approach has proved to be effective over areas with relatively uniform soil and vegetation hydric status. Recently, [5] has extended the approach of [4] to conditions where vegetation hydric status is heterogeneous. This required developing a methodology to estimate the fraction of senescent vegetation cover from a time series of FORMOSAT-2 images.

Manuscript received December 2, 2010; revised June 28, 2011; accepted September 11, 2011. This work was supported in part by the French program Terre-Océan-Surfaces-Continentales-Atmosphère and in part by the Centre National de la Recherche Scientifique. The National Airborne Field Experiments have been made possible through infrastructure (LE0453434 and LE0560930) and research (DP0557543) funding from the Australian Research Council and the collaboration of a large number of scientists from throughout Australia, U.S., and Europe. Initial setup and maintenance of the study catchments were funded by a research Grant (DP0343778) from the Australian Research Council and by the CRC for Catchment Hydrology.

O. Merlin is with the Centre d'Etudes Spatiales de la Biosphère (CESBIO), 31401 Toulouse, France (e-mail: olivier.merlin@cesbio.cnes.fr).

F. Jacob (e-mail: frederic.jacob@supagro.inra.fr).

J.-P. Wigneron (e-mail: jpwigner@bordeaux.inra.fr).

J. Walker (e-mail: jeff.walker@monash.edu).

G. Chehbouni (e-mail: ghani.chehbouni@cesbio.cnes.fr).

Color versions of one or more of the figures in this paper are available online at http://ieeexplore.ieee.org.

Digital Object Identifier 10.1109/TGRS.2011.2169802

The accuracy in disaggregated temperature was improved by taking into account fractional senescent vegetation cover in addition to fractional green vegetation cover.

Fractional green and senescent vegetation covers, however, are not the only factors explaining the spatial variations of land surface temperature, especially over irrigated areas where crop fields may have different moisture status to the surrounds. In particular, the temperature over a flooded crop field may be drastically different from the temperature over a mature crop field. Therefore, the fraction of open water is an important variable to represent the spatial variations of land surface temperature. Over nonwatered land surfaces, the soil evaporative efficiency (ratio of actual to potential soil evaporation) is a signature of the capacity of the soil to evaporate its water content in the near surface and thus to counter an increase of its thermodynamic temperature. Consequently, soil evaporative efficiency is also an essential variable to describe the spatial variations of land surface temperature. Moreover, knowledge of soil evaporative efficiency is needed to decouple the effects of soil and vegetation hydric status on the surface energy budget and hence to better represent the resultant radiative surface temperature. As an example, the crop water stress index (CWSI) [6], [7] can be used to detect plant stress based on the difference between foliage and air temperature. Nevertheless, the application of the CWSI to partially vegetated areas is subjected to large uncertainties because the soil background may have a different temperature to the plants [7] depending on soil evaporative efficiency. Another example is provided by Moran *et al.* [8] who proposed the vegetation index/temperature (VIT) trapezoid to estimate a most probable range of plant stress over partially vegetated fields. It is a three-step procedure in which the following steps are performed: 1) the temperatures of the four vertices of the VIT trapezoid are estimated using an energy budget model; 2) the minimum and maximum probable vegetation temperatures are estimated from the measured composite land surface temperature, together with the maximum and minimum simulated soil temperatures; and 3) the minimum and maximum probable CWSIs are computed by normalizing the minimum and maximum probable vegetation temperatures from the vegetation temperature extremes simulated by the energy budget model. The point is that this approach does not allow estimating a single CWSI value because the retrieval problem is underdetermined. In particular, Moran *et al.* [8] noted that "with knowledge of a second point within the hourglass (perhaps soil temperature), it would be possible to infer [the canopy-air temperature] difference and pinpoint the CWSI value." In the latter case, knowledge of soil temperature is equivalent to knowledge of soil evaporative efficiency, which would remove the underdetermination of the VIT trapezoid.

The objective of this paper is to develop a new disaggregation methodology of kilometric land surface temperature using hectometric multivariable ancillary data. The approach is based on a radiative transfer equation that estimates differences in temperature data at hectometric resolution. Specifically, the use of a radiative transfer equation allows the following: 1) including variables other than those used by previous disaggregation approaches and 2) deducing the most pertinent variables. In addition to fractional green and senescent vegetation covers, the new methodology includes the variability at hectometric resolution of fractional open water and soil evaporative efficiency. With respect to other disaggregation algorithms in literature [4], [5], the proposed technique differs in the following four main aspects: 1) it relies on a physically based radiative transfer equation rather than empirical linear regressions; 2) it takes into account the fractional open water derived from shortwave-infrared band as required; 3) it takes into account the soil hydric status via microwave-derived soil evaporative efficiency; and 4) it allows the relative weight of each parameter used for disaggregating temperature to be quantified.

The new disaggregation technique is compared to the existing approaches using data collected during the National Airborne Field Experiment in 2006 (NAFE'06; [9]). The experimental site covers a 5 km by 32 km irrigated agricultural area, which included approximately 5% of flooded rice crops during NAFE'06. Disaggregation algorithms are first tested by aggregating ASTER temperature at 1-km resolution and by comparing the disaggregated temperature to the high-resolution ASTER temperature initially used in the aggregation process. The application to aggregated ASTER data allows evaluating approaches independently of differences between ASTER and MODIS products [5]. Disaggregation algorithms are then applied to MODIS data.

II. Experimental Data

The study area is a 5 km by 32 km area included in the Coleambally Irrigation Area (CIA) located in the flat western plains of the Murrumbidgee catchment in southeastern Australia (35° S, 146° E). The principal summer crops grown in the CIA are rice, maize, and soybeans, while winter crops include wheat, barley, oats, and canola. In November, rice crops are flooded under 30 cm height of irrigation water.

The NAFE'06 was conducted from October 31 to November 20, 2006, over a 40 km by 60 km area, with more detailed flights over the 5 km by 32 km focus area studied in this paper. While a full description of the NAFE'06 data set is given in [9], a brief overview of the most pertinent details is provided here. The data used in this paper are comprised of airborne L-band brightness temperature; ASTER red, near-infrared, and shortwave-infrared reflectances; ASTER land surface temperature data (resampled at 250-m resolution); MODIS land surface temperature data; and air temperature data collected by a meteorological station in the NAFE'06 area.

A. PLMR

The Polarimetric L-band Multibeam Radiometer (PLMR) is an airborne instrument that measures both H and V polarizations using a single receiver with polarization switching at view angles of $\pm 7°$, $\pm 21.5°$, and $\pm 38.5°$. The accuracy of the PLMR is estimated to be better than 2 K and 3 K in the H and V polarization, respectively [10].

During NAFE'06, the PLMR flew on November 14 to collect L-band brightness temperature at 250-m resolution over the 5 km by 32 km area in the CIA. PLMR was mounted in the across-track configuration so that each pixel was observed at a

given incidence angle (approximately 7°, 21.5°, or 38.5°). Data were processed for incidence angle and beam location on the ground by taking into account aircraft position, attitude, and ground topography.

As the sensitivity to soil moisture is higher for H-polarized brightness temperature than for V-polarized brightness temperature, only the H-polarized brightness temperature TB is used in this paper. Preprocessing of TB consists of the following: 1) resampling H-polarized PLMR data at 250-m resolution on a grid that matches in symmetry to the flight lines over the 5 km by 32 km area and 2) converting the resampled TB to an equivalent value at 21.5° incidence angle. The incidence angle 21.5° is chosen to minimize conversion errors. The angular conversion involves the brightness temperature collected by inner beams at approximately 7° incidence angle being multiplied by the ratio $\overline{TB_{\rm MB}}/\overline{TB_{\rm IB}}$, with $\overline{TB_{\rm MB}}$ and $\overline{TB_{\rm IB}}$ being the mean brightness temperatures collected by the middle and inner beams, respectively. Similarly, the brightness temperature collected by the outer beams at approximately 38.5° incidence angle is multiplied by the ratio $\overline{TB_{\rm MB}}/\overline{TB_{\rm OB}}$, with $\overline{TB_{\rm OB}}$ being the mean brightness temperature collected by the outer beams. Mean brightness temperatures $\overline{TB_{\rm IB}}$, $\overline{TB_{\rm MB}}$, and $\overline{TB_{\rm OB}}$ are computed as the average (for all flight lines) of the TB collected by the beams pointing at $\pm 7°$, $\pm 21.5°$, and $\pm 38.5°$, respectively. This technique was already used in [11] to generate TB images by assuming that the impact of soil moisture and biomass on the angular dependance of TB is negligible or small. In this paper, a slightly different approach is adopted to take into account the variations in aircraft attitude during data collection, which made the incidence angle θ oscillate around 7°, 21.5°, and 38.5°. The brightness temperature $TB(\theta)$ observed at the incidence angle θ is multiplied by the ratio $\overline{TB_{\rm MB}}/\overline{TB_{\rm interp}(\theta)}$, with $\overline{TB_{\rm interp}(\theta)}$ being the mean brightness temperature linearly interpolated at θ incidence angle from the mean data collected by the inner, middle, and outer beams.

B. ASTER

The ASTER instrument was launched in 1999 aboard Terra, a sun synchronous platform with 11:00 UTC descending Equator crossing and a 16-day revisit cycle. An ASTER scene covers an area of approximately 60 km by 60 km and consists of 14 nadir-looking bands and one oblique-looking band to create stereo-based digital elevation models. The three nadir-looking bands in the visible and near infrared have a 15-m resolution. The six bands in the shortwave-infrared have a 30-m resolution. Finally, there are five thermal infrared bands with a 90-m resolution.

The ASTER overpass of the NAFE'06 site was on November 16, 2006. Official ASTER products [12] were used here for surface reflectance (AST_07) and radiometric temperature (AST_08) with accuracies of 5% and 1.5 K, respectively [13]–[19]. They were downloaded from the Earth Observing System Data Gateway (EDG).

ASTER 15-m resolution red (B2) and near-infrared (B3) bands were extracted over the 5 km by 32 km area and resampled at 250-m resolution to match the spatial resolution and extent of PLMR observations. The ASTER 30-m resolution B5 band (1.60–1.70 μm) was extracted over the 5 km by 32 km study area and resampled at 50-m resolution. Fractional open water was estimated using B5 band [20] based on a threshold method. Consequently, B5 data were resampled at a resolution finer than that (250 m) of PLMR data to classify open water pixels at 50-m resolution and to obtain fractional open water at 250-m resolution from the binary classification. ASTER 90-m resolution radiometric temperature was extracted over the 5 km by 32 km area and aggregated at 250-m resolution to match the spatial resolution and extent of PLMR observations. Aggregation was achieved by linearly averaging high-resolution surface temperatures, i.e., without accounting for the nonlinear relationship between physical temperature and radiance. This choice was motivated by the results of [21], which compared the temperature aggregated using different scaling approaches and obtained very low differences (maximum difference of 0.2 °C).

C. MODIS

The MODIS/Terra data were collected concurrently with ASTER data. MODIS official products consisted of the 928-m resolution surface skin temperature (MOD11-L2) retrieved by the "generalized split window" algorithm [22]–[24] and registered in the sinusoidal projection. The MODIS Reprojection Tool was used to project MOD11-L2 data in UTM WGS 1984 55S with a sampling interval of 1 km.

In this paper, the disaggregation of 1-km MODIS temperature is evaluated using high-resolution ASTER data. To distinguish the errors associated with the disaggregation technique and the errors associated with the discrepancy between MODIS and ASTER temperature products, a comparison is made between ASTER and MODIS data at 1-km resolution over the 5 km by 32 km study area. The ASTER data are aggregated at the MODIS spatial resolution (1 km) by linearly averaging high-resolution temperatures. The root-mean-square difference (RMSD), bias, correlation coefficient, and slope of the linear regression between MODIS and aggregated ASTER data are 2.7 °C, −2.3 °C, 0.75, and 0.52, respectively. The discrepancy between MODIS and ASTER data, which is mainly explained here by a significant bias and a relatively low slope of the linear regression, is on the same order of magnitude as the mean difference (about 3 °C) reported in literature [5], [21], [25].

III. Disaggregation Algorithms

This paper aims to compare different approaches for disaggregating kilometric MODIS land surface temperature data. The study uses aggregated ASTER and real MODIS data and demonstrates the disaggregation at 250-m resolution. The resolution of 250 m is chosen to match with the lowest resolution at which ancillary data composed of red, near-infrared, shortwave-infrared, and microwave-L bands are available. In this case study, the target scale is determined by the resolution (250 m) of airborne microwave data.

As shown in the schematic diagram of Fig. 1, the disaggregation algorithms are noted as Dk, with k being the number of factors taken into account in the disaggregation. The new

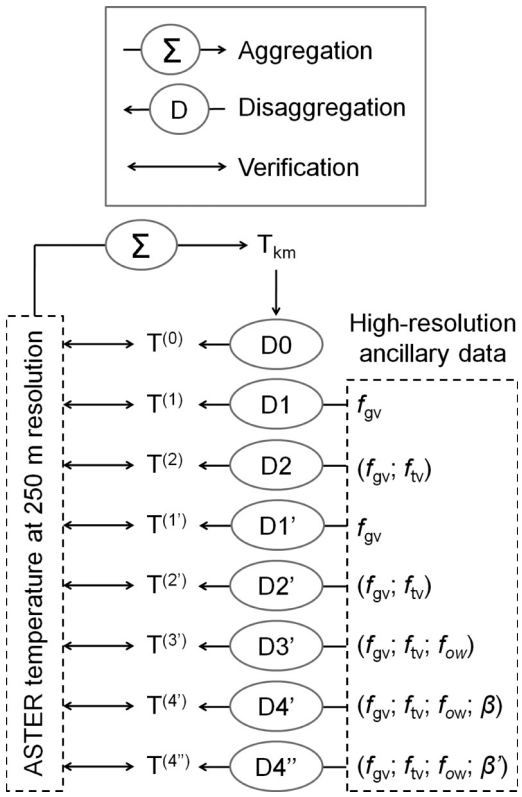

Fig. 1. Schematic diagram presenting the different disaggregation algorithms of kilometric temperature $T_{\rm km}$ and the verification strategy at high (250 m) resolution.

algorithms are noted as Dk$'$. D0 does not use any ancillary data, while D1 is based on a linear regression between land surface temperature and fractional green (photosynthetically active) vegetation cover. Fractional green vegetation cover $f_{\rm gv}$ is defined as the surface area of green vegetation per unit area of soil. D1 is the same as in [4]. D2 is based on D1 but takes into account both fractional green and total vegetation covers. Fractional vegetation cover $f_{\rm tv}$ is defined as the total surface area of (green plus senescent) vegetation per unit area of soil. D2 is the same as in [5]. The new algorithms D1$'$, D2$'$, D3$'$, and D4$'$ (and D4$''$) are all derived from a radiative transfer equation. The four algorithms differ with regard to the number of factors which are explicitly taken into account. D1$'$ includes the variability of $f_{\rm gv}$ and is thus a substitute for D1 based on radiative transfer. D2$'$ includes the variability of both $f_{\rm gv}$ and $f_{\rm tv}$ and is thus a substitute for D2 based on radiative transfer. The other algorithms D3$'$ and D4$'$ integrate additional variables. D3$'$ includes the variability of $f_{\rm gv}$, $f_{\rm tv}$, and fractional open water $f_{\rm ow}$. D4$'$ includes the variability of $f_{\rm gv}$, $f_{\rm tv}$, $f_{\rm ow}$, and soil evaporative efficiency (ratio of actual to potential soil evaporation) β. D4$''$ is the same as D4$'$ but with a different formulation for soil evaporative efficiency.

D0 sets the disaggregated temperature as

$$T^{(0)} = T_{\rm km} \tag{1}$$

with $T_{\rm km}$ being the land surface temperature observed at kilometric resolution.

Using D1, the disaggregated temperature is computed as

$$T^{(1)} = T_{\rm km} + \mathbf{a_1} \times (f_{\rm gv} - \langle f_{\rm gv}\rangle_{\rm km}) \tag{2}$$

with $f_{\rm gv}$ being the fractional green vegetation cover derived at high resolution, $\langle f_{\rm gv}\rangle_{\rm km}$ being the $f_{\rm gv}$ aggregated at kilometric resolution, and $\mathbf{a_1}$ being the slope of the linear regression between $T_{\rm km}$ and $\langle f_{\rm gv}\rangle_{\rm km}$. Note that the variables defined at kilometric resolution are noted with the subscript km.

Using D2, the disaggregated temperature is computed as

$$T^{(2)} = T_{\rm km} + \mathbf{a_1^{proj}} \times \left(f_{\rm gv}^{\rm proj} - \langle f_{\rm gv}\rangle_{\rm km}\right) \tag{3}$$

with $f_{\rm gv}^{\rm proj}$ being the projected $f_{\rm gv}$ and $\mathbf{a_1^{proj}}$ being the slope of the linear regression between $T_{\rm km}$ and the projected $f_{\rm gv}$ estimated at kilometric resolution $f_{\rm gv,km}^{\rm proj}$. Note that the variables defined at the image scale are written in bold. The notion of a "projected variable" was introduced in [26]. It is a robust tool that strenghtens the correlation between two variables by representing the dependence of these variables on other additional variables. In [5], the projection technique was applied to fractional green vegetation cover to artificially improve the spatial correlation between T and $f_{\rm gv}$ by taking into account the dependence of T on $f_{\rm tv}$. The projected fractional green vegetation cover is computed as

$$f_{\rm gv}^{\rm proj} = f_{\rm gv} - \frac{\mathbf{T_{fcsv}} - (\mathbf{T_{b,ds}} + \mathbf{T_{b,ws}})/2}{\mathbf{T_{fcsv}} - \mathbf{T_{fcgv}}} \times (f_{\rm tv} - \langle f_{\rm tv}\rangle_{\rm km}) \tag{4}$$

with $f_{\rm tv}$ being the fractional total vegetation cover derived at high resolution, $\langle f_{\rm tv}\rangle_{\rm km}$ being the $f_{\rm tv}$ aggregated at kilometric resolution, $\mathbf{T_{b,ws}}$ being the temperature of wet bare soil, $\mathbf{T_{b,ds}}$ being the temperature of dry bare soil, $\mathbf{T_{fcgv}}$ being the temperature of full-cover green vegetation, and $\mathbf{T_{fcsv}}$ being the temperature of full-cover senescent vegetation (notations are summarized in Table I). Following the interpretation of the "triangle method" [27], $\mathbf{T_{b,ws}}$, $\mathbf{T_{b,ds}}$, $\mathbf{T_{fcgv}}$, and $\mathbf{T_{fcsv}}$ correspond to the minimum and maximum soil and vegetation temperatures within the study area, respectively. It is reminded that $f_{\rm tv} = f_{\rm gv} + f_{\rm sv}$, with $f_{\rm gv}$ and $f_{\rm sv}$ being the fractional green and senescent vegetation covers, respectively.

In (4), the projected fractional green vegetation cover estimated at kilometric resolution is

$$f_{\rm gv,km}^{\rm proj} = \langle f_{\rm gv}\rangle_{\rm km} - \frac{\mathbf{T_{fcsv}} - (\mathbf{T_{b,ds}} + \mathbf{T_{b,ws}})/2}{\mathbf{T_{fcsv}} - \mathbf{T_{fcgv}}} \times (\langle f_{\rm tv}\rangle_{\rm km} - \mathbf{f_{tv}}) \tag{5}$$

with $\mathbf{f_{tv}}$ being the mean $f_{\rm tv}$ over the whole study area.

The new algorithms D$'$ use a radiative transfer equation to model the spatial variability of disaggregated temperature within each 1-km resolution pixel, using ancillary data available at high resolution such as $f_{\rm gv}$, $f_{\rm tv}$, $f_{\rm ow}$, and β. D1$'$ is a substitute for D1 based on radiative transfer. It expresses disaggregated temperature as

$$T^{(1')} = T_{\rm km} + \Delta T^{(1')} \tag{6}$$

TABLE I
INTERPRETATION OF THE VERTICES IN THE GENERALIZED "TRIANGLE APPROACH"

Vertex	Surface type	Near-surface soil hydric status	Abbreviation
A	Bare soil	Dry	b,ds
B	Bare soil	Wet	b,ws
C	Full-cover green vegetation	Wet or dry	fcgv
C′	Full-cover green vegetation	Wet	fcgv,ws
C″	Full-cover green vegetation	Dry	fcgv,ds
D	Full-cover senescent vegetation	Wet or dry	fcsv
D′	Full-cover senescent vegetation	Dry	fcsv,ds

with $\Delta T^{(1')}$ being the difference between the temperature simulated using high-resolution $f_{\rm gv}$ and that aggregated within the 1-km resolution pixel

$$\Delta T^{(1')} = T_{\rm mod}\ (f_{\rm gv}, \langle f_{\rm tv}\rangle_{\rm km}, \langle f_{\rm ow}\rangle_{\rm km}, \langle\beta\rangle_{\rm km}) - \langle T_{\rm mod}\ (f_{\rm gv}, \langle f_{\rm tv}\rangle_{\rm km}, \langle f_{\rm ow}\rangle_{\rm km}, \langle\beta\rangle_{\rm km})\rangle_{\rm km} \quad (7)$$

with $T_{\rm mod}$ being the land surface temperature simulated by a radiative transfer equation. In (7), fractional total vegetation cover, fractional open water, and soil evaporative efficiency are set to their values aggregated at kilometric resolution. Therefore, only the variability of $f_{\rm gv}$ is taken into account at high resolution.

D2′ is a substitute for D2 based on radiative transfer. It expresses the disaggregated temperature as in (6), with the simulated temperature difference $\Delta T^{(2')}$ written as

$$\Delta T^{(2')} = T_{\rm mod}\ (f_{\rm gv}, f_{\rm tv}, \langle f_{\rm ow}\rangle_{\rm km}, \langle\beta\rangle_{\rm km}) - \langle T_{\rm mod}\ (f_{\rm gv}, f_{\rm tv}, \langle f_{\rm ow}\rangle_{\rm km}, \langle\beta\rangle_{\rm km})\rangle_{\rm km}. \quad (8)$$

D3′ is derived from the same radiative transfer equation and includes the variability of $f_{\rm gv}$, $f_{\rm tv}$, and $f_{\rm ow}$ at high resolution. It determines the disaggregated temperature using (6) but with the simulated temperature difference $\Delta T^{(3')}$ written as

$$\Delta T^{(3')} = T_{\rm mod}\ (f_{\rm gv}, f_{\rm tv}, f_{\rm ow}, \langle\beta\rangle_{\rm km}) - \langle T_{\rm mod}\ (f_{\rm gv}, f_{\rm tv}, f_{\rm ow}, \langle\beta\rangle_{\rm km})\rangle_{\rm km}. \quad (9)$$

D4′ is derived from the same radiative transfer equation and includes the variability of $f_{\rm gv}$, $f_{\rm tv}$, $f_{\rm ow}$, and β at high resolution. It determines the disaggregated temperature using (6) but with the simulated temperature difference $\Delta T^{(4')}$ written as

$$\Delta T^{(4')} = T_{\rm mod}\,(f_{\rm gv}, f_{\rm tv}, f_{\rm ow}, \beta) - \langle T_{\rm mod}\,(f_{\rm gv}, f_{\rm tv}, f_{\rm ow}, \beta)\rangle_{\rm km}. \quad (10)$$

D4″ is an extension of (10) to replace β by another formulation of soil evaporative efficiency noted as β'.

The high- to low-resolution simulated temperature difference in (7)–(10) is computed using a linearized radiative transfer equation [5], [28], [29]. Modeled land surface temperature $T_{\rm mod}$ is written as

$$T_{\rm mod} = f_{\rm ow}T_{\rm ow} + (1 - f_{\rm ow})T_{\rm nw} \quad (11)$$

with $T_{\rm ow}$ being the surface temperature of a water body and $T_{\rm nw}$ being the skin temperature of a nonwatered land surface. Nonwatered land surface temperature is expressed as

$$T_{\rm nw} = f_{\rm gv}\mathbf{T_{fcgv}} + (f_{\rm tv} - f_{\rm gv})\mathbf{T_{fcsv}} + (1 - f_{\rm tv})T_{\rm bs} \quad (12)$$

with $\mathbf{T_{fcgv}}$ and $\mathbf{T_{fcsv}}$ being the temperature of full-cover green and senescent vegetations, respectively, and $T_{\rm bs}$ being the bare soil temperature. With the soil evaporative efficiency defined [30] as

$$\beta = \frac{\mathbf{T_{b,ds}} - T_{\rm bs}}{\mathbf{T_{b,ds}} - \mathbf{T_{b,ws}}} \quad (13)$$

the bare soil temperature can be expressed as

$$T_{\rm bs} = \beta\mathbf{T_{b,ws}} + (1 - \beta)\mathbf{T_{b,ds}}. \quad (14)$$

By assuming that water temperature is close to well-watered green vegetation [27], modeled land surface temperature becomes

$$T_{\rm mod} = f_{\rm ow}\mathbf{T_{fcgv}} + (1 - f_{\rm ow})T_{\rm nw} \quad (15)$$

with the nonwatered land surface temperature expressed as

$$T_{\rm nw} = f_{\rm gv}\mathbf{T_{fcgv}} + (f_{\rm tv} - f_{\rm gv})\mathbf{T_{fcsv}} + (1 - f_{\rm tv})\left[\beta\mathbf{T_{b,ws}} + (1 - \beta)\mathbf{T_{b,ds}}\right]. \quad (16)$$

The temperature extremes $\mathbf{T_{b,ds}}$, $\mathbf{T_{b,ws}}$, $\mathbf{T_{fcgv}}$, and $\mathbf{T_{fcsv}}$ are extrapolated (according to Section V) from low-resolution land surface temperatures using high-resolution ancillary data [5].

IV. DERIVATION OF BIOPHYSICAL VARIABLES

The four variables used by the disaggregation methodology are the following: fractional green vegetation cover $f_{\rm gv}$, fractional total (green plus senescent) vegetation cover $f_{\rm tv}$, fractional open water $f_{\rm ow}$, and soil evaporative efficiency β. All of these variables are estimated from ASTER red, near-infrared, and shortwave-infrared reflectance products and from the PLMR H-polarized brightness temperature converted at an incidence angle of 21.5°.

A. Fractional Green Vegetation Cover

Fractional green vegetation cover can be estimated from the Normalized Difference Vegetation Index (NDVI) as in [31]

$$f_{\rm gv} = \frac{\rm NDVI - \mathbf{NDVI_{bs}}}{\mathbf{NDVI_{fcgv}} - \mathbf{NDVI_{bs}}} \quad (17)$$

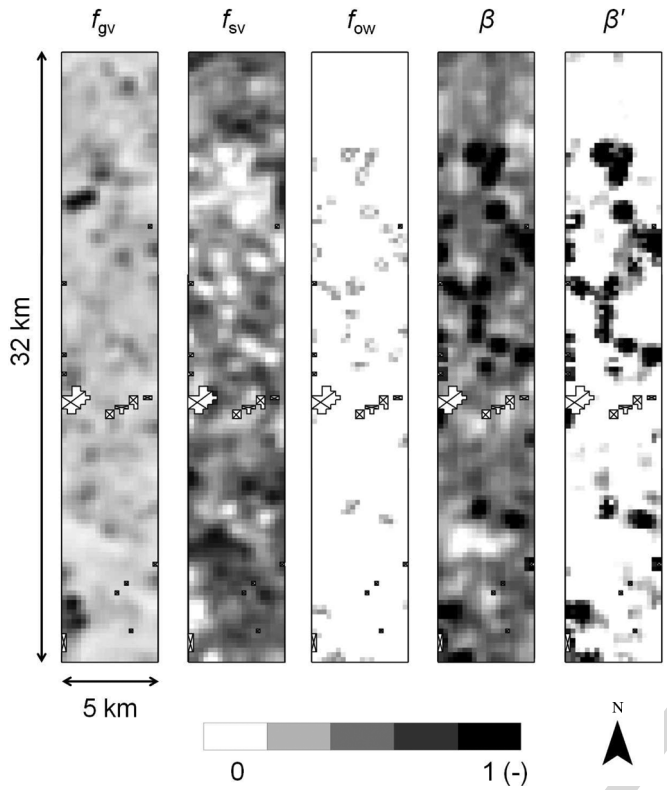

Fig. 2. Images of fractional green vegetation cover $f_{\rm gv}$, fractional senescent vegetation cover $f_{\rm sv} = f_{\rm tv} - f_{\rm gv}$, fractional open water $f_{\rm ow}$, soil evaporative efficiency β, and soil evaporative efficiency β'. Note that 2% of the 5 km by 32 km area is contaminated by clouds and cloud shadow. Contaminated 250-m resolution pixels are represented by crossed-out surfaces.

with $\mathbf{NDVI_{bs}}$ and $\mathbf{NDVI_{fcgv}}$ being the NDVI over bare soil and full-cover green vegetation, respectively. NDVI is computed as the difference between near-infrared and red bands divided by their sum. The spatial variation of fractional green vegetation cover over the study area is shown in Fig. 2.

B. Fractional Total (Green Plus Senescent) Vegetation Cover

Fractional total vegetation cover is estimated by correlating $f_{\rm tv}$ with surface albedo for green vegetation and by setting $f_{\rm tv}$ to the maximum $f_{\rm gv}$ for senescent vegetation. This methodology [5] is based on two assumptions, which are generally met in agricultural areas: 1) soil albedo is generally lower than green vegetation albedo, and 2) green vegetation albedo is lower than senescent vegetation albedo. Although a time series of red and near-infrared data would be required to estimate soil albedo and green vegetation albedo on a pixel-by-pixel basis [5], only one ASTER scene is available for this study period. Therefore, an alternate approach is adopted. Surface albedo is modeled as a linear mixing of vegetation and soil components (e.g., [32] and [33])

$$\alpha = (1 - f_{\rm tv})\alpha_{\mathbf{bs}} + f_{\rm gv}\alpha_{\mathbf{fcgv}} + (f_{\rm tv} - f_{\rm gv})\alpha_{\mathbf{fcsv}} \qquad (18)$$

with $\alpha_{\mathbf{bs}}$, $\alpha_{\mathbf{fcgv}}$, and $\alpha_{\mathbf{fcsv}}$ being the albedo for bare soil, full-cover green vegetation, and full-cover senescent vegetation, respectively, and with the end-members $\alpha_{\mathbf{bs}}$, $\alpha_{\mathbf{fcgv}}$, and $\alpha_{\mathbf{fcsv}}$ estimated in Section V.

By inverting (18), fractional vegetation cover is expressed as

$$f_{\rm tv} = \frac{\alpha - \alpha_{\mathbf{bs}} + f_{\rm gv}(\alpha_{\mathbf{fcsv}} - \alpha_{\mathbf{fcgv}})}{\alpha_{\mathbf{fcsv}} - \alpha_{\mathbf{bs}}} \qquad (19)$$

with α being the surface albedo estimated as a weighted sum of red and near-infrared reflectances using the coefficients given in [34] and validated in [35]–[38]. As stated previously, our case study does not allow calibrating $\alpha_{\mathbf{bs}}$, $\alpha_{\mathbf{fcgv}}$, and $\alpha_{\mathbf{fcsv}}$ on a pixel-by-pixel basis. Consequently, the value of $f_{\rm tv}$ computed from (19) may, on some occasions, be lower than $f_{\rm gv}$ or larger than 1. To avoid nonphysical values, $f_{\rm tv}$ is set to $f_{\rm gv}$ and 1 in the former and latter case, respectively.

The spatial variation of fractional senescent vegetation cover ($f_{\rm sv} = f_{\rm tv} - f_{\rm gv}$) over the study area is shown in Fig. 2. Note that NAFE'06 was undertaken at the beginning of the summer agricultural season so that all irrigated crops were green and healthy.

C. Fractional Open Water

The fraction of open water within each 250-m resolution pixel is estimated using 50-m resolution resampled ASTER B5 reflectance product. Various studies have indicated that the shortwave-infrared band centered at around 1 μm is highly sensitive to the presence of open water [20], [39], [40]. In this paper, a simple threshold method is applied to classify at 50-m resolution the 5 km by 32 km area in two classes: water and nonwatered surface. The threshold value is estimated as 0.170 from one flooded crop field in the south of the study area. The spatial variation of fractional open water over the study area is shown in Fig. 2. Open water represents 5% of the study area and is attributed to rice cropping.

D. Soil Evaporative Efficiency

Soil evaporative efficiency β is defined as the ratio of actual to potential soil evaporation. In this paper, β is estimated from PLMR brightness temperatures. Two different formulations are used to evaluate the coupling effects of near-surface soil moisture, $f_{\rm gv}$, and $f_{\rm sv}$ on microwave-derived soil evaporative efficiency.

By assuming that brightness temperature is mainly sensitive to surface soil moisture [41] and that soil evaporative efficiency is mainly driven by surface soil moisture [42], [43], soil evaporative efficiency can be estimated as

$$\beta = 1 - \frac{TB - \mathbf{TB_{b,ws}}}{\mathbf{TB_{fcsv,ds}} - \mathbf{TB_{b,ws}}} \qquad (20)$$

with $\mathbf{TB_{b,ws}}$ and $\mathbf{TB_{fcsv,ds}}$ being the minimum and maximum brightness temperatures observed over the study area, respectively. As brightness temperature generally decreases with surface soil moisture and increases with vegetation cover [44], $\mathbf{TB_{b,ws}}$ and $\mathbf{TB_{fcsv,ds}}$ are interpreted as the brightness temperatures over wet bare soil and full-cover senescent vegetation with dry soil, respectively. The spatial variation of β over the study area is shown in Fig. 2.

Since brightness temperature also depends on biomass (e.g., [45]), a second formulation of soil evaporative efficiency β' is

TABLE II
NDVI AND SURFACE ALBEDO END-MEMBERS

End-member	Value	Unit
$\mathbf{NDVI_{bs}}$	0.15	-
$\mathbf{NDVI_{fcgv}}$	0.65	-
$\alpha_{\mathbf{bs}}$	0.17	-
$\alpha_{\mathbf{fcgv}}$	0.22	-
$\alpha_{\mathbf{fcsv}}$	0.31	-

derived in order to decouple the effects of soil moisture, $f_{\rm gv}$, and $f_{\rm sv}$ on TB. As in [46], the assumption is that, for a given vegetated pixel, if vegetation is partially stressed (i.e., $f_{\rm sv} > 0$ or $f_{\rm tv} > f_{\rm gv}$), then near-surface soil moisture availability is zero (i.e., $\beta' = 0$). Alternatively, if that pixel does not contain senescent vegetation (i.e., $f_{\rm sv} = 0$ or $f_{\rm tv} = f_{\rm gv}$), then β' is computed as the ratio of the measured "wet soil" brightness temperature difference to the "dry soil"–"wet soil" brightness temperature difference. Formally, one writes

$$\beta' = 0 \quad \text{if} \quad TB > TB_{\mathbf{ds}} \tag{21}$$

$$\beta' = 1 - \frac{TB - TB_{\mathbf{ws}}}{TB_{\mathbf{ds}} - TB_{\mathbf{ws}}} \quad \text{if} \quad TB \leq TB_{\mathbf{ds}} \tag{22}$$

with $TB_{\mathbf{ds}}$ and $TB_{\mathbf{ws}}$ being the "dry soil" and "wet soil" brightness temperatures, respectively, both being estimated for $f_{\rm sv} = 0$. Since green vegetation is partially transparent to microwaves, the "dry soil" brightness temperature is computed as a weighted sum of the brightness temperature over dry bare soil (noted as $\mathbf{TB_{b,ds}}$) and the brightness temperature over full-cover green vegetation with dry soil (noted as $\mathbf{TB_{fcgv,ds}}$)

$$TB_{\mathbf{ds}} = f_{\rm gv}\mathbf{TB_{fcgv,ds}} + (1 - f_{\rm gv})\mathbf{TB_{b,ds}}. \tag{23}$$

Similarly, the "wet soil" brightness temperature is computed as a weighted sum of the brightness temperature over wet bare soil (noted as $\mathbf{TB_{b,ws}}$) and the brightness temperature over full-cover green vegetation with wet soil (noted as $\mathbf{TB_{fcgv,ws}}$)

$$TB_{\mathbf{ws}} = f_{\rm gv}\mathbf{TB_{fcgv,ws}} + (1 - f_{\rm gv})\mathbf{TB_{b,ws}}. \tag{24}$$

The spatial variation of β' over the study area is shown in Fig. 2.

V. ESTIMATING END-MEMBERS

A key step in the disaggregation procedure is estimating the 14 end-members from ASTER and PLMR data. They are composed of the following: $\mathbf{NDVI_{bs}}$, $\mathbf{NDVI_{fcgv}}$, $\alpha_{\mathbf{bs}}$, $\alpha_{\mathbf{fcgv}}$, $\alpha_{\mathbf{fcsv}}$, $\mathbf{T_{b,ws}}$, $\mathbf{T_{b,ds}}$, $\mathbf{T_{fcgv}}$, $\mathbf{T_{fcsv}}$, $\mathbf{TB_{b,ws}}$, $\mathbf{TB_{b,ds}}$, $\mathbf{TB_{fcgv,ws}}$, $\mathbf{TB_{fcgv,ds}}$, and $\mathbf{TB_{fcsv,ds}}$. For the convenience of the reader, the unit is degree Celsius for radiometric temperature and kelvin for brightness temperature.

A. NDVI

NDVI end-members are estimated as the minimum and maximum values of NDVI observed over the 5 km by 32 km area for bare soil and full-cover green vegetation, respectively. Values for $\mathbf{NDVI_{bs}}$ and $\mathbf{NDVI_{fcgv}}$ are reported in Table II.

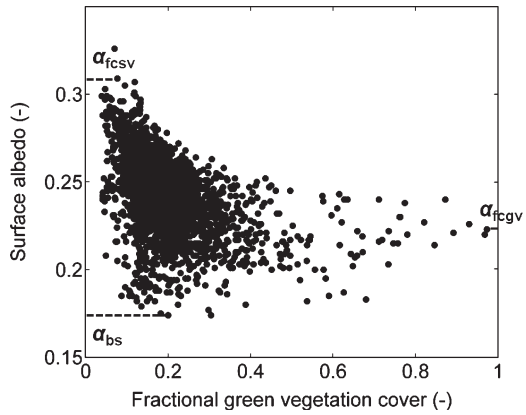

Fig. 3. ASTER surface albedo α plotted against ASTER fractional green vegetation cover $f_{\rm gv}$. Three particular values of α are identified: the soil albedo $\alpha_{\mathbf{bs}}$ estimated as the minimum surface albedo, the green vegetation albedo $\alpha_{\mathbf{fcgv}}$ estimated as the albedo corresponding to the largest $f_{\mathbf{gv}}$, and the senescent vegetation albedo $\alpha_{\mathbf{fcsv}}$ estimated as the maximum surface albedo.

In this paper, the study domain included extreme conditions in terms of vegetation cover so that NDVI end-members could be estimated from the red and near-infrared reflectances acquired over the area on a single date. In the case where extreme conditions are not encountered in the application domain, a different approach should be adopted, such as the use of a time series of NDVI data (instead of a single snapshot image) that would capture the phenological stages of agricultural crops. Also, the determination of reflectance end-members could be further constrained by the use of ancillary spectral data sets [47].

B. Albedo

Fig. 3 shows the space defined by surface albedo α and fractional green vegetation cover $f_{\rm gv}$. Pixels including open water are removed from the scatterplot. The soil albedo $\alpha_{\mathbf{bs}}$ is defined as the minimum ASTER surface albedo observed within the study area by assuming that the dependence of $\alpha_{\mathbf{bs}}$ on soil moisture is small compared to the dependence of α on vegetation cover. The green vegetation albedo $\alpha_{\mathbf{fcgv}}$ is estimated as the surface albedo corresponding to maximum fractional green vegetation cover. The senescent vegetation albedo $\alpha_{\mathbf{fcsv}}$ is estimated as the maximum surface albedo observed within the study area. Values for $\alpha_{\mathbf{bs}}$, $\alpha_{\mathbf{fcgv}}$, and $\alpha_{\mathbf{fcsv}}$ are reported in Table II.

C. Land Surface Temperature

As the range of surface conditions varies with spatial resolution, two different procedures are developed to estimate temperature end-members.

1) When estimating temperature end-members from 250-m resolution data, one pixel is identified as fully covered green vegetation, one pixel as fully covered senescent vegetation, one pixel as bare dry soil, and one pixel as bare wet soil. In this case, it is assumed that all extreme conditions are included at high resolution within the study domain.

TABLE III
LAND SURFACE TEMPERATURE AND L-BAND BRIGHTNESS TEMPERATURE END-MEMBERS THAT ARE ESTIMATED FROM HIGH-RESOLUTION ASTER TEMPERATURE DATA, EXTRAPOLATED FROM AGGREGATED ASTER TEMPERATURE DATA, AND EXTRAPOLATED FROM MODIS TEMPERATURE DATA. FOR THE CONVENIENCE OF THE READER, THE UNIT IS DEGREE CELSIUSFOR RADIOMETRIC TEMPERATURE AND KELVIN FOR BRIGHTNESS TEMPERATURE

AQ3

End-member	High-resolution T	Aggregated ASTER $T_{\rm km}$	MODIS $T_{\rm km}$	Unit
$\mathbf{T_{b,ds}}$	38	40.2	38.9	°C
$\mathbf{T_{b,ws}}$	25	27.6	26.2	°C
$\mathbf{T_{fcgv}}$	21	21.0	21.0	°C
$\mathbf{T_{fcsv}}$	34	32.0	28.7	°C
$\mathbf{TB_{b,ds}}$	240	246	241	K
$\mathbf{TB_{b,ws}}$	190	193	193	K
$\mathbf{TB_{fcgv,ws}}$	205	205	205	K
$\mathbf{TB_{fcgv,ds}}$	240	240	240	K
$\mathbf{TB_{fcsv,ds}}$	280	280	280	K

2) When estimating temperature end-members from 1-km resolution data (as in the operational scenario), none of the pixels are identified as representative of any extreme condition. Temperature end-members are extrapolated from 1-km temperature data using ancillary data composed of air temperature, soil albedo, green vegetation albedo, and senescent vegetation albedo as described in the following.

End-members $\mathbf{T_{b,ws}}$, $\mathbf{T_{b,ds}}$, $\mathbf{T_{fcgv}}$, and $\mathbf{T_{fcsv}}$ are determined by analyzing the consistency of the diagrams in Fig. 4. Fig. 4(a) shows the space defined by ASTER land surface temperature and ASTER fractional green vegetation cover. The three edges of the triangle $T - f_{\rm gv}$ are interpreted [27] as "bare soil" between $\mathbf{A}$ and $\mathbf{B}$, "wet surface" between $\mathbf{B}$ and $\mathbf{C}$, and "dry soil" between $\mathbf{C}$ and $\mathbf{A}$. Fig. 4(b) shows the space defined by ASTER land surface temperature and ASTER surface albedo. An interpretation of the polygon $T - \alpha$ is provided in [5], which is consistent with the triangle method. The four edges are interpreted as "bare soil" between $\mathbf{A}$ and $\mathbf{B}$, "wet surface" between $\mathbf{B}$ and $\mathbf{C}$, "full cover" between $\mathbf{C}$ and $\mathbf{D}$, and "dry surface" between $\mathbf{D}$ and $\mathbf{A}$. The notation system for polygon vertices $\mathbf{A}$, $\mathbf{B}$, $\mathbf{C}$, and $\mathbf{D}$ is summarized in Table I, and the corresponding temperature values $\mathbf{T_{b,ds}}$, $\mathbf{T_{b,ws}}$, $\mathbf{T_{fcgv}}$, and $\mathbf{T_{fcsv}}$ are reported in Table III.

In this paper, high-resolution temperature T is assumed to be unavailable. Consequently, the extreme temperatures $\mathbf{T_{b,ds}}$, $\mathbf{T_{b,ws}}$, $\mathbf{T_{fcgv}}$, and $\mathbf{T_{fcsv}}$ are extrapoled from the spaces $T_{\rm km} - \langle f_{\rm gv}\rangle_{\rm km}$ and $T_{\rm km} - \langle\alpha\rangle_{\rm km}$ defined at kilometric resolution (see Fig. 4(c) and (d) for aggregated ASTER temperature and Fig. 4(e) and (f) for MODIS temperature). An approach similar to [5] is used as follows.

1) Vertex $\mathbf{C}$ corresponds to full-cover green vegetation and is located at $(1, \mathbf{T_{fcgv}})$ in Fig. 4(c) (Fig. 4(e) for MODIS temperature) and at $(\alpha_{\mathbf{fcgv}}, \mathbf{T_{fcgv}})$ in Fig. 4(d) [Fig. 4(f)]. In this paper, $\mathbf{T_{fcgv}}$ is set to the air temperature $\mathbf{T_a}$ measured at the time of ASTER overpass. Vertex $\mathbf{C}$ is thus placed at $(1, \mathbf{T_a})$ in Fig. 4(c) [Fig. 4(e)] and at $(\alpha_{\mathbf{fcgv}}, \mathbf{T_a})$ in Fig. 4(d) [Fig. 4(f)].

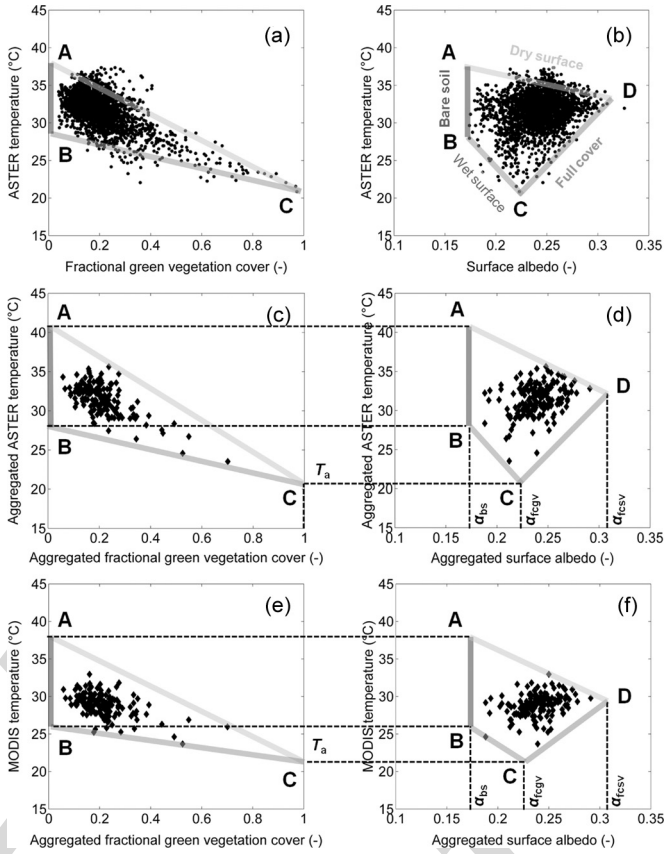

Fig. 4. (a) Scatterplot of ASTER temperature versus fractional green vegetation cover and (b) versus surface albedo, (c) scatterplot of aggregated ASTER temperature versus aggregated fractional green vegetation cover and (d) versus aggregated surface albedo, and (e) scatterplot of MODIS temperature versus aggregated fractional green vegetation cover and (f) versus aggregated surface albedo. The vertices $\mathbf{A}$, $\mathbf{B}$, $\mathbf{C}$, and $\mathbf{D}$ obtained using high-resolution data in (a) and (b) are extrapolated using low-resolution data in (c), (d), (e), and (f) from ancillary data composed of air temperature $\mathbf{T_a}$, soil albedo $\alpha_{\mathbf{bs}}$, green vegetation albedo $\alpha_{\mathbf{fcgv}}$, and senescent vegetation albedo $\alpha_{\mathbf{fcsv}}$.

2) Vertex $\mathbf{B}$ corresponds to wet bare soil and is located at $(0, \mathbf{T_{b,ws}})$ in Fig. 4(c) [Fig. 4(e)] and at $(\alpha_{\mathbf{bs}}, \mathbf{T_{b,ws}})$ in Fig. 4(d) [Fig. 4(f)]. It is placed in Fig. 4(c) [Fig. 4(e)] at the intersection between $(\mathbf{BC})$ and the vertical line $\langle f_{\rm gv}\rangle_{\rm km} = 0$. The slope of $(\mathbf{BC})$ is computed as the slope of the linear regression of the data points corresponding to the "wet surface" edge of the triangle $T_{\rm km} - \langle f_{\rm gv}\rangle_{\rm km}$. The off-set of $(\mathbf{BC})$ is determined from $\mathbf{C}$.
3) Vertex $\mathbf{A}$ corresponds to dry bare soil and is located at $(0, \mathbf{T_{b,ds}})$ in Fig. 4(c) [Fig. 4(e)] and at $(\alpha_{\mathbf{bs}}, \mathbf{T_{b,ds}})$ in Fig. 4(d) [Fig. 4(f)]. It is placed in Fig. 4(c) [Fig. 4(e)] at the intersection between $(\mathbf{AC})$ and the vertical line $\langle f_{\rm gv}\rangle_{\rm km} = 0$. The slope of $(\mathbf{AC})$ is computed as the slope of the linear regression of the data points corresponding to the "dry soil" edge of the triangle $T_{\rm km} - \langle f_{\rm gv}\rangle_{\rm km}$. The off-set of $(\mathbf{AC})$ is determined from $\mathbf{C}$.
4) Vertex $\mathbf{D}$ corresponds to full-cover senescent vegetation and is located at $(\alpha_{\mathbf{fcsv}}, \mathbf{T_{fcsv}})$ in Fig. 4(d) [Fig. 4(f)]. It is placed in Fig. 4(d) [Fig. 4(f)] at the intersection between $(\mathbf{AD})$ and the vertical line $\langle\alpha\rangle_{\rm km} = \alpha_{\mathbf{fcsv}}$. The line $(\mathbf{AD})$ is considered as being parallel to $(\mathbf{BC})$[5]. Consequently, the slope of $(\mathbf{AD})$ is determined from

the slope of $(\mathbf{BC})$. The off-set of $(\mathbf{AD})$ is determined from $\mathbf{A}$. Note that the lines $(\mathbf{AD})$ and $(\mathbf{BC})$ might not be strictly parallel. This may be due to a lack of representativeness of the surface conditions captured at 250-m resolution within the study area. In that case, one or several data points may be located above $(\mathbf{AD})$. To circumvent this artifact, the slope of $(\mathbf{AD})$ in Fig. 4(d) [Fig. 4(f)] is increased so that all data points will be located below the "dry surface" edge.

Table III lists the four temperature end-members: 1) estimated from Fig. 4(a) and (b) using high-resolution ASTER data; 2) extrapolated from Fig. 4(c) and (d) using aggregated ASTER temperature data; and 3) extrapolated from Fig. 4(e) and (f) using MODIS temperature data. The values extrapolated from aggregated ASTER and MODIS temperatures are rather close to those estimated from high-resolution ASTER temperature data, with the maximum difference in extrapolated temperatures being 2.6 °C, except for $\mathbf{T_{fcsv}}$ using MODIS data. In the latter case, the significant underestimation (5.3 °C) of $\mathbf{T_{fcsv}}$ can be explained by the following: 1) the negative mean difference $(-2.3\ ^\circ\mathrm{C})$ between MODIS and ASTER data and/or 2) the smaller range of (spatial dynamics) of 1-km resolution MODIS data in relation to 1-km aggregated ASTER data [please compare Fig. 4(c) with Fig. 4(e), and Fig. 4(d) with Fig. 4(f)].

D. Brightness Temperature

To estimate soil evaporative efficiency β in (20) and β' in (22), five brightness temperature values corresponding to extreme surface conditions are required: $\mathbf{TB_{b,ds}}$, $\mathbf{TB_{b,ws}}$, $\mathbf{TB_{fcgv,ws}}$, $\mathbf{TB_{fcgv,ds}}$, and $\mathbf{TB_{fcsv,ds}}$. In this paper, those five values are estimated from a generalized version [5], [9] of the classical "triangle method" [27].

Fig. 5(a) shows the space defined by PLMR brightness temperature and ASTER land surface temperature. In the following, an original interpretation of the five vertices visible in Fig. 5(a) is provided, which is consistent with both the classical "triangle method" and the state-of-the-art L-band radiative transfer models. Vertices are presented successively in the counterclockwise direction, and the correspondence with vegetation and soil conditions is summarized in Table I.

1) Vertex at minimum brightness temperature: L-band radiative transfer models predict an increase of brightness temperature with biomass and a decrease of brightness temperature with surface soil moisture (e.g., [48] and [49]). Therefore, the point at minimum brightness temperature corresponds to wet bare soil. This vertex is noted as $\mathbf{B}$ in Fig. 5(a), which is consistent with Fig. 4.
2) Vertex at maximum land surface temperature: the triangle method predicts a decrease of land surface temperature with both vegetation cover and surface soil moisture. Therefore, the point at maximum land surface temperature corresponds to dry bare soil. This vertex is noted as $\mathbf{A}$ in Fig. 5(a), which is consistent with Fig. 4.
3) Vertex at maximum brightness temperature: being consistent with an increase of vegetation emission with biomass and a decrease of soil emission with surface soil moisture, the point at maximum brightness temperature corresponds to full-cover vegetation with dry soil. It could correspond to full-cover green vegetation. However, the associated land surface temperature in Fig. 5(a) is much larger than that over full-cover green vegetation (21 °C) and rather close to the temperature over full-cover senescent vegetation (34 °C). Therefore, the point at maximum brightness temperature corresponds to full-cover senescent vegetation with dry soil. This vertex is noted as $\mathbf{D}'$ in Fig. 5(a), which is consistent with Fig. 4. A prime mark indicates that $\mathbf{D}'$ corresponds to a dry soil, whereas $\mathbf{D}$ does not specify soil hydric status. Note that $\mathbf{D}'$ does not necessarily correspond to dry senescent vegetation since wet senescent vegetation can lead to large values of brightness temperature [50]. In our case study, however, no rainfall occurred during the four days preceding the ASTER overpass, which means that senescent vegetation was completely dry. In terms of radiative transfer modeling, the effect of dry biomass on brightness temperature can be represented by large values of roughness parameter [51].
4) Vertices at minimum land surface temperature: two more vertices are apparent in the counterclockwise direction. Being consistent with a decrease of land surface temperature with green vegetation, both points correspond to full-cover green vegetation. As vegetation is partially transparent to the L-band emission from the soil, each point corresponds to a different soil hydric status. The vertex with a larger TB [noted as $\mathbf{C}''$ in Fig. 5(a)] corresponds to full-cover green vegetation with dry soil, and the point with a lower TB [noted as $\mathbf{C}'$ in Fig. 5(a)] corresponds to full-cover green vegetation with wet soil.

As high-resolution temperature is assumed to be unavailable in this paper, brightness temperature end-members are not estimated from the polygon $TB - T$ in Fig. 5(a) but from the polygon $TB - f_{\mathrm{gv}}$ shown in Fig. 5(b). The following is an interpretation of the polygon in Fig. 5(b), based on the consistency with the polygon in Fig. 5(a). In particular, the five vertices in Fig. 5(a) can be located in Fig. 5(b) as follows.

1) Vertex $\mathbf{B}$ corresponds to wet bare soil. It is located at the minimum value of brightness temperature such that $f_{\mathrm{gv}} = 0$.
2) Vertex $\mathbf{A}$ corresponds to bare dry soil. It is not apparent in Fig. 5(b) because fractional green vegetation is not sufficient information to distinguish between bare soil and senescent vegetation.
3) Vertex $\mathbf{D}'$ corresponds to full-cover senescent vegetation with dry soil. It is located at the maximum value of brightness temperature.
4) Vertex $\mathbf{C}''$ corresponds to full-cover green vegetation with dry soil. It is located at the maximum value of brightness temperature such that $f_{\mathrm{gv}} = 1$.
5) Vertex $\mathbf{C}'$ corresponds to full-cover green vegetation with wet soil. It is located at the minimum value of brightness temperature such that $f_{\mathrm{gv}} = 1$.

Based on the aforementioned interpretation of the polygon $TB - f_{\mathrm{gv}}$ in Fig. 5(b), the methodology used for estimating

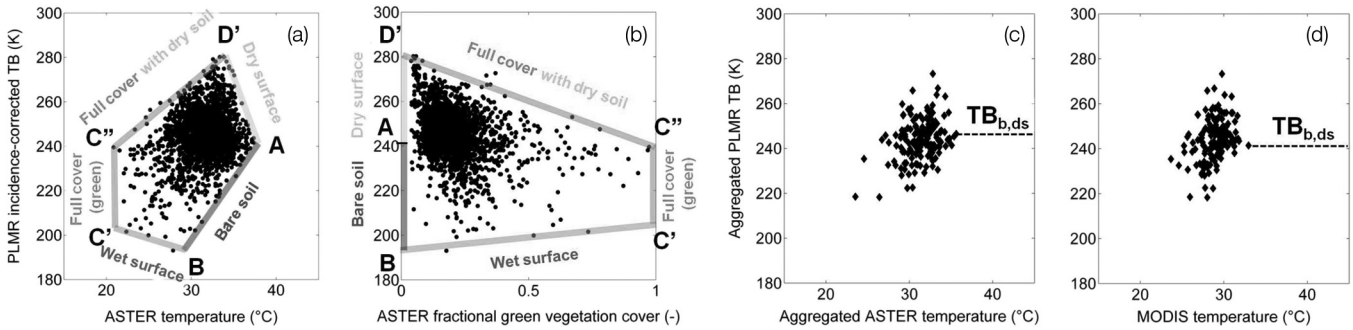

Fig. 5. (a) Scatterplot of PLMR incidence-corrected brightness temperature TB versus ASTER land surface temperature and (b) versus ASTER fractional green vegetation cover, and (c) scatterplot of aggregated TB versus aggregated ASTER temperature and (d) versus MODIS temperature. Extreme brightness temperatures $\mathbf{TB_{b,ws}}$, $\mathbf{TB_{fcgv,ws}}$, $\mathbf{TB_{fcgv,ds}}$, and $\mathbf{TB_{fcsv,ds}}$ are estimated by interpreting the bare soil, dry surface, full-cover vegetation, and wet surface edges of the polygon in (b). The estimation of $\mathbf{TB_{b,ds}}$ using low-resolution temperature data is illustrated with aggregated ASTER temperature in (c) and MODIS temperature in (d).

$\mathbf{TB_{b,ds}}$, $\mathbf{TB_{b,ws}}$, $\mathbf{TB_{fcgv,ws}}$, $\mathbf{TB_{fcgv,ds}}$, and $\mathbf{TB_{fcsv,ds}}$ is detailed in the following.

1) The brightness temperature over full-cover dry surface ($\mathbf{TB_{fcsv,ds}}$) and over wet bare soil ($\mathbf{TB_{b,ws}}$) are set to the maximum and minimum brightness temperatures observed within the study area, respectively.
2) The brightness temperatures over full-cover green vegetation with wet soil ($\mathbf{TB_{fcgv,ws}}$) and over full-cover green vegetation with dry soil ($\mathbf{TB_{fcgv,ds}}$) are estimated as the brightness temperature extrapolated at $f_{\rm gv} = 1$ in Fig. 5(b) along the "wet soil" and the "full-cover dry soil" edge, respectively. The slope of the lines ($\mathbf{BC}'$) and ($\mathbf{D}'\mathbf{C}''$) are determined so that all of the points with $f_{\rm gv} > 0.5$ be above and below the "wet soil" and "full-cover dry soil" edges, respectively.
3) Vertex $\mathbf{A}$ cannot be identified in the space $TB - f_{\rm gv}$. Consequently, $\mathbf{TB_{b,ds}}$ is set to the brightness temperature corresponding to the maximum $T_{\rm km}$ (see Fig. 5(c) for aggregated ASTER temperature and Fig. 5(d) for MODIS temperature data).

Table III lists the five brightness temperature end-members: 1) estimated from Fig. 5(a) using high-resolution ASTER data; 2) estimated from Fig. 5(b) and (c) using high-resolution fractional green vegetation cover and aggregated ASTER temperature data; and 3) estimated from Fig. 5(b) and (d) using high-resolution fractional green vegetation cover and MODIS temperature data. Values estimated from low-resolution temperature are remarkably close to those estimated from high-resolution ASTER temperature data (Table III), except for $\mathbf{TB_{b,ds}}$ with a difference of 6 K. This difference is apparently due to the lack of representativeness of kilometric aggregated brightness temperature and the method for estimating $\mathbf{TB_{b,ds}}$ at kilometric scale. Note, however, that a 6-K difference is still relatively low compared to the range (190 K–280 K) covered by brightness temperature values.

VI. Application

The disaggregation algorithms presented here are applied to the NAFE'06 data set. ASTER land surface temperature is aggregated at 1-km resolution, and kilometric temperature is used as input to D0, D1, D1′, D2, D2′, D3′, D4′, and D4″. As shown in Fig. 1, the verification strategy consists in comparing disaggregation results at 250-m resolution with ASTER land surface temperature. An application to MODIS data is also presented.

A. Application to Aggregated ASTER Data

1) End-Members Derived From High-Resolution Data: The approach is first implemented using the end-members estimated from high-resolution ASTER temperature data. This allows testing the robustness of the model in (15) and (16) independently of the methodology used for extrapolating the nine end-members $\mathbf{T_{b,ds}}$, $\mathbf{T_{b,ws}}$, $\mathbf{T_{fcgv}}$, $\mathbf{T_{fcsv}}$, $\mathbf{TB_{b,ds}}$, $\mathbf{TB_{b,ws}}$, $\mathbf{TB_{fcgv,ws}}$, $\mathbf{TB_{fcgv,ds}}$, and $\mathbf{TB_{fcsv,ds}}$.

Fig. 6 shows the output images of the eight disaggregation algorithms, which are to be compared with the reference image derived from ASTER land surface temperature. One observes that the disaggregated temperature is successively improved by including additional factors in the disaggregation, which indicates that the methodology is able to take into account several independent factors. Although the boxy artifact at 1-km resolution is successively reduced from $T^{(0)}$ to $T^{(4'')}$, it is still apparent for $T^{(4'')}$. This effect may be due to the following: 1) other factors that are not taken into account in the procedure, such as green vegetation water stress, wind speed, surface emissivity, surface albedo, etc.; 2) errors in estimated $f_{\rm gv}$, $f_{\rm sv}$, $f_{\rm ow}$, and β; and/or 3) resampling errors at 250-m resolution.

Table IV lists the RMSD, correlation coefficient, and slope between the disaggregated and ASTER temperatures for each of the eight disaggregation algorithms. The error is successively decreased from 1.65 °C to 1.16 °C, while the correlation coefficient and slope are successively increased from 0.79 and 0.63 to 0.89 and 0.88, respectively. When comparing D1, D2, D1′, and D2′, no significant differences are observed between all four algorithms in terms of root-mean-square error, correlation coefficient, and slope. Note that, in this paper, $f_{\rm tv}$ was estimated in a different way than in [5] because only one visible and near-infrared image was available and a FORMOSAT-like time series would be required to derive $f_{\rm tv}$ more accurately on a pixel-by-pixel basis. Nevertheless, this comparison suggests that D1′ seems to be equivalent to D1 and D2′ equivalent to D2, which justifies the use of the $T_{\rm mod}$ model.

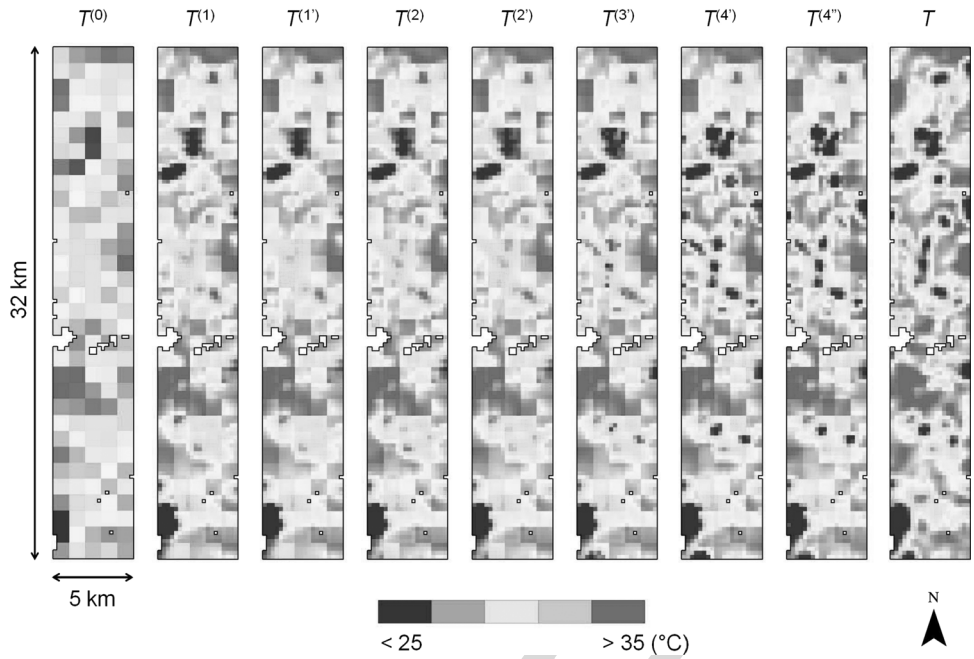

Fig. 6. Maps of the temperature disaggregated by the eight algorithms as compared with the map (right) of high-resolution ASTER temperature.

TABLE IV
RMSD, CORRELATION COEFFICIENT (R), AND SLOPE BETWEEN THE DISAGGREGATED AND ASTER TEMPERATURES. THE RESULTS CORRESPOND TO THE END-MEMBERS ESTIMATED USING HIGH-RESOLUTION ASTER TEMPERATURE DATA (TO THE END-MEMBERS EXTRAPOLATED USING AGGREGATED ASTER TEMPERATURE DATA)

Algorithm	RMSD °C	R -	Slope -
D0	1.65	0.79	0.63
D1	1.39	0.86	0.76
D2	1.35 (1.35)	0.87 (0.87)	0.76 (0.76)
D1′	1.38 (1.39)	0.86 (0.86)	0.74 (0.72)
D2′	1.30 (1.40)	0.88 (0.86)	0.75 (0.73)
D3′	1.22 (1.27)	0.89 (0.88)	0.78 (0.76)
D4′	1.15 (1.15)	0.91 (0.91)	0.86 (0.84)
D4″	1.16 (1.24)	0.89 (0.80)	0.88 (0.86)

The main advantage of the new approach is to take into account a number of additional factors, including fractional open water and soil evaporative efficiency. When comparing the results obtained for D3′, D4′, and D4″ in Table IV, it is observed that the disaggregated temperature is significantly improved against the classical approaches D1 and D2. Moreover, the statistical results are successively improved by including f_{ow}, β, and β'. Fig. 7 shows the improvement, especially in the slope between the disaggregated and ASTER temperatures. The good results obtained for D4″ indicate that the performance of disaggregation algorithms is intimately related to the following: 1) the capability of separating the independent factors that impact on surface temperature and 2) the ability to integrate them consistently into the procedure.

2) End-Members Derived From Aggregated ASTER Data: As disaggregation procedures D1′, D2′, D3′, D4′, and D4″ are subjected to uncertainties in land surface temperature and brightness temperature end-members, the five algorithms are next tested using the end-members estimated from kilometric temperature data, as presented in Section V. Aggregated ASTER (instead of MODIS) data are used to evaluate the

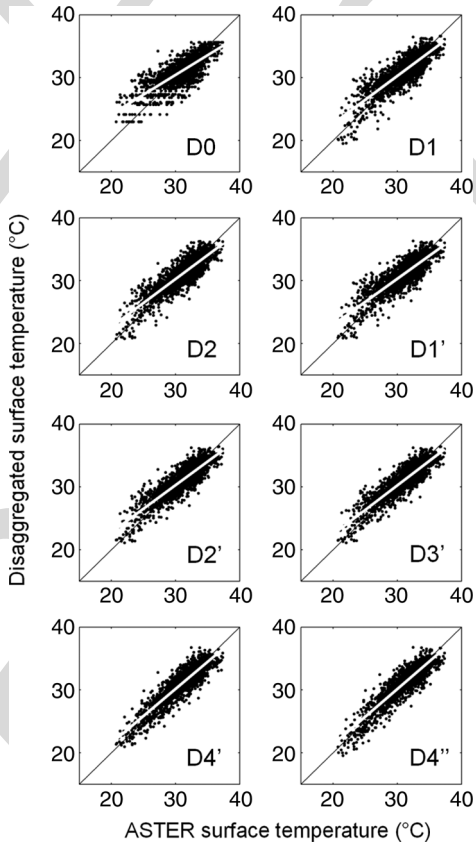

Fig. 7. Aggregated ASTER temperature (1 km) is disaggregated by each of the eight algorithms and is plotted against high-resolution ASTER temperature.

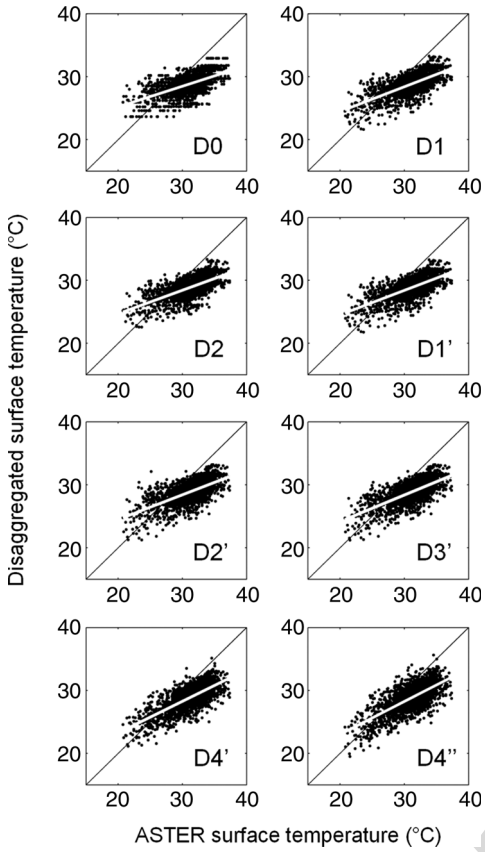

Fig. 8. MODIS temperature (1 km) is disaggregated by each of the eight algorithms and is plotted against high-resolution ASTER temperature.

impact of end-members regardless of the discrepancy between MODIS and ASTER temperatures.

Table IV lists the RMSD, correlation coefficient, and slope between the disaggregated and ASTER temperatures for each of the five algorithms. Results are compared with those obtained using the end-members estimated from high-resolution ASTER temperature. In general, the error is slightly larger, and the correlation coefficient and slope are slightly lower using extrapolated end-members. Nevertheless, the disaggregated temperature is still much improved by applying D4″ instead of D1′, with the correlation coefficient and slope increasing from 0.74 to 0.88 and from 0.72 to 0.86, respectively. Consequently, the extrapolation of end-members from kilometric data is not found to be a limiting factor in the methodology.

B. Application to MODIS Data

Disaggregation algorithms D0, D1, D1′, D2, D2′, D3′, D4′, and D4″ are then applied to MODIS data. In this case, end-members are derived from MODIS data. Fig. 8 shows the scatterplot of disaggregated MODIS versus ASTER temperature for each algorithm separately. One observes that the new methodology improves the correlation and slope of the linear regression between the disaggregated and ASTER temperatures. However, a systematic negative bias is apparent in the disaggregated temperature. Table V lists the RMSD, correlation coefficient, and slope between the disaggregated and ASTER temperatures for each of the eight algorithms. The error slightly decreases

TABLE V
RMSD, CORRELATION COEFFICIENT (R), AND SLOPE BETWEEN THE DISAGGREGATED AND ASTER TEMPERATURES. THE RESULTS CORRESPOND TO THE END-MEMBERS EXTRAPOLATED USING MODIS TEMPERATURE DATA

Algorithm	RMSD °C	R -	Slope -
D0	3.19	0.60	0.33
D1	3.08	0.67	0.39
D2	3.11	0.66	0.37
D1′	3.09	0.67	0.39
D2′	3.12	0.65	0.39
D3′	3.06	0.69	0.42
D4′	2.98	0.73	0.50
D4″	3.03	0.70	0.52

from 3.2 °C to 3.0 °C, while the correlation coefficient and slope increase from 0.6 and 0.3 to 0.7 and 0.5, respectively. The results obtained for D3′ and D4′ in Table V indicate that the disaggregated temperature is improved against the classical approaches D1 and D2. As for the application to aggregated ASTER data, the statistical results are successively improved by including f_{ow}, β, and β'. However, the improvement with MODIS data is not as visible as with aggregated ASTER data because the difference between MODIS and ASTER data (please refer to Section II-C) has the same order of magnitude as the subpixel variability at 250-m resolution (see RMSD for D0 in Table V). In particular, the mean bias and the relatively low slope of the linear regression between the disaggregated and ASTER data are associated with the discrepancy at 1-km resolution between the MODIS and ASTER temperature data.

VII. SENSITIVITY ANALYSIS

To further assess the stability of the new D′ algorithms based on radiative transfer, two sensitivity analyses are conducted by the following: 1) adding a Gaussian noise on kilometric temperatures and high-resolution brightness temperatures and 2) estimating the contribution of each factor on the variability of modeled land surface temperature.

A. Uncertainty in End-Members

To test the stability of the method for estimating the nine end-members ($\mathbf{T_{b,ds}}$, $\mathbf{T_{b,ws}}$, $\mathbf{T_{fcgv}}$, $\mathbf{T_{fcsv}}$, $\mathbf{TB_{b,ds}}$, $\mathbf{TB_{b,ws}}$, $\mathbf{TB_{fcgv,ws}}$, $\mathbf{TB_{fcgv,ds}}$, and $\mathbf{TB_{fcsv,ds}}$) from low-resolution temperature data, a Gaussian noise with a standard deviation of 1 °C is added to the kilometric (aggregated ASTER) land surface temperature data set, and a Gaussian noise with a standard deviation of 2 K is added to the high-resolution brightness temperature data set. An ensemble of 100 data sets is generated and used as input to the disaggregation algorithms.

Table VI reports the average and standard deviation of extrapolated end-members computed within the ensemble of 100 artificially perturbed data sets. Results indicate that the method for extrapolating end-members is stable for all end-members.

TABLE VI
MEAN AND STANDARD DEVIATION OF LAND SURFACE TEMPERATURE AND L-BAND BRIGHTNESS TEMPERATURE END-MEMBERS EXTRAPOLATED USING KILOMETRIC TEMPERATURE DATA. FOR THE CONVENIENCE OF THE READER, THE UNIT IS DEGREE CELSIUS FOR RADIOMETRIC TEMPERATURE AND KELVIN FOR BRIGHTNESS TEMPERATURE

End-member	Mean	St. dev.	Unit
$\mathbf{T_{b,ds}}$	40.8	0.8	°C
$\mathbf{T_{b,ws}}$	25.7	1.5	°C
$\mathbf{T_{fcgv}}$	21.0	0	°C
$\mathbf{T_{fcsv}}$	33.1	1.3	°C
$\mathbf{TB_{b,ds}}$	246	3.2	K
$\mathbf{TB_{b,ws}}$	193	1.4	K
$\mathbf{TB_{fcgv,ws}}$	204	2.3	K
$\mathbf{TB_{fcgv,ds}}$	240	1.5	K
$\mathbf{TB_{fcsv,ds}}$	281	1.0	K

TABLE VII
RMSD, CORRELATION COEFFICIENT (R), AND SLOPE BETWEEN THE DISAGGREGATED AND ASTER TEMPERATURES FOR THE DATA INCLUDING ALL THE 100 ARTIFICIALLY NOISED DATA SETS

Algorithm	RMSD °C	R -	Slope -
D0	1.81	0.75	0.63
D1	1.58	0.82	0.76
D2	1.54	0.83	0.76
D1′	1.57	0.82	0.73
D2′	1.54	0.83	0.74
D3′	1.44	0.85	0.78
D4′	1.39	0.87	0.87
D4″	1.48	0.86	0.89

Table VII lists the RMSD, correlation coefficient, and slope between the disaggregated and ASTER temperatures for all 100 data sets. Although the results are generally degraded by using noisy input data sets, D4″ is still superior to all other algorithms (see Fig. 9). Therefore, the integration of fractional open water and soil evaporative efficiency into the disaggregation is able to improve the representation of land surface temperature variability despite the uncertainties in $f_{\rm ow}$ and β', and the uncertainties in extrapolated end-members.

B. Weighting Variability Factors

Results with the NAFE'06 data set have indicated that the new D′ algorithms based on radiative transfer significantly improve (in relation to D1 and D2 methods) the representation of disaggregated temperature by directly integrating the various input parameters of the radiative transfer equation. Another advantage of the proposed methodology is to quantify the weight of these input parameters. Here, the relative weights of $f_{\rm gv}$, $f_{\rm sv}$, $f_{\rm ow}$, and β' are compared, and the relative improvement in disaggregated temperature when including these factors in the disaggregation is assessed. The weight of $f_{\rm gv}$ on the variability

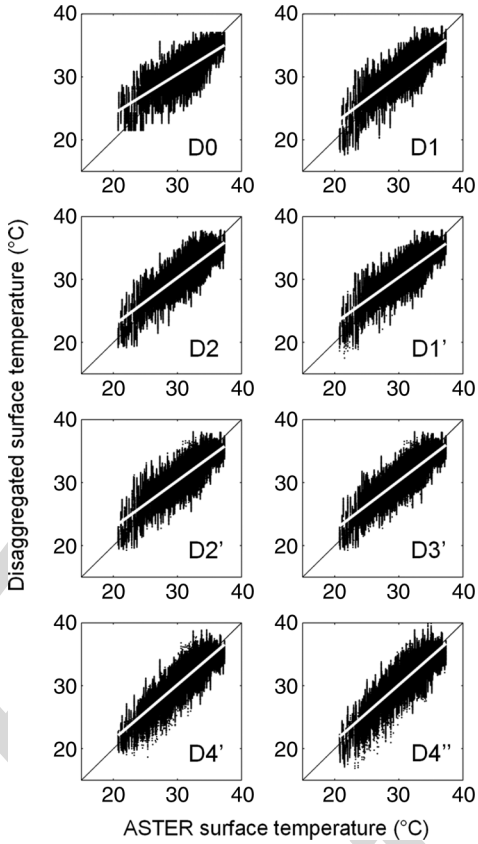

Fig. 9. As for Fig. 7 but using all the 100 artificially noised input data sets.

in land surface temperature is derived by computing the first partial derivative of $T_{\rm mod}$ from (15) and (16)

$$\frac{\partial T_{\rm mod}}{\partial f_{\rm gv}} = -(1-f_{\rm ow})(\mathbf{T_{fcsv}} - \mathbf{T_{fcgv}}). \quad (25)$$

Similarly, the first partial derivative of $T_{\rm mod}$ is computed with respect to $f_{\rm sv}$

$$\frac{\partial T_{\rm mod}}{\partial f_{\rm sv}} = -(1-f_{\rm ow})\left[\beta'\mathbf{T_{b,ws}} + (1-\beta')\mathbf{T_{b,ds}} - \mathbf{T_{fcsv}}\right] \quad (26)$$

with respect to $f_{\rm ow}$

$$\frac{\partial T_{\rm mod}}{\partial f_{\rm ow}} = -\left[f_{\rm gv}\mathbf{T_{fcgv}} + (f_{\rm tv}-f_{\rm gv})\mathbf{T_{fcsv}} + (1-f_{\rm tv})\left(\beta'\mathbf{T_{b,ws}} + (1-\beta')\mathbf{T_{b,ds}}\right) - \mathbf{T_{fcgv}}\right] \quad (27)$$

and with respect to β'

$$\frac{\partial T_{\rm mod}}{\partial \beta'} = -(1-f_{\rm ow})(1-f_{\rm tv})(\mathbf{T_{b,ds}} - \mathbf{T_{b,ws}}). \quad (28)$$

Table VIII lists the standard deviation of each parameter within the study area, the average of partial derivatives, and the relative weight of each parameter on the variability of modeled land surface temperature. The relative weights of $f_{\rm gv}$, $f_{\rm sv}$, $f_{\rm ow}$, and β' are estimated as the mean partial derivative times the standard deviation. Results indicate that all parameters have a negative impact on T. More interestingly, $f_{\rm gv}$ appears to be the most significant variability factor, with a relative weight of 42%, which is consistent with NDVI-based approaches [4].

TABLE VIII
STANDARD DEVIATION, MEAN PARTIAL DERIVATIVE, AND IMPACT ON HIGH-RESOLUTION MODELED TEMPERATURE OF EACH OF THE FOUR PARAMETERS: FRACTIONAL GREEN VEGETATION COVER, FRACTIONAL SENESCENT VEGETATION COVER, FRACTIONAL OPEN WATER, AND SOIL EVAPORATIVE EFFICIENCY

Factor	Standard deviation	Mean partial derivative	Impact on T_{mod} (percentage of total)
-	-	°C	°C (%)
f_{gv}	0.11	−13	0.97 (42)
f_{sv}	0.19	−2.0	0.26 (11)
f_{ow}	0.06	−11	0.45 (20)
β'	0.19	−4.8	0.17 (27)

The second and third most significant variability factors are soil evaporative efficiency and fractional open water, with relative weights of 27% and 20%, respectively. Finally, fractional senescent vegetation cover represents only 11% of the variability in land surface temperature. The low impact of f_{sv} can be associated with the low mean partial derivative. In particular, $\partial T_{\mathrm{mod}}/\partial f_{\mathrm{sv}}$ is low because the temperature difference between dry bare soil ($\mathbf{T_{b,ds}}$) and full-cover senescent vegetation ($\mathbf{T_{fcsv}}$) is also low in our case study.

The relative weights in Table VIII are now related with the disaggregation results in Table III. Consequently, the poor improvement of D2 against D1 (and D2′ against D1′) can be attributed to the relatively low weight of f_{sv} in the variability of land surface temperature. Conversely, the significant improvements of D4″ against D3′, D3′ against D2′, and D1 (and D1′) against D0 are attributed to the large weights of β', f_{ow}, and f_{gv}, respectively.

In summary, the variability of land surface temperature is reasonably represented by model T_{mod}. Moreover, the approach allows the relative weight of each variability factor to be taken into account in the disaggregation procedure.

VIII. SUMMARY AND CONCLUSION

A new disaggregation methodology for land surface temperature has been developed to integrate the main surface parameters involved in the surface energy budget. It is based on a linearized radiative transfer equation, which distinguishes between soil, vegetation, and water temperature, and uses soil evaporative efficiency and fractional senescent vegetation cover to parameterize/estimate soil and vegetation hydric status, respectively. The approach is implemented using four parameters: the fraction of green vegetation cover derived from red and near-infrared bands, the fraction of senescent vegetation cover derived from red and near-infrared bands, the fraction of open water derived from shortwave-infrared band, and the soil evaporative efficiency derived from microwave-L band. It is tested over a 5 km by 32 km area of irrigated land in Australia, including flooded rice crops, using ASTER and L-band airborne data. Low-resolution land surface temperature is simulated by aggregating ASTER land surface temperature at 1-km resolution, and the disaggregated temperature is compared to high-resolution ASTER temperature. The results indicate that the methodology is able to separate efficiently the independent factors that impact surface temperature and to integrate them consistently into the disaggregation procedure. The error in disaggregated temperature is successively reduced from 1.65 °C to 1.16 °C by including each of the four parameters. The correlation coefficient and slope between the disaggregated and ASTER temperatures are improved from 0.79 to 0.89 and from 0.63 to 0.88, respectively. Moreover, the radiative transfer equation allows quantifying the impact at high resolution of each parameter on land surface temperature. In this case study, fractional green vegetation cover is responsible for 42% of the variability in disaggregated land surface temperature, fractional senescent vegetation cover for 11%, fractional open water for 20%, and soil evaporative efficiency for 27%.

Note that the approach presented in this paper did not take into account the water stress of green vegetation because none of the considered parameters (fractional green vegetation cover, fractional senescent vegetation cover, fractional open water, and soil evaporative efficiency) could describe the hydric status of photosynthetically active (green) vegetation. The analysis was conducted solely in a highly irrigated environment in which vegetation water stress was small. However, in most cases, the vegetation water stress might not be negligible for natural areas. In the presence of water-stressed green vegetation, the scatterplot (temperature versus green vegetation cover) would be transformed into a trapezoidal shape with four vertices rather than a triangle. In such conditions, the disaggregation problem would be partly undetermined since the partitioning between unstressed and stressed green vegetations would not be represented. Consequently, the approaches shown here are not expected to be representative of other less extreme environments than the present irrigated area. Nevertheless, one should keep in mind that improving the spatial resolution of land surface temperature data via disaggregation is only relevant in the conditions where the spatial variability of temperature is large.

Although the approach was successfully applied to airborne and satellite data collected during NAFE'06, further research is needed to test the disaggregation approach on a routine basis. One may anticipate that fractional green and senescent vegetation covers could be derived accurately using FORMOSAT-like data. The FORMOSAT-2 instrument [52] provides shortwave data at high spatial resolution (8 m) and high temporal frequency (potentially one image per day), which allow a fine analysis of the seasonality of canopies during the crop cycle [5], [53], [54]. Fractional open water could be derived from Landsat-5 data (e.g., [20]). Although the repeat cycle of Landsat (16 days) is longer than the temporal resolution needed for land surface temperature, the seasonal variations of water bodies

such as irrigation canals and flooded fields are expected to be low. Soil evaporative efficiency could be derived at high resolution from active microwave sensors, such as the Phased Array L-band SAR (PALSAR) [55]. Soil evaporative efficiency formulas express evaporation as a function of normalized surface soil moisture. Therefore, soil evaporative efficiency is equivalent to a soil moisture index, which could be replaced in (20) by the radar-derived soil wetness index computed as the observed to minimal backscattering coefficient difference divided by the maximal to minimal backscattering coefficient difference [56], [57]. Note, however, that the temporal coverage of the PALSAR fine beam dual polarization mode is relatively low, with a revisit cycle of 46 days. Consequently, accurate disaggregation of land surface temperature would still rely on the availability of high-resolution radar data.

ACKNOWLEDGMENT

The authors would like to thank the NAFE'06 participants for their participation in collecting this extensive data set.

REFERENCES

[1] S. Stisen, I. Sandholt, A. Nørgaard, R. Fensholt, and K. H. Jensen, "Combining the triangle method with thermal inertia to estimate regional evapotranspiration—Applied to MSG-SEVERI data in the Senegal River basin," *Remote Sens. Environ.*, vol. 112, no. 3, pp. 1242–1255, Mar. 2008.

[2] R. Tang, Z.-L. Li, and B. Tang, "An application of the Ts-VI method with enhanced edges determination for evapotranspiration estimation from MODIS data in arid and semi-arid regions: Implementation and validation," *Remote Sens. Environ.*, vol. 114, no. 3, pp. 540–551, Mar. 2010. doi:DOI:10.1016/j.rse.2009.10.012.

[3] B. Seguin, F. Becker, T. Phulpin, X. F. Gu, G. Guyot, Y. Kerr, C. King, J. P. Lagouarde, C. Ottlé, M. P. Stoll, A. Tabbagh, and A. Vidal, "IRSUTE: A minisatellite project for land surface heat flux estimation from field to regional scale," *Remote Sens. Environ.*, vol. 68, no. 3, pp. 357–369, Jun. 1999.

[4] N. Agam, W. P. Kustas, M. C. Anderson, F. Li, and C. M. U. Neale, "A vegetation index based technique for spatial sharpening of thermal imagery," *Remote Sens. Environ.*, vol. 107, no. 4, pp. 545–558, Apr. 2007.

[5] O. Merlin, B. Duchemin, O. Hagolle, F. Jacob, B. Coudert, G. Chehbouni, G. Dedieu, J. Garatuza, and Y. Kerr, "Disaggregation of MODIS surface temperature over an agricultural area using a time series of FORMOSAT-2 images," *Remote Sens. Environ.*, vol. 114, no. 11, pp. 2500–2512, Nov. 2010. doi:DOI:10.1016/j.rse.2010.05.025.

[6] S. B. Idso, R. D. Jackson, P. J. Pinter, R. J. Reginato, and J. L. Hatfield, "Normalizing the stress–degree–day parameter for environmental variability," *Agric. Meteorol.*, vol. 24, no. 1, pp. 45–55, 1981.

[7] R. D. Jackson, S. B. Idso, R. J. Reginato, and P. J. Pinter, "Canopy temperature as a crop water stress indicator," *Water Resour. Res.*, vol. 17, no. 4, pp. 1133–1138, 1981.

[8] M. S. Moran, T. R. Clarke, Y. Inoue, and A. Vidal, "Estimating crop water deficit using the relation between surface-air temperature and spectral vegetation index," *Remote Sens. Environ.*, vol. 49, no. 3, pp. 246–263, Sep. 1994.

[9] O. Merlin, J. P. Walker, J. D. Kalma, E. J. Kim, J. Hacker, R. Panciera, R. Young, G. Summerell, J. Hornbuckle, M. Hafeez, and T. J. Jackson, "The NAFE'06 data set: Towards soil moisture retrieval at intermediate resolution," *Adv. Water Resour.*, vol. 31, no. 11, pp. 1444–1455, Nov. 2008. doi:DOI:10.1016/j.advwatres.2008.01.018.

[10] R. Panciera, J. P. Walker, J. D. Kalma, E. J. Kim, J. Hacker, O. Merlin, M. Berger, and N. Skou, "The NAFE'05/CoSMOS data set: Toward SMOS calibration, downscaling and assimilation," *IEEE Trans. Geosci. Remote Sens.*, vol. 46, no. 3, pp. 736–745, Mar. 2008. doi:DOI:10.1109/TGRS.2007.915403.

[11] T. Schmugge, T. J. Jackson, W. P. Kustas, R. Roberts, R. Parry, D. C. Goodrich, S. A. Amer, and M. A. Weltz, "Push broom microwave radiometer observations of surface soil moisture in Monsoon '90," *Water Resour. Res.*, vol. 30, no. 5, pp. 1321–1328, 1994.

[12] M. Abrams, "The Advanced Spaceborne Thermal Emission and Reflection radiometer (ASTER): Data products for the high spatial resolution imager on NASA's Terra platform," *Int. J. Remote Sens.*, vol. 21, pp. 847–859, 2000.

[13] K. Thome, K. Arai, S. Hook, H. Kieer, H. Lang, T. Matsunaga, A. Ono, F. Palluconi, H. Sakuma, P. Slater, T. Takashima, H. Tonooka, S. Tsuchida, R. M. Welch, and E. Zalewski, "ASTER preflight and inflight calibration and the validation of level 2 products," *IEEE Trans. Geosci. Remote Sens.*, vol. 36, no. 4, pp. 1161–1172, Jul. 1998.

[14] F. Jacob, F. Petitcolin, T. Schmugge, E. Vermote, A. French, and K. Ogawa, "Comparison of land surface emissivity and radiometric temperature derived from MODIS and ASTER sensors," *Remote Sens. Environ.*, vol. 90, no. 2, pp. 137–152, Mar. 2004.

[15] J. A. Sobrino, J. C. Jiménez-Muñoz, L. Balick, A. R. Gillespie, D. A. Sabol, and W. T. Gustafson, "Accuracy of ASTER level-2 thermal-infrared standard products of an agricultural area in Spain," *Remote Sens. Environ.*, vol. 106, no. 2, pp. 146–153, Jan. 2007. doi:DOI:10.1016/j.rse.2006.08.010.

[16] C. Coll, V. Caselles, E. Valor, R. Niclòs, J. M. Sánchez, J. M. Galve, and M. Mira, "Temperature and emissivity separation from ASTER data for low spectral contrast surfaces," *Remote Sens. Environ.*, vol. 110, no. 2, pp. 162–175, Sep. 2007. doi:DOI:10.1016/j.rse.2007.02.008.

[17] A. French, T. Schmugge, J. Ritchie, A. Hsu, F. Jacob, and K. Ogawa, "Detecting land cover change at the Jornada Experimental Range, New Mexico with ASTER emissivities," *Remote Sens. Environ.*, vol. 112, no. 4, pp. 1730–1748, Apr. 2008. doi:DOI:10.1016/j.rse.2007.08.020.

[18] F. Jacob, T. Schmugge, A. Olioso, D. Courault, A. French, K. Ogawa, F. Petitcolin, G. Chehbouni, A. Pinheiro, and J. Privette, *Modeling and Inversion in Thermal Infrared Remote Sensing Over Vegetated Land Surfaces. Advances in Land Remote Sensing*, vol. 10, S. Liang, Ed. New York: Springer-Verlag, 2008.

[19] D. E. Sabol, A. R. Gillespie, E. Abbott, and G. Yamada, "Field validation of the ASTER temperature–emissivity separation algorithm," *Remote Sens. Environ.*, vol. 113, no. 11, pp. 2328–2344, Nov. 2009. doi:DOI:10.1016/j.rse.2009.06.008.

[20] T. G. Van Niel, T. R. McVicar, H. Fang, and S. Liang, "Calculating environmental moisture for per-field discrimination of rice crops," *Int. J. Remote Sens.*, vol. 24, no. 4, pp. 885–890, 2003.

[21] Y. Liu, T. Hiyama, and Y. Yamaguchi, "Scaling of land surface temperature using satellite data: A case examination on ASTER and MODIS products over a heterogeneous terrain area," *Remote Sens. Environ.*, vol. 105, no. 2, pp. 115–128, Nov. 2006.

[22] Z. Wan and J. Dozier, "A generalized split-window algorithm for retrieving land-surface temperature from space," *IEEE Trans. Geosci. Remote Sens.*, vol. 34, no. 4, pp. 892–905, Jul. 1996.

[23] G. C. Hulley and S. J. Hook, "Generating consistent land surface temperature and emissivity products between ASTER and MODIS data for Earth science research," *IEEE Trans. Geosci. Remote Sens.*, vol. 49, no. 9, pp. 1304–1315, Apr. 2011. doi:DOI:10.1109/TGRS.2010.2063034.

[24] M. Atitar and J. A. Sobrino, "A split-window algorithm for estimating LST from Meteosat 9 data: Test and comparison with *in situ* data and MODIS LSTs," *IEEE Geosci. Remote Sens. Lett.*, vol. 6, no. 1, pp. 122–126, Jan. 2009. doi:DOI:10.1109/LGRS.2008.2006410.

[25] Y. Liu, Y. Yamaguchi, and C. Ke, "Reducing the discrepancy between ASTER and MODIS land surface temperature products," *Sensors*, vol. 7, pp. 3043–3057, 2007.

[26] O. Merlin, G. Chehbouni, Y. Kerr, E. G. Njoku, and D. Entekhabi, "A combined modeling and multi-spectral/multi-resolution remote sensing approach for disaggregation of surface soil moisture: Application to SMOS configuration," *IEEE Trans. Geosci. Remote Sens.*, vol. 43, no. 9, pp. 2036–2050, Sep. 2005.

[27] T. Carlson, "An overview of the 'triangle method' for estimating surface evapotranspiration and soil moisture from satellite imagery," *Sensors*, vol. 7, pp. 1612–1629, 2007.

[28] M. C. Anderson, J. M. Norman, G. R. Diak, W. P. Kustas, and J. R. Mecikalski, "A two-source time-integrated model for estimating surface fluxes using thermal infrared remote sensing," *Remote Sens. Environ.*, vol. 60, no. 2, pp. 195–216, May 1997.

[29] O. Merlin and G. Chehbouni, "Different approaches in estimating heat flux using dual angle observations of radiative surface temperature," *Int. J. Remote Sens.*, vol. 25, no. 1, pp. 275–289, 2004.

[30] K. Nishida, R. R. Nemani, J. M. Glassy, and S. W. Running, "Development of an evapotranspiration index from Aqua/MODIS for monitoring surface moisture status," *IEEE Trans. Geosci. Remote Sens.*, vol. 41, no. 2, pp. 493–501, Feb. 2003.

[31] G. Gutman and A. Ignatov, "The derivation of the green vegetation fraction from NOAA/AVHRR data for use in numerical weather

prediction models," *Int. J. Remote Sens.*, vol. 19, no. 8, pp. 1533–1543, 1998.
[32] J. Noilhan and S. Planton, "A simple parameterization of land surface processes for meteorological models," *Monthly Weather Rev.*, vol. 117, no. 3, pp. 536–549, 1989.
[33] D. A. Roberts, M. O. Smith, and J. B. Adams, "Green vegetation, nonphotosynthetic vegetation, and soils in AVIRIS data," *Remote Sens. Environ.*, vol. 44, no. 2/3, pp. 255–269, May 1993.
[34] M. Weiss, F. Baret, M. Leroy, A. Begué, O. Hautecoeur, and R. Santer, "Hemispherical reflectance and albedo estimates from the accumulation of across track sun synchronous satellite data," *J. Geophys. Res.*, vol. 104, no. D18, pp. 221–232, 1999.
[35] F. Jacob, A. Olioso, M. Weiss, F. Baret, and O. Hautecoeur, "Mapping short-wave albedo of agricultural surfaces using airborne PolDER data," *Remote Sens. Environ.*, vol. 80, no. 1, pp. 36–46, Apr. 2002.
[36] F. Jacob, M. Weiss, A. Olioso, and A. French, "Assessing the narrowband to broadband conversion to estimate visible, near infrared and shortwave apparent albedo from airborne PolDER data," *Agronomie*, vol. 22, no. 6, pp. 537–546, Sep./Oct. 2002.
[37] F. Jacob and A. Olioso, "Derivation of diurnal courses of albedo and reflected solar irradiance from airborne PolDER data acquired near solar noon," *J. Geophys. Res.*, vol. 110, no. D10, p. D10 104, May 2005.
[38] A. Bsaibes, D. Courault, F. Baret, M. Weiss, A. Olioso, F. Jacob, O. Hagolle, O. Marloie, N. Bertrand, V. Desfond, and F. Kzemipour, "Albedo and LAI estimates from FORMOSAT-2 data for crop monitoring," *Remote Sens. Environ.*, vol. 113, no. 4, pp. 716–729, Apr. 2009. doi:DOI:10.1016/j.rse.2008.11.014.
[39] P. M. Barbosa, M. A. Casterad, and J. Herrero, "Performance of several Landsat 5 Thematic Mapper (TM) image classification methods for crop extent estimates in an irrigation district," *Int. J. Remote Sens.*, vol. 17, no. 18, pp. 3665–3674, Dec. 1996.
[40] H. Xu, "Modification of normalized difference water index (NDWI) to enhance open water features in remotely sensed imagery," *Int. J. Remote Sens.*, vol. 27, no. 14, pp. 3025–3033, Jul. 2006.
[41] W. P. Kustas, T. J. Schmugge, K. S. Humes, T. J. Jackson, R. Parry, M. A. Weltz, and M. S. Moran, "Relationships between evaporative fraction and remotely sensed vegetation index and microwave brightness temperature for semiarid rangelands," *J. Appl. Meteor.*, vol. 32, no. 12, pp. 1781–1790, Dec. 1993.
[42] J. W. Deardorff, "Efficient prediction of ground temperature and moisture with inclusion of a layer of vegetation," *J. Geophys. Res.*, vol. 83, no. C4, pp. 1889–1903, Apr. 1978.
[43] P. J. Camillo and R. J. Gurney, "A resistance parameter for bare soil evaporation models," *Soil Sci.*, vol. 141, no. 2, pp. 95–105, Feb. 1986.
[44] F. T. Ulaby, R. K. Moore, and A. K. Fung, *Microwave Remote Sensing: Active and Passive*, vol. 2. Norwood, MA: Artech House, 1982.
[45] T. J. Schmugge, "Applications of passive microwave observations of surface soil moisture," *J. Hydrol.*, vol. 212/213, pp. 188–197, Dec. 1998.
[46] M. C. Anderson, J. M. Norman, W. P. Kustas, R. Houborg, P. J. Starks, and N. Agam, "A thermal-based remote sensing technique for routine mapping of land-surface carbon, water and energy fluxes from field to regional scales," *Remote Sens. Environ.*, vol. 112, no. 12, pp. 4227–4241, Dec. 2008. doi:DOI:10.1016/j.rse.2008.07.009.
[47] L. M. Montandon and E. E. Small, "The impact of soil reflectance on the quantification of the green vegetation fraction from NDVI," *Remote Sens. Environ.*, vol. 112, no. 4, pp. 1835–1845, Apr. 2008. doi:DOI:10.1016/j.rse.2007.09.007.
[48] E. G. Njoku and D. Entekhabi, "Passive microwave remote sensing of soil moisture," *J. Hydrol.*, vol. 184, no. 1/2, pp. 101–129, Oct. 1996.
[49] J.-P. Wigneron, Y. Kerr, P. Waldteufel, K. Saleh, M.-J. Escorihuela, P. Richaume, P. Ferrazzoli, P. de Rosnay, R. Gurneye, J.-C. Calvet, J. P. Grant, M. Guglielmettih, B. Hornbuckle, C. Matzler, T. Pellarin, and M. Schwank, "L-band Microwave Emission of the Biosphere (L-MEB) model: Description and calibration against experimental data sets over crop fields," *Remote Sens. Environ.*, vol. 107, no. 4, pp. 639–655, Apr. 2007. doi:DOI:10.1016/j.rse.2008.10.014.
[50] K. Saleh, J.-P. Wigneron, P. de Rosnay, J.-C. Calvet, M. J. Escorihuela, Y. Kerr, and P. Waldteufel, "Impact of rain interception by vegetation and mulch on the L-band emission of natural grass," *Remote Sens. Environ.*, vol. 101, no. 1, pp. 127–139, Mar. 2006.
[51] K. Saleh, J.-P. Wigneron, P. Waldteufel, P. deRosnay, M. Schwank, J.-C. Calvet, and Y. H. Kerr, "Estimates of surface soil moisture under grass covers using L-band radiometry," *Remote Sens. Environ.*, vol. 109, no. 1, pp. 42–53, Jul. 2007.
[52] J.-S. Chern, J. Ling, and S.-L. Weng, "Taiwan's second remote sensing satellite," *Acta Astronaut.*, vol. 63, no. 11/12, pp. 1305–1311, Dec. 2008. doi:DOI:10.1016/j.actaastro.2008.05.022.
[53] B. Duchemin, O. Hagolle, B. Mougenot, I. Benhadj, R. Hadria, V. Simonneaux, J. Ezzahar, J. Hoedjes, S. Khabba, M. H. Kharrou, G. Boulet, G. Dedieu, S. Er-Raki, R. Escadafal, A. Olioso, and A. G. Chehbouni, "Agrometeorological study of semi-arid areas: An experiment for analysing the potential of time series of FORMOSAT-2 images (Tensift-Marrakech plain)," *Int. J. Remote Sens.*, vol. 29, no. 17, pp. 5291–5299, 2008. doi:DOI:10.1080/01431160802036482.
[54] R. Hadria, B. Duchemin, L. Jarlan, G. Dedieu, F. Baup, S. Khabba, A. Olioso, and T. Le Toan, "Potentiality of optical and radar satellite data at high spatio-temporal resolutions for the monitoring of irrigated wheat crops in Morocco," *Int. J. Appl. Earth Obs. Geoinf.*, vol. 12, pp. S32–S37, Feb. 2010. doi:DOI:10.1016/j.jag.2009.09.003.
[55] A. Rosenqvist, M. Shimada, N. Ito, and M. Watanabe, "ALOS PALSAR: A pathfinder mission for global-scale monitoring of the environment," *IEEE Trans. Geosci. Remote Sens.*, vol. 45, no. 11, pp. 3307–3316, Nov. 2007.
[56] W. Wagner, G. Lemoine, M. Borgeaud, and H. Rott, "A study of vegetation cover effects on ERS scatterometer data," *IEEE Trans. Geosci. Remote Sens.*, vol. 37, no. 2, pp. 938–948, Mar. 1999.
[57] R. Fieuzal, B. Duchemin, L. Jarlan, M. Zribi, F. Baup, O. Merlin, O. Hagolle, and J. Garatuza-Payan, "Combined use of optical and radar satellite data for the monitoring of irrigation and soil moisture of wheat crops," *Hydrol. Earth Syst. Sci.*, vol. 15, no. 4, pp. 1117–1129, 2011. doi:DOI:10.5194/hess-15-117-2011.

Olivier Merlin, photograph and biography not available at the time of publication. **AQ4**

Frédéric Jacob, photograph and biography not available at the time of publication.

Jean-Pierre Wigneron, photograph and biography not available at the time of publication.

Jeffrey Walker, photograph and biography not available at the time of publication.

Ghani Chehbouni, photograph and biography not available at the time of publication.

AUTHOR QUERIES

AUTHOR PLEASE ANSWER ALL QUERIES

Please be aware that the authors are required to pay overlength page charges ($200 per page) if the paper is longer than 6 pages. If you cannot pay any or all of these charges please let us know.

AQ1 = Please provide the current affiliation (name and specific address of the company) of authors "Frederic Jacob," "Jean-Pierre Wigneron," "Jeffrey Walker," and "Ghani Chehbouni."
AQ2 = The sentence that starts with "It is a three-step procedure..." was modified to properly introduce the list. Please check if the thought is preserved, and correct if necessary.
AQ3 = The caption for Table III was modified. Please check if the thought is preserved, and correct if necessary.
AQ4 = Please provide photo and biography of all authors.

END OF ALL QUERIES